Subtropical Stratocumulus and its Effect on Climate

Peter M. Caldwell

A dissertation submitted in partial fulfillment
of the requirements for the degree of

Doctor of Philosophy

University of Washington

2007

Program Authorized to Offer Degree: Department of Atmospheric Sciences

University of Washington
Graduate School

This is to certify that I have examined this copy of a doctoral dissertation by

Peter M. Caldwell

and have found that it is complete and satisfactory in all respects,
and that any and all revisions required by the final
examining committee have been made.
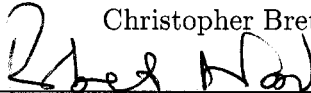

Chair of the Supervisory Committee:

_____

Christopher S. Bretherton
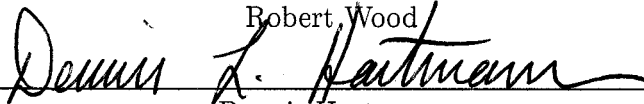
Reading Committee:

_____

Christopher Bretherton

_____

Robert Wood

_____

Dennis Hartmann

Date: 7/24/07

In presenting this dissertation in partial fulfillment of the requirements for the doctoral degree at the University of Washington, I agree that the Library shall make its copies freely available for inspection. I further agree that extensive copying of this dissertation is allowable only for scholarly purposes, consistent with "fair use" as prescribed in the U.S. Copyright Law. Requests for copying or reproduction of this dissertation may be referred to Proquest Information and Learning, 300 North Zeeb Road, Ann Arbor, MI 48106-1346, 1-800-521-0600, to whom the author has granted "the right to reproduce and sell (a) copies of the manuscript in microform and/or (b) printed copies of the manuscript made from microform."

Signature

Date 7/26/07

University of Washington

Abstract

Subtropical Stratocumulus and its Effect on Climate

Peter M. Caldwell

Chair of the Supervisory Committee:
Professor Christopher S. Bretherton
Department of Atmospheric Sciences

Despite widespread recognition of the importance of subtropical stratocumulus clouds to the planetary energy budget, the strength and even the sign of stratocumulus response to increased levels of greenhouse gases is still unknown. In this study, we attempt to address some of the causes for this uncertainty.

One challenge to assessing stratocumulus response to warming is that stratocumulus behavior is determined both by small-scale local processes and by the large-scale circulation. We present a new method which sidesteps this range-of-scales difficulty by explicitly resolving fine-scale detail in the stratocumulus region while implicitly including the effects of the large-scale circulation. The results of this model suggest that stratocumulus feedback acts to cool the planet.

Another reason why stratocumulus response to climate change is uncertain is that processes in the stratocumulus-topped boundary layer are not well understood or parameterized due to a dearth in measurements of key quantities. We improve this situation by deriving estimates of the diurnal cycle of entrainment from shipboard measurements taken during the East Pacific Investigation of Climate (EPIC) 2001 cruise. Comparison between these observations and values derived from several existing entrainment parameterizations is better than expected, suggesting that entrainment should be relatively well captured by models. The EPIC data is also used to construct a diurnal cycle of buoyancy flux profiles under the assumption of well-mixed conditions. These profiles, in conjunc-

tion with a comparison of the difference between cloudbase and lifting condensation level, suggest that drizzle is acting during EPIC to limit early-morning turbulent mixing.

We also perform a more in-depth comparison between a large-eddy simulation (LES) and the EPIC data. The LES was found to reproduce many features of the EPIC observations. In particular, budgets of boundary-layer moisture and energy, the diurnal cycle of subsidence, boundary-layer stratification, and the relation between buoyancy forcing and entrainment were well-simulated. The model was unable to reproduce the observed precipitation rates or diurnal cycle of boundary-layer depth. Sensitivity studies found subsidence to have little effect on liquid water path, which was significantly increased in simulations where drizzle was artificially decreased.

TABLE OF CONTENTS

LIST OF FIGURES

LIST OF TABLES

GLOSSARY

ALBEDO: The fraction of incoming solar radiation reflected back to space.

BOUNDARY LAYER: The layer of a fluid closest to a material surface where turbulent effects are important.

CLIMATE SENSITIVITY: The equilibrium change in global mean surface temperature following a unit change in radiative forcing.

CLOUD RADIATIVE FORCING: The change in net top-of-atmosphere radiative flux induced by the presence of cloud (i.e. flux without cloud minus observed flux).

DECOUPLED: Boundary-layer state when the cloud layer has stopped interacting with the subcloud layer. Opposite of well-mixed.

ENTRAINMENT: The rate of BL growth due to incorporation of free-tropospheric growth by overshooting BL eddies.

EULERIAN: A system of coordinates which is fixed in space for all time without any attempt to identify individual fluid parcels from one time to the next. See also Lagrangian.

LAGRANGIAN: A system of coordinates by which fluid parcels are identified for all time by assigning them coordinates which do not change with time. See also Eulerian.

LATENT HEAT FLUX: Water vapor flux scaled into energy units with the understanding that moisture flux takes energy from one area by evaporative cooling and transports it to another area which is warmed by condensational heating.

POTENTIAL TEMPERATURE (θ): The temperature a parcel would have if it were lifted or sunk adiabatically to the 1000 mb level.

REYNOLDS AVERAGE: Theoretical average of a quantity over an infinite number of realizations of the same experiment.

SENSIBLE HEAT FLUX: The potential temperature flux scaled into energy units.

SURFACE LAYER: The layer nearest the surface where mechanical production of turbulence exceeds buoyant production.

TURBULENT KINETIC ENERGY (TKE): The energy contained in turbulent motions. Typically described per unit mass as $1/2 \left(u^2 + v^2 + w^2\right)$ where u, v, and w are the east-west, north-south, and vertical motions.

WELL MIXED: BL state when mixing dominates stratifying effects resulting in quantities conserved under moist- and dry-adiabatic processes becoming constant in height.

ACKNOWLEDGMENTS

Chapter 1

INTRODUCTION

1.1 The Importance of Low Clouds

Clouds affect the earth's radiation budget in two opposing ways. On one hand, clouds generally have a higher albedo than the underlying surface, so they decrease the amount of solar radiation absorbed by the earth-atmosphere system and thus act to cool the planet. On the other hand, clouds also act to warm the planet by trapping infrared radiation near the surface. This occurs because (at a given wavelength) the strength of emitted radiation by any substance increases as the fourth power of its absolute temperature (e.g. Liou, 2002, p. 12). Since clouds absorb radiation from below (where it is warmer) and emit radiation in proportion to their (relatively colder) cloud-top temperature, they decrease the amount of radiation lost to space, thus decreasing the Earth-atmosphere system's ability to cool radiatively. The first of these effects is often called the albedo or shortwave (SW) effect, while the second is known as the longwave (LW) or greenhouse effect.

Since the greenhouse effect increases with cloud altitude, the SW and LW effects tend to cancel for high clouds, resulting in relatively weak cloud forcing. For low clouds (taken here to be clouds with tops lower than 2km) the cloud-top temperature is not significantly different than the surface temperature and the albedo effect dominates. As a result, low clouds exert a strong cooling effect on the planet. This effect is illustrated dramatically in Fig. 1.1, which compares the geographical distributions of low cloud with the cloud radiative forcing (CRF). This graphic shows definitively that the strongest CRF is associated with low clouds. Using the correlation between low cloud amount and net top-of-atmosphere (TOA) radiative flux derived in Klein and Hartmann (1993), one

2

a. Annual ISCCP C2 Inferred Low Cloud Amount   **b. Annual ERBE Net Radiative Cloud Forcing**

NO DATA 0   10   20   30   40   50   60   70   80   NO DATA -90   -70   -50   -40   -30   -20   -10   0   10   20   30   40

Percent   W/m**2
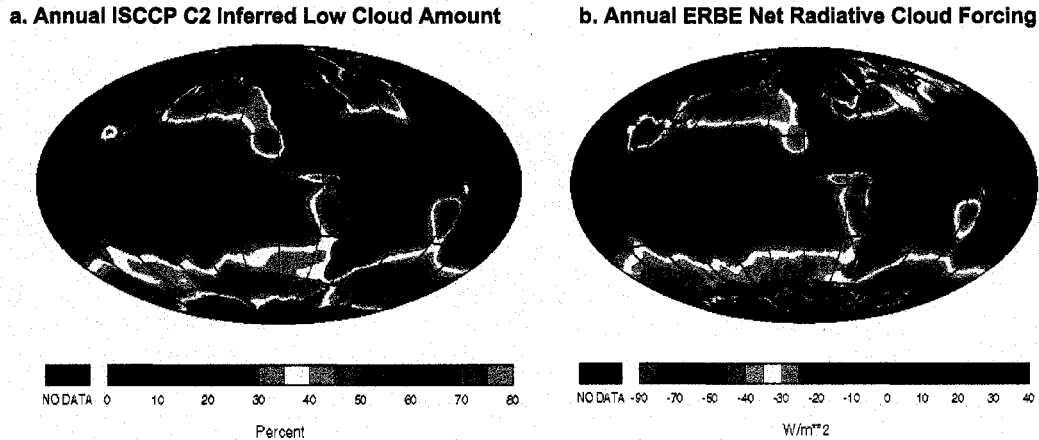
Figure 1.1: ISCCP-derived stratus low cloud amount (a) and ERBE net cloud forcing (b). Both graphics courtesy Dennis Hartmann.

can estimate that an increase of just 4% in global low cloud coverage would induce a TOA radiation imbalance sufficient to completely cancel the 4W m^{-2} direct radiative impact of carbon dioxide doubling. Similar results based on different data are presented in Randall et al. (1984),Hanson (1991), and Slingo (1990). In light of this strong climate sensitivity to changes in low clouds, understanding what affects low cloudiness is crucial to understanding our climate and how it may change.

Low clouds also play an important role in energy transport. These clouds generally form at the top of the atmospheric boundary layer (BL) and their presence has a significant impact on heat and moisture transfer between the surface, the BL, and the free troposphere. Additionally, Ma et al. (1996) found that increasing low cloudiness in the Southeast (SE) Pacific in the UCLA coupled ocean-atmosphere general circulation model (GCM) enhanced the strength of the tropical circulation which (by enhancing surface fluxes and equatorial upwelling) also caused a widespread decrease in East Pacific sea surface temperature (SST). Yu and Mechoso (1999) use a later version of the same model to conclude that proper simulation of the SE Pacific low cloud maximum is critical to removing the spurious southern branch of the Intertropical Convergence Zone (ITCZ) in
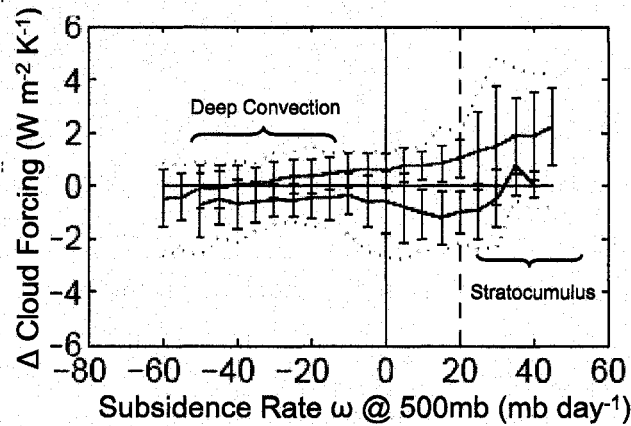
Figure 1.2: Sensitivity of net cloud forcing from 15 coupled ocean atmosphere GCMs as a function of 500mb ω. The blue (red) line is the mean over the 7 (8) models predicting a decrease (increase) in cloud forcing averaged over all ω. Errorbars are one standard deviation values. The envelope of the model runs is given by the dotted lines. Based on Fig. 2 from Bony and Dufresne (2005).

the UCLA GCM.

1.2 Current Understanding of Low-Cloud Feedbacks

Because even minor changes in low clouds result in significant changes to the earth's radiation budget (as noted above), low cloud response to global warming represents a potentially important climate feedback. Assessing the magnitude of cloud feedbacks has historically proven challenging (Cess et al., 1989), and is in fact still regarded as the largest source of uncertainty in the climate sensitivity of GCMs (Alley et al., 2007, p. 12). The partitioning of this uncertainty among cloud types is illustrated for tropical clouds in Fig. 1.2. To make this graphic, the net CRF and SST change for 15 coupled ocean-atmosphere GCMs has been calculated for each ocean gridpoint between 30°N and 30°S for both a control run and a run with CO_2 increasing by 1% per year. Linear regression is then used to compute the cloud forcing trend for a 1K SST increase for each gridpoint and the results are binned and displayed as a function of 500mb vertical pressure velocity ω. Since mean motion is upward ($\omega < 0$) in regions of deep convection while tropical low clouds form in regions of strong descending motion ($\omega > 0$), this binning process is useful for differentiating model response by cloud type. Since model spread is greatest in regions of positive ω, it appears that the most uncertain feedback in the tropics is

that due to low cloud changes (Bony and Dufresne, 2005). There is some indication that this situation extends to at least 60°latitude (Cess et al., 1997). Since cloud feedbacks are the largest source of climate change uncertainty and low clouds seem to be the least constrained cloud type, improving low cloud parameterization is the single most effective thing we could do to reduce uncertainty about climate change.

Since feedbacks involving low clouds have the potential to play such a major role in shaping our future climate, understanding these feedbacks is vitally important. Fig. 1.2 can be used to give us a sense of this response in GCMs. In this graphic, most of the models sampled predict that low cloud forcing will become less negative as the planet warms, constituting a positive feedback on warming. It should be noted, however, that the study resulting in Fig. 1.2 only examines a very small subset of available GCM data and that GCMs are continually evolving. In general, modeled low cloud response to global warming is extremely uncertain. This fact is underscored by the fact that another recent study of low clouds in the two top US GCMs (GFDL AM2 and NCAR CAM3) actually finds an increasing trend in low-cloud albedo (Zhu et al., 2007).

Observational data is also ambiguous. Norris (1999) finds an increase of 3.6% in global mean low cloud cover over the ocean between 1952 and 1995 from the surface observer record in the Comprehensive Ocean-Atmosphere Data Set (COADS), but cautions that this result may be an artifact of the record. International Satellite Cloud Climatology Project (ISCCP) data, on the other hand, show a decrease in low clouds in all latitude bands (Norris, 2005), but caution that at least some of this trend may be due to issues arising from the temporal evolution of satellite viewing angle bias, a problem substantiated by Campbell (2004) and Evan et al. (2007). Nonetheless, independent satellite measurements from the Earth Radiation Budget satellite show a slight decrease in TOA reflected SW radiation, which supports the view that low cloudiness has decreased (Norris, 2005). Another way scientists have attempted to divine the low cloud tendency is from observed low cloud response to shorter term climate anomalies such as the El Niño-Southern Oscillation (e.g. Oreopoulos and Davies, 1993). This technique is inappropriate because, as noted in Zhu et al. (2007), low clouds respond to the ocean-wide pattern of

SST change as well as the local SST. In short, the sign of low cloud response to global warming is still very unclear.

1.3 Geographic Distribution of Low Clouds

To have any hope of understanding low cloud changes, we must first understand the conditions under which low clouds exist. A useful starting point is the geographic distribution of low cloud in Fig. 1.1a. An obvious feature of this graphic is that low clouds tend to form over the ocean. In fact, the surface observer record tells us that low cloud coverage is 34% over ocean, but only 18% over land (Klein and Hartmann, 1993). The one exception to this rule is the small maximum in low cloudiness found in the southeastern Chinese plain in winter. Oceanic low clouds appear most frequently in four different regimes. Maxima over the high latitude oceans occur mainly in the spring and summer, when warm (and thus relatively moist) air from lower latitudes flows over melting pack ice and is cooled to saturation by turbulent mixing (Houze, 1993). Other maxima in low clouds are found to the east of the midlatitude continents in winter. These clouds form when cold continental air flows over the warm western boundary currents (Agee et al., 1973). Klein and Hartmann (1993) note that a third maximum of low-cloud fraction appears over the midlatitude oceans in the summer and ascribe this feature to sinking motions over the ocean driven by land-sea contrast. Finally, extensive sheets of stratocumulus (Sc) form to the west of the subtropical continents where subsiding warm air in the downward branch of the Hadley and Walker circulations meets a sea surface which has been cooled by upwelling and equatorward ocean currents.

This last regime is the focus of my thesis. Subtropical Sc are a useful starting point for understanding low cloud feedbacks because they form in a relatively steady large-scale circulation, which simplifies analysis. Further, most previous Sc research has focused on these clouds, so observational data is readily available. Additionally, subtropical Sc have a clear impact on the tropical circulation (as mentioned in Section 1.1), so improved understanding of this region has clear utility from a general circulation perspective. Finally, there is some indication that the tropics drive global variability (Sterl and Hazeleger,

2005), so understanding tropical changes may be a prerequisite for understanding the whole climate system. This last conclusion is supported by the fact that El Niño, which is tropically forced, has such profound effects on midlatitude weather.

1.4 The Subtropical Sc-Topped BL

In order to understand subtropical stratocumulus cloud feedbacks, a deeper understanding of the Sc-topped BL is required. In this regime, the combination of a warm free troposphere and a cold sea surface results in the formation of a strong inversion. The presence of this inversion encourages cloud formation by limiting the escape of BL moisture and turbulent kinetic energy (TKE) to the free troposphere. As a result, the Sc-topped BL tends to be a fairly moist region with a great deal of turbulent mixing. Frequently, mixing is sufficient to overpower any stratifying effects with the result that quantities conserved under both moist and dry adiabatic processes become independent of height throughout the BL. In this case the BL is said to be *well mixed*. Mixing encourages Sc formation by transporting moisture from the surface to the BL top where clouds form. The presence of large-scale subsidence in the Sc regions enhances turbulence by forcing the BL to remain shallow, thus increasing the energy per unit area available for mixing.

Paradoxically, the TKE required for the maintenance of Sc results largely from buoyant accelerations driven by the presence of the cloud itself. As a result, some synoptic conditions which support a steady Sc-topped BL also support a stable cloud-free solution (Randall and Suarez, 1984). This fact is the bane of Sc modelers because once cloud disappears from a simulation (e.g. during initialization) it may not return for quite a while. TKE can also be produced by shear (which doesn't depend on the pre-existence of cloud), but in subtropical Sc this mechanism for turbulence generation is typically only important in the surface layer.

Buoyancy generation of TKE is described by the buoyancy flux $\mathcal{B} = \overline{w'b'}$, the covariance between vertical velocity w and the buoyancy $b = g\theta'_v/\theta_{\text{ref}}$. Here the overbar denotes a Reynolds average and primes denote deviations from this average. In this last equation, g is the gravitational acceleration, θ_{ref} is a reference potential temperature, and
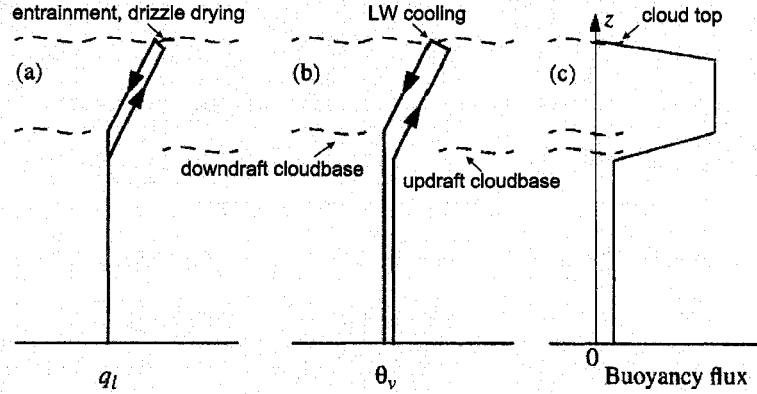
Figure 1.3: Circulation path for an idealized parcel in a steady-state Sc-topped BL. Dashed lines indicate cloud top and cloudbase for updrafts (indicated by upward arrows) and downdrafts (indicated by downward arrows). Panel (a) shows parcel q_l and panel (b) shows θ_v for updrafts and downdrafts, while panel (c) shows the resulting buoyancy flux profile. From Bretherton (1997).

θ_v is the virtual potential temperature (the potential temperature corrected to include the density effects of liquid water q_l and water vapor q_v). The main source of buoyancy flux in the Sc-topped BL is LW cooling in the strongly emissive cloudy air just below the BL top. This cooling causes cloud-top air to become negatively buoyant and sink, as diagrammed in Fig. 1.3b. Due to a process called entrainment, however, the magnitude of the observed cloud-top cooling is substantially diminished from that predicted on the basis of LW divergence alone. Entrainment (w_e) is the rate at at which turbulent eddies overshooting the inversion drag free-tropospheric air with them as they sink back into the BL. Since free-tropospheric air in the subtropics is substantially warmer than air in the Sc-topped BL, entrainment causes the BL to warm, opposing the effect of radiative cooling. Free-tropospheric air is also frequently much drier than BL air, though, with the result that entrainment also induces evaporative cooling as cloud water mixes with subsaturated entrained air. The net effect of the LW cooling and entrainment is to produce downdrafts below cloud top which are much colder than updrafts, resulting in a strongly positive buoyancy flux in this region (Fig. 1.3c).

In the interior of the cloud, temperature changes moist adiabatically with height

(assuming the BL is well-mixed), so the difference between updraft and downdraft θ_v (and hence the buoyancy flux) remains approximately constant. Because updrafts are moistened by contact with the sea surface and downdrafts are dried by entrainment, the downdraft cloud base tends to be higher than that for updrafts (Fig. 1.3a). In the region between these cloudbases, updrafts experience substantial condensational warming as they rise while downdrafts sink at a constant θ. As a result, the buoyancy flux transitions in this region from the high values found in cloud to lower values below. The subcloud $\mathcal{B}$ is mainly the result of updrafts being warmed by surface sensible heating. This surface heating is relatively weak because efficient mixing keeps the SST just a degree or so colder that the surface.

Several processes may cause the BL to deviate from the idealized, well-mixed structure described above. For example, during the day clouds absorb SW radiation, which offsets the net cooling described above and decreases TKE. Since the height at which SW radiation is absorbed tends to be lower in the cloud than that of LW emission, SW absorption can destabilize the cloud layer (causing more entrainment warming) while cutting off turbulence across cloud base (e.g. Ciesielski et al., 2001). Frequently SW absorption is strong enough to halt mixing across cloudbase, a situation called diurnal decoupling (Nicholls, 1984).

A second potentially important process is drizzle. By removing liquid water from downdrafts, drizzle tends to increase the difference between updraft and downdraft cloudbase. If this difference becomes large enough, the subcloud downdraft θ_v in Fig. 1.3b will rise above the updraft θ_v and mixing will be retarded below cloud base (Stevens et al., 1998). Further, drizzle induces a pattern of condensational heating above cloudbase and evaporative cooling below which acts to stabilize the cloud base against mixing.

A third potential stabilizing process is surface moisture flux (Bretherton and Wyant, 1997). By moistening updrafts, enhancement of surface latent heat flux (LHF) results in an enhanced updraft/downdraft cloudbase asymmetry which, through the same arguments used for drizzle, results in decreased subcloud buoyancy flux. The process through which increased surface moisture flux creates warm downdrafts below cloudbase is a bit

subtle and serves as a nice illustration of the strong coupling between the BL moisture and θ budgets. For the moisture budget to remain closed as a parcel completes a circuit in Fig. 1.3, moisture added to updrafts near the surface must be removed somewhere else along the parcel trajectory. This can happen by enhanced precipitation (which warms downdrafts through latent heat release) or enhanced entrainment (which warms downdrafts by incorporating warm free-tropospheric air). Through both pathways, changes in the BL moisture budget project onto the BL θ budget. These budgets and their interaction are discussed in more detail in Chapter 2.

1.5 Possible Mechanisms for Sc Feedback

A number of mechanisms whereby low clouds might change in response to anthropogenic forcing have been suggested over the years. Many of these theories have focused on cloud response to aerosol changes because increased aerosol in ship exhaust often results in obvious changes in cloud properties, proving dramatically that such feedbacks exist and providing a natural laboratory for investigating these effects (e.g. Radke et al., 1989). Cloud-aerosol feedbacks also have great relevance to the larger question of global warming because there is some evidence that aerosol-induced albedo increases are partially masking the warming effects of rising CO_2 (e.g. Charlson et al., 1992).

Although aerosols directly impact clouds by heating the cloud layer through absorption of solar radiation, this effect is generally found to be negligible (e.g. Ackerman and Toon, 1996; Coakley and Walsh, 2002). Because aerosols serve as the cloud condensation nuclei (CCN) upon which cloud droplets form and grow, however, changes to the aerosol distribution can still have a large effect on cloud properties. As noted by Twomey (1977), for a fixed amount of liquid water, an increase in CCN implies that the liquid is divided into a larger number of smaller drops. This repartitioning results in an increase in the scattering cross-section presented by the cloud and thus an increase in albedo. This effect is known as the Twomey or first indirect aerosol effect. Additionally, Albrecht (1989) noted that larger cloud droplets coalesce more efficiently to drizzle-drop size (radii>20 μm), so increased CCN should result in decreased drizzle. Since drizzle removes water

from the cloud and stabilizes the subcloud layer through condensation and evaporation, Albrecht concluded that the decrease in drizzle due to increased CCN should have an additional moistening effect on Sc, enhancing the increase in albedo from the Twomey effect. The impact on cloud albedo of aerosol-induced drizzle changes is thus known as the Albrecht or second indirect aerosol effect. While it is indisputable that CCN changes have a strong impact on drizzle and thereby on Sc properties, it is not clear that this effect is to decrease cloud water. Ackerman et al. (2004) note that while drizzle that reaches the surface dries the BL and decreases LWP, drizzle which evaporates in the BL decreases TKE, reducing entrainment drying and thus *increasing* LWP. When little drizzle reached the surface, this second effect was found to dominate in their large eddy simulation (LES) results, resulting in decreased cloud water at higher CCN. This result was investigated further in a simplified (mixed-layer) context by Wood (2007a), who found that cloud thickness only decreased with increasing CCN when cloud base was high (so little precipitation reached the surface) and only as a transient response. Over longer timescales, increased CCN was always found to increase cloud thickness (although the reasons for this are still unclear).

A more limited number of studies have focused on the impact of global warming on Sc. This problem is more difficult because cloud amount is intimately tied to local SST as well as to to free-tropospheric temperature, moisture and subsidence profiles - all of which will probably change as the planet warms. As a result, a complete understanding of subtropical Sc response to global warming requires an understanding of how warming will affect the entire tropical circulation. Currently, most of our understanding about subtropical Sc change is based on the empirical relationship between lower tropospheric stability (LTS, defined as $\theta|_{700mb} - \theta|_{surf}$) and cloud amount noted by Klein and Hartmann (1993). This relation is highly correlated to inversion strength, which has also been used as a low cloud predictor (Slingo et al., 1989; Wood and Bretherton, 2006). While LTS can explain a substantial fraction of the variance in Sc amount on daily to interannual timescales, it seems unlikely that this measure is the sole factor controlling Sc. In particular, Stevens et al. (2007) suggest that LTS might be less relevant in the

heart of the Sc regions, where cloud fraction is always close to one. Wood and Brether-
ton (2006) point out that different inversion strength measures respond differently to
a uniform global warming because they vary in how they account for the increase in
static stability of the lower troposphere expected in a warmer climate. Another poten-
tial warming feedback was posited by Somerville and Remer (1984). They noted that
observationally, the amount of water held by a cloud of given cloudbase and cloud top
increases at warmer temperatures. The impact of this last feedback on low cloud albedo
has yet to be rigorously tested.

1.6 The EPIC Dataset

The East Pacific Investigation of Climate (EPIC) Sc field campaign (Bretherton et al.,
2004), which took place in October 2001 aboard the NOAA vessel Ronald H. Brown
(RHB), provides a new dataset for answering some of the open questions regarding Sc
and climate. Except for one earlier and less instrumented cruise into the south edge of
the SE Pacific Sc region (Garreaud et al., 2001), the EPIC cruise was the first to provide
extensive documentation of conditions in this region - the location of the largest sheet
of subtropical Sc on Earth (Fig. 1.1a). A centerpiece of this campaign was a set of
three-hourly rawinsonde profiles taken between Oct. 16th and 22nd, when the RHB was
collocated with a Woods Hole Oceanographic Institute (WHOI) buoy at 20°S, 85°W.
Fig. 1.4 shows profiles of θ and q_v from these sondes. These profiles show two surprising
features. First, the BL top shows a very strong and regular diurnal cycle. This cycle is
much stronger than that found in the better studied Northeast (NE) Pacific and suggests
that there are important geographical variations between subtropical Sc regions. The
second important feature in Fig. 1.4 is the well-mixedness of the profiles (best observed
below cloudbase since neither θ nor q_v is adiabatically conserved in cloud). This lack of
stratification was unexpected since BLs deeper than 1 km were typically found in previous
campaigns to have substantial stratification (e.g. Albrecht et al., 1995a). This well-mixed
structure greatly simplifies the analysis of BL turbulence performed in Chapter 2.

In addition to the sonde data, precipitation profiles and horizontal cross-sections for
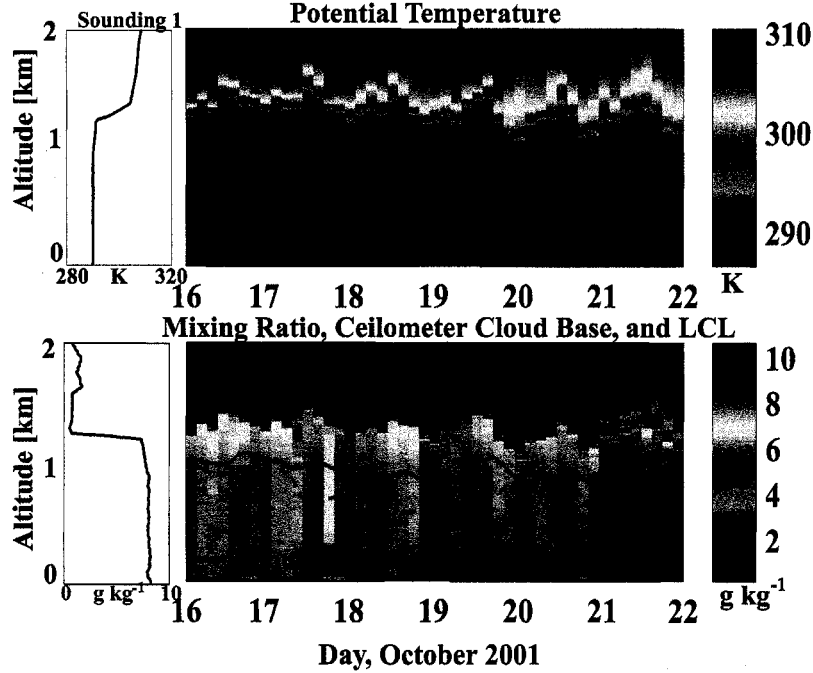
Figure 1.4: Potential temperature and moisture profiles from the EPIC radiosondes at 20°S 85°W. Also included are cloud base and surface lifting condensation level (LCL, shifted up 150m to account for stratification in the surface layer).

the study period were obtained from vertically pointing 8 mm and scanning 5 cm wavelength radars (Comstock et al., 2004), liquid water path (LWP) was derived from a microwave radiometer (Zuidema et al., 2005), and cloudbase was obtained from a ceilometer. These quantities, along with a host of other ship-based measurements, provide a rich dataset for furthering our understanding of this important cloud type. We have synthesized this data into a "modeler's EPIC Sc dataset", available at http://www.atmos.washington.edu/∼caldwep/r search/ScDataset/sc_integ_data_fr.htm.

1.7 Coordinate Systems

Choosing a vertical coordinate system for this thesis has been a challenge. In previous studies of the Sc-topped BL, a Boussinesq framework with geometric height coordinate z has generally been used. While appropriate for the shallower BLs these studies have

focused on, the error involved in this approximation becomes significant for BLs of the depth observed during EPIC. Nonetheless, there are several good reasons for using a geometric height coordinate. First, the bulk of the Sc literature is based on this coordinate, so quantities such as entrainment and buoyancy flux are generally defined relative to this system. Further, we use geometric coordinates all the time in our daily lives, so we are most familiar with this system. Finally, the Boussinesq system provides a simple framework for understanding the qualitative behavior of our system of interest.

For quantitative accuracy when analyzing the deeper EPIC BL or for understanding the large-scale flow influencing subtropical Sc, a system based on pressure coordinates p is more appropriate. This framework, which accounts for density variation with height, can be related to z through the hydrostatic relation

$$\frac{\partial p}{\partial z} = -\rho g \tag{1.1}$$

where ρ is the density of air. Near the surface $\rho g \approx 0.1\text{mb m}^{-1}$, so each 10m increase in z is equivalent to a decrease of about 1 mb in p. In order to improve this analogy between height and pressure, we introduce a 'pressure-height' coordinate $\hat{p} = p_0 - p$ equal to the difference between the instantaneous surface pressure p_0 and the actual pressure. Differences between any two heights in this coordinate system have the same magnitude as differences in p (resulting in accurate results), but $\hat{p}$ increases upward in the familiar manner of z. For the remainder of this thesis, we will switch back and forth between these three coordinate systems as required to provide simple, yet quantitatively accurate results.

1.8 Goals of this Work

As noted in Section 1.4, entrainment has an important effect on BL depth and on turbulent mixing. Further, entrainment warming and drying play a dominant role in the BL energy and moisture budgets, as documented for EPIC in Chapter 2. In light of these central roles, accurate measurement and parameterization of entrainment is key to understanding and simulating subtropical Sc. In fact, Stevens et al. (2005b) conclude for LES

that "if for a given forcing a simulation can be made to predict the correct entrainment rate, other aspects of the simulation are likely to be in better accord with the data". Unfortunately, entrainment is very hard to measure since it is a small-scale turbulent process which takes place hundreds of meters above the ocean surface. Most observational estimates of entrainment have historically been made from airplanes (Nicholls and Turton, 1986; Kawa and Pearson, 1989; Bretherton et al., 1995; de Roode and Duynkerke, 1997; Boers et al., 1997; Faloona et al., 2005), though a tethered balloon (Roach et al., 1982) and satellite data (Wood and Bretherton, 2004) have also been used. Because of the logistical difficulties associated with these instruments, relatively few entrainment measurements have been made. Further, all known in-situ methods for measuring w_e are subject to large errors that are hard to quantify. Attempts have been made to measure entrainment in a laboratory tank of fluid stratified into two layers by heating the upper layer from below (McEwan and Paltridge, 1976; Sayler and Breidenthal, 1997), but the analogy to turbulence in the Sc-topped BL is imperfect because the Prandtl and Reynolds numbers of the working fluid are quite different than air and the heating and cooling associated with phase changes are neglected is neglected in these experiments.

Given the lack of reliable entrainment observations, it is unsurprising that there is no consensus about how to parameterize entrainment in models. As an example of the extent of this uncertainty, Stevens (2002) found steady-state LWP values for a mixed-layer model using different entrainment parameterizations to vary by a factor of two. The difficulty in parameterizing entrainment results from more than a simple lack of entrainment observations. Even in cases where entrainment estimates are available, the conditions giving rise to the observed entrainment are generally not captured and there is no clear way to separate the contributions to entrainment from different physical processes such as radiation, drizzle, etc. For this reason, the factors which influence entrainment are still somewhat mysterious. In particular, the role of LW cooling in the intermittently turbulent entrainment interface layer is not well observed or understood. There is also controversy about how evaporative cooling associated with mixing between free-tropospheric and BL air influences the entrainment process. VanZanten and Duynkerke (2001) suggest that

the LW effect dominates, while Nicholls and Turton (1986) and Lilly (2002a) stress the role of evaporative cooling. Further, there is some debate as to the lengthscale of the eddies involved in the entrainment process (e.g. compare Lewellen and Lewellen (1998) to Lilly (2002b)). Further discussion of how these uncertainties are addressed in current entrainment parameterizations is included in Chapter 2.

Partially as a response to the uncertainty involved in entrainment parameterization, LES, which handles the entrainment process without explicitly invoking an entrainment parameterization, has become a popular method for modeling subtropical Sc. However, because entrainment occurs on small scales (which are themselves parameterized in LES), it is unclear that LES predicts entrainment rate better than empirical entrainment closures (e.g. Stevens et al., 2005b). Indeed, for the the DYCOMS RF01 intercomparison, the variability in LES LWP was every bit as big as for single-column model experiments (Zhu et al., 2005).

Since entrainment is so important to the evolution of the Sc-topped BL and yet so poorly understood, the first priority of this thesis is to derive additional estimates of w_e from the EPIC data and to use these to evaluate existing entrainment parameterizations. This work is the focus of Chapter 2. The skill of an LES in predicting the time variation of entrainment during the 6 days of EPIC is considered further in Chapter 3.

Another uncertain process in the Sc-topped BL is drizzle. Because surface precipitation is generally weak in the subtropical Sc region, drizzle was ignored in early models of Sc (Lilly, 1968; Moeng, 1984). However, subtropical Sc field experiments such as FIRE (Albrecht et al., 1988), ASTEX (Albrecht et al., 1995a), DYCOMS-II (Stevens et al., 2003), and EPIC (Bretherton et al., 2004) have frequently observed significant drizzle from Sc, particularly when cloud droplet concentrations were low. Further, even if drizzle evaporates before reaching the surface, precipitation can have a profound effect on BL dynamics by decreasing BL TKE (as described in Section 1.4). Because drizzle damps mixing across cloudbase, heavily precipitating Sc tends to be *cumulus-coupled* - broken into separate cloud and subcloud layers which communicate only through intermittent cumulus convection originating from the near-surface destabilization caused by evapora-

tion (Jiang et al., 2002; Stevens et al., 1998). This effect seems to be associated with mesoscale cloud organization which may have important impacts on albedo (Paluch and Lenschow, 1991; Comstock et al., 2005; Savic-Jovcic and Stevens, 2007).

By influencing BL TKE, drizzle also affects w_e. The influence of drizzle-induced changes in entrainment on cloud LWP is a subject of continuing research and seems to depend on meteorological conditions (Randall, 1984; Pincus and Baker, 1994; Ackerman et al., 2004; Wood, 2007a; Bretherton et al., 2007). Since drizzle rates decrease rapidly with increasing CCN, these dynamic impacts of drizzle are a primary component of the second indirect aerosol effect described in Section 1.5. As such, satellite composite studies of ship tracks provide a natural testbed for examining these effects. Such studies suggest that the impact of drizzle varies greatly from location to location (Coakley and Walsh, 2002), though the generalization of these studies may be limited by the difficulty in choosing an appropriate sample of tracks (Ackerman et al., 2000). The combination of drizzle profiles and inferred entrainment rate timeseries obtained during EPIC provide a golden opportunity to observationally test models of how drizzle affects entrainment. The impact of drizzle on BL structure is examined observationally in Chapter 2 by examining mixed-layer buoyancy flux profiles. An LES sensitivity study of the of the EPIC BL response to changed CCN concentration is included in Chapter 3.

As mentioned in Section 1.6, the BL observed during EPIC had an impressively large and regular diurnal cycle. Diurnal variation in cloud properties are important to capture in models because clouds only reflect and absorb sunlight during daylight hours. In addition, diurnal variation is an excellent test for climate models since it is an observable and reproducible response to radiative forcing (Randall et al., 2003). Observations (e.g. Hignett, 1991; Rozendaal et al., 1995; Wood et al., 2002) show that cloud fraction and LWP in subtropical Sc tend to peak in the early morning hours, a result ascribed primarily to daytime solar absorption. These studies show a much stronger diurnal cycle in the southern hemisphere Sc regions than in the north, however, which suggests that effects other than solar zenith angle must be playing a role as well. It seems likely that these additional factors vary by region. For example, Ciesielski et al. (2001) noted that the

timing of the diurnal cycle of subsidence seems to vary from region to region throughout the North Atlantic and Garreaud and Muñoz (2004) have shown that the diurnal cycle of subsidence is particularly pronounced in the EPIC region in response to slope heating over the Andes. Further, while it is clear that the diurnal cycle is driven by variation in solar radiation which acts to decrease daytime mixing (Turton and Nicholls, 1987; Hignett, 1991), the pathway through which this occurs is still a matter of active research and probably depends on local factors such as BL depth and cloud thickness. Because of the large suite of data collected during EPIC and the strength and repeatability of the observed diurnal cycle, the EPIC campaign provides an excellent opportunity to further our knowledge about diurnal changes to the Sc-topped BL. In Chapter 2, diurnal variation in the BL mass, moisture, and energy budget are used to investigate how the BL responds to variations in insolation. In particular, the availability of precipitation profiles allows us to determine for the first time how diurnal variations in drizzle affect BL evolution. In Chapter 3, an LES is used to simulate a 6-day period of EPIC. Sensitivity studies are performed to isolate the relative roles of subsidence and solar absorption in determining the observed diurnal variation in BL depth and cloud thickness, and the impact of CCN change son the cloud thickness over the diurnal cycle.

Finally, the question of subtropical Sc response to anthropogenic greenhouse gas and aerosol forcing is considered directly in Chapter 4. In this Chapter, a simple model based on our improved understanding of drizzle and entrainment is used to predict an increase in the albedo of subtropical Sc. This discussion is followed by conclusions in Chapter 5.

Chapter 2

MIXED-LAYER BUDGET ANALYSIS OF THE DIURNAL CYCLE OF ENTRAINMENT IN SE PACIFIC STRATOCUMULUS

2.1 Introduction

As noted in section 1.6, the EPIC field campaign provides an excellent opportunity to explore some of the key issues surrounding the subtropical Sc-topped BL. In this Chapter, we use BL-averaged budgets of mass, moisture, and energy constructed from the EPIC data to understand the strong diurnal modulation of BL properties noted in Chapter 1. We pay particular attention to deducing the diurnal cycle of entrainment and buoyancy flux and to analyzing the role of drizzle processes both in the budgets and in BL mixing. Our methodology is explained in section 2.2, the relevant data is described in section 2.3, and results are displayed in section 2.4.

2.2 Methodology

2.2.1 Budget Equations and Entrainment Rates

The variables used for this study are BL depth, total water mixing ratio $q_t = q_v + q_l$, and liquid water static energy $s_l = c_p T + gz - L q_l$. In this last equation, T, c_p, and L are (respectively) the absolute temperature, the isobaric heat capacity of dry air, and the latent heat of water vaporization. Although c_p varies slightly with q_t and L varies slightly with T, these variations are minor so constant values of 1004 J kg^{-1} K^{-1} and 2.5×10^6 J kg^{-1} are assumed in this study. These thermodynamic budgets are based on variables approximately conserved under adiabatic displacements and phase changes. Because the BL during EPIC was fairly deep, we use the 'pressure-height' coordinate $\hat{p}$ described in section 1.7 to avoid the small but quantitatively significant errors associated with a constant-density assumption. Under this framework, we arrive at horizontally-

and BL-averaged budget equations for q_t and s_l (derived in appendix A)

$$\hat{p}_i\left[\frac{\partial\langle q_t\rangle}{\partial t} + \langle \mathbf{v}\cdot\nabla_h q_t\rangle\right] - g\frac{\text{LHF}}{L} - gF_P(0) - \hat{\omega}_e\Delta q_t = [\langle q_t\rangle - q_{t-}]\,\mathbf{v}\cdot\nabla_h\hat{p}_i \qquad (2.1)$$

$$\hat{p}_i\left[\frac{\partial\langle s_l\rangle}{\partial t} + \langle \mathbf{v}\cdot\nabla_h s_l\rangle\right] - g\text{SHF} + gLF_P(0) + g\Delta_{\text{BL}}F_R - \hat{\omega}_e\Delta s_l = [\langle s_l\rangle - s_{l-}]\,\mathbf{v}\cdot\nabla_h\hat{p}_i \quad (2.2)$$

where the operator $\langle x\rangle$ denotes the mass-weighted BL average of a given quantity x, $\mathbf{v}\cdot\nabla_h x$ represents the horizontal advection of x into our layer of interest, Δx is the difference between the value of x just above the BL-capping inversion and $\langle x\rangle$, and x_- is the value of x just below the inversion. In addition, $F_P(\hat{p})$ (negative for downward flux) is the horizontally-averaged precipitation rate at pressure-height $\hat{p}$ (in cloud, precipitation is taken to be the total liquid water flux including droplet sedimentation) and $\Delta_{\text{BL}}F_R = F_R(\hat{p}_i) - F_R(0)$ is the divergence of net radiative flux (positive upward) between the BL top, $\hat{p}_i$, and the surface. The entrainment rate is expressed here in $\hat{p}$-coordinates as $\hat{\omega}_e = \rho g\,w_e$.

In an idealized mixed layer, the conserved quantities are equal to their BL-averaged value everywhere below $\hat{p}_i$, so mixed-layer analyses typically neglect the terms on the right-hand side of (2.1) and (2.2). In the present study, we have estimated the effect of these terms to always be less than 2 W m^{-2}, which is small compared to the other budget terms and to the measurement uncertainty (see Tables 2.1 and 2.2). For this reason, the rest of this Chapter focuses on the mixed-layer version of these equations. A schematic showing the fluxes which contribute to each mixed-layer budget is included in Fig. 2.1.

Using observationally-derived estimates of the surface and precipitation fluxes and inferring radiative fluxes from observed thermodynamic and liquid water profiles (described in detail in section 2.3.2), we can estimate all terms in (2.1) and (2.2) except the entrainment fluxes. Thus estimates of $\hat{\omega}_e$ may be derived as budget residuals of (2.1) and (2.2). A third independent estimate of $\hat{\omega}_e$ may be obtained from the BL mass budget. BL mass (given by $\hat{p}_i/g$ in the current coordinate system) changes as a result of imbalance between mass influx due to entrainment and mass outflux, equal to the subsidence rate
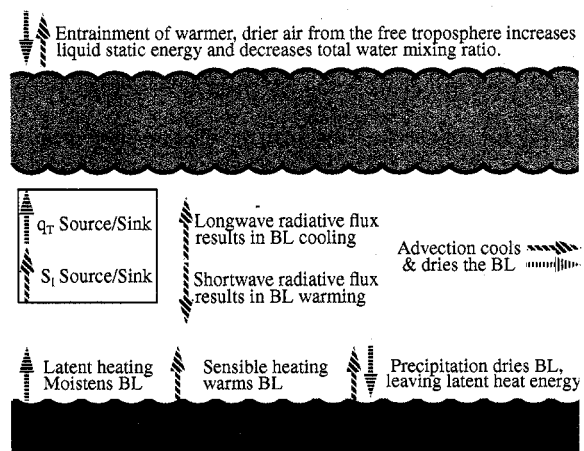
Figure 2.1: Schematic of BL indicating sources and sinks of $\overline{q_t}$ and $\overline{s_l}$.

Table 2.1: Mean and standard deviation (over all 6 days of sampling) for each term in the q_t budget (2.1). Entrainment rates are taken from the ECMWF mass budget. Each term has been scaled into W m^{-2} for ease of comparison with the s_l budget and, with the exception of $-L\hat{p}_i/g\, \partial\langle q_t\rangle/\partial t$, is signed so a positive value indicates an increase in BL moisture.

	$-\dfrac{L\hat{p}_i}{g}\dfrac{\partial\langle q_t\rangle}{\partial t}$	$-\dfrac{L\hat{p}_i}{g}\langle \mathbf{v}\cdot\nabla_h q_t\rangle$ ECMWF/NCEP	LHF	$LF_p(0)$	$\dfrac{L}{g}\hat{\omega}_e\Delta q_t$ ECMWF/NCEP	Residual ECMWF/NCEP
Mean:	-6	-26/-50	99	-5	-68/-61	-6/-23
St. Dev:	9	7/2	2	1	10/8	15/12

Table 2.2: As for Table 2.1, but for the s_l budget (2.2).

	$-\dfrac{\hat{p}_i}{g}\dfrac{\partial\langle s_l\rangle}{\partial t}$	$-\dfrac{\hat{p}_i}{g}\langle \mathbf{v}\cdot\nabla_h s_l\rangle$ ECMWF/NCEP	SHF	$-LF_p(0)$	$-\Delta_{BL}F_{SW}$	$-\Delta_{BL}F_{LW}$	$\dfrac{1}{g}\hat{\omega}_e\Delta s_l$ ECMWF/NCEP	Residual ECMWF/NCEP
Mean:	1	-19/-20	14	5	26	-78	41/37	-10/-15
St. Dev:	3	3/1	1	1	1	1	6/5	8/6

$\hat{\omega}_s$ by continuity. Thus $\hat{\omega}_s = \partial \hat{p}_i / \partial t$. In equation form this reduces to

$$\frac{\partial \hat{p}_i}{\partial t} + \mathbf{v} \cdot \nabla_h \hat{p}_i = \hat{\omega}_e + \hat{\omega}_s. \tag{2.3}$$

By using radar data, satellite measurements, and large-scale gridded analyses to estimate $\partial \hat{p}_i / \partial t$, $\mathbf{v} \cdot \nabla_h \hat{p}_i$, and $\hat{\omega}_s$, respectively (all described in section 2.3.1), we are able to diagnose $\hat{\omega}_e$ from (2.3). The consistency of the entrainment rates inferred from each of the three budgets is an important check on the plausibility of our results.

2.2.2 Turbulent Flux Profiles

Conserved-Variable Fluxes

For the BL to remain well mixed, $\partial q_t / \partial t + \langle \mathbf{v} \cdot \nabla_h q_t \rangle$ and $\partial s_l / \partial t + \langle \mathbf{v} \cdot \nabla_h s_l \rangle$ must be height-independent. Since the time change of a quantity at any point in space is given by the convergence of its flux function, well-mixedness implies that if horizontal advection is constant in height (an assumption we make), the flux convergence of q_t and s_l must be constant in height, or equivalently, that these fluxes must themselves be linear functions of $\hat{p}$. In terms of our mixed-layer budgets, the flux function for q_t is

$$W(\hat{p}) = \overline{\hat{\omega}' q_t'} + g \, F_P(\hat{p}), \tag{2.4}$$

and for s_l it is

$$E(\hat{p}) = \overline{\hat{\omega}' s_l'} + g \left[F_R(\hat{p}) - L \, F_P(\hat{p}) \right]. \tag{2.5}$$

If (2.4) and (2.5) vary linearly with $\hat{p}$, $W(\hat{p})$ and $E(\hat{p})$ are uniquely determined by their surface and cloud-top values so

$$W(\hat{p}) = g \left[\frac{\text{LHF}}{L} + F_P(0) \right] \left(1 - \frac{\hat{p}}{\hat{p}_i} \right) - \hat{\omega}_e \Delta q_t \frac{\hat{p}}{\hat{p}_i}, \tag{2.6}$$

$$E(\hat{p}) = g \left[\text{SHF} - L F_P(0) + F_R(0) \right] \left(1 - \frac{\hat{p}}{\hat{p}_i} \right) + \left[g \, F_R(\hat{p}_i) - \hat{\omega}_e \Delta s_l \right] \frac{\hat{p}}{\hat{p}_i}. \tag{2.7}$$

By substituting (2.6) and (2.7) into (2.4) and (2.5) and solving for the corresponding turbulent fluxes, equations for the turbulent flux profiles of q_t and s_l may be obtained.

Buoyancy Fluxes and Convective Velocity

As described in section 1.4, buoyancy flux $\mathcal{B}$ is the main source of TKE in the subtropical stratocumulus-capped BL. In $\hat{p}$ coordinates, the buoyancy flux can be written

$$\mathcal{B} = \frac{1}{\rho \, s_{v0}} \overline{\hat{\omega}' s_v'}. \tag{2.8}$$

Here, the virtual static energy $s_v = c_p T_v + gz$ is defined in terms of virtual or 'density' temperature (including liquid loading) $T_v = T + T_{\text{ref}}(\delta q_v - q_l)$, where $\delta = 0.608$ and $T_{\text{ref}} = 290\text{K}$. The term s_{v0} is a reference virtual static energy (taken here to be 290 kJ kg^{-1} - the mean over all soundings of s_v at $\hat{p} = 50$ mb).

We now relate $\mathcal{B}$ to the conserved variable fluxes following Bretherton and Wyant (1997) but working in terms of liquid static energy rather than moist static energy. Using the definition $s_l = c_p T + gz - L q_l$, s_v may be rewritten as

$$s_v = s_l + (1 - \epsilon) L q_l + \delta \epsilon L q_v \tag{2.9}$$

where $\epsilon = c_p T_{\text{ref}} / L \approx 0.1$. Expressing this quantity in terms of the conserved variables is particularly simple below cloud base, as $q_l = 0$ and thus $q_v = q_t$. Within the cloud, q_v is assumed equal to the saturation mixing ratio, q_s, so that

$$\begin{aligned} q_v' &= \frac{\partial q_s}{\partial T} T' \\ &= \frac{1}{c_p} \frac{\partial q_s}{\partial T} \left[s_l' - L \left(q_t' - q_v' \right) \right]. \end{aligned}$$

Solving this last equation for q_v' and setting $\gamma = L/c_p \, \partial q_s / \partial T$, we can express (2.9) in terms of s_l' and q_t' in the cloud layer. Together, the sub-cloud and in-cloud forms of (2.9)

imply

$$\overline{\hat{\omega}'s_v'} = \begin{cases} \overline{\hat{\omega}'s_l'} + \delta\epsilon L\overline{\hat{\omega}'q_t'}, & 0 \leq \hat{p} < \hat{p}_{cb} \\ \beta\overline{\hat{\omega}'s_l'} + (\beta - \epsilon)L\overline{\hat{\omega}'q_t'}, & \hat{p}_{cb} < \hat{p} < \hat{p}_i. \end{cases} \tag{2.10}$$

Here, $\hat{p}_{cb}$ is the cloud-base pressure-height and $\beta = [1 + \epsilon\gamma(\delta + 1)]/(\gamma + 1) \approx 0.5$ is a weak function of pressure and temperature (Randall, 1980). In section 2.4.3, mixed layer buoyancy flux profiles constructed by applying the data described in section 2.3 to (2.10) are discussed.

The convective velocity scale, w_*, a measure of the overturning velocity of buoyantly driven eddies, is then calculated as

$$w_* = \left[2.5 \frac{z_i}{\hat{p}_i} \int_0^{\hat{p}_i} \mathcal{B} d\hat{p} \right]^{\frac{1}{3}} \tag{2.11}$$

where z_i is the BL depth expressed in meters. Here, we have adapted the standard definition of w_* (e.g. Nicholls and Turton (1986)) to $\hat{p}$ coordinates based on the derivation of a turbulent kinetic energy equation from the same governing equations in $\hat{p}$ coordinates used to derive (2.1) and (2.2). This equation is important for the entrainment parameterizations tested in section 2.4.4.

2.3 Data

2.3.1 Mass Budget

We assume (consistent with soundings) that cloud-top always coincides with inversion base. Thus entrainment may be calculated from (2.3) by combining measurements of cloud-top height tendency, subsidence rate, and advection of cloud-top height. During the cruise, measurements of cloud-top height were obtained at 15 second resolution from a vertically pointing 35 GHz cloud radar. This data was averaged into 3-hour means with the first mean centered at 2 UTC on the 16th; $\partial\hat{p}_i/\partial t$ was then approximated using centered differencing. Estimates of subsidence rate at the buoy location were obtained from 12-35 hour forecasts (obtained at full model vertical resolution) by both the European Center for Medium Range Weather Forecasting (ECMWF) operational forecast

model (courtesy of Martin Köhler at ECMWF) and the National Center for Environmental Prediction (NCEP) medium-range forecast model (courtesy of Hua-Lu Pan at NCEP and Steve Krueger at the University of Utah). These models assimilated surface meteorological data from the WHOI buoy but not from the RHB radiosonde soundings described in the next section. McNoldy et al. (2004) showed that, at least on climatological timescales, subsidence from reanalysis-versions of these models is in good agreement with QuikSCAT data. Advection of inversion height is assumed to have a constant value of -0.49 mm s^{-1}, diagnosed as the large-scale slope of satellite-derived cloud-top height based on a climatology from Oct-Nov 2000 - a comparable season (Wood and Bretherton, 2004). We chose this estimate despite probable synoptic and diurnal variations in the advection of inversion height, noting that because its climatological mean value is an order of magnitude smaller than the other budget terms, exact diagnosis of cloud-top height advection is probably not quantitatively important to the mass budget.

2.3.2 Moisture and Liquid Static Energy Budgets

For our budgets, we compute BL-averaged q_t and s_l from the radiosonde profiles at each launch time as the mean of the profile over the layer from 50m above the surface to the base of the inversion capping the BL. The 50m lower limit was chosen to avoid errors associated with ship-deck heating. The inversion base was chosen by eye as the height at which q_t begins to drop from relatively large BL values (typically 8 g kg^{-1}) to the extremely dry values found in the overlying air (usually 2 g kg^{-1} or less, see Fig. 2.2). This measure of inversion base agrees reasonably well with the radar-derived value; the root-mean-square error between the two versions is 64m and the sonde-based $\hat{p}_i$ is 35m lower on average (the diurnal cycle of these two quantities is compared in Fig. 2.3). The q_t and s_l profiles are computed by combining radiosonde-derived measurements of q_v and T with estimates of q_l. A q_l profile was estimated for each 3 hour period by assuming liquid water content increases linearly from a cloud base value of zero to a cloud-top value such that $1/g \int_{\hat{p}_b}^{\hat{p}_i} q_l d\hat{p}$ matches the observed liquid water path. Liquid water path was obtained at 5 min resolution from a NOAA shipboard microwave radiometer following

Temp (K)

280.4   285.9   291.5
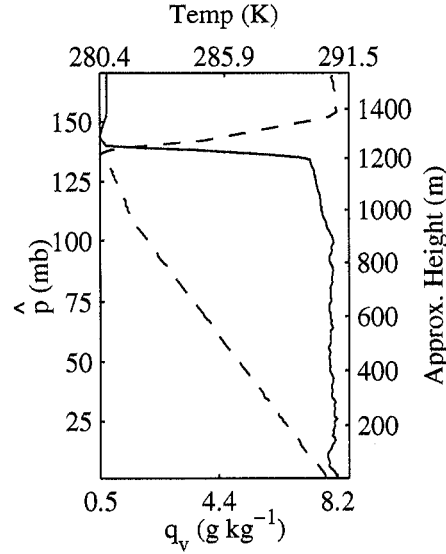
Figure 2.2: Mixing ratio (solid line) and temperature (dashed line) profiles from the radiosonde launched at 2 UTC (2000 LT) on Oct 16, 2001. The temperature inversion appears to be around 15mb ($\approx$150m) deep - five times as thick as the moisture inversion.

Hogg et al. (1983). This quantity, and all others obtained at higher-than-radiosonde resolution, was averaged into 3 hour means centered on the radiosonde launch times. One exception, however, is cloud base, which was obtained at 15 second resolution from NOAA Environmental Technology Laboratory (ETL) ceilometer. The lowest altitude return was composited into hourly median values before averaging into 3 hour means about the radiosonde launch times. This added complexity was introduced to avoid bias introduced by large outliers in the apparent cloud base that we believe was a ceilometer response to intermittent sub-cloud drizzle. Cloud fraction was taken to be the fraction of each 3 hour period that the ceilometer registered a cloud base. Density is derived from the ideal gas law. Time derivatives of $\langle q_t \rangle$ and $\langle s_l \rangle$ are computed using centered differencing. Advective terms are estimated from the ECMWF and NCEP forecasts mentioned in section 2.3.1. Results from both models are compared in section 2.4.

Surface sensible and latent heat fluxes are derived from temperature and humidity
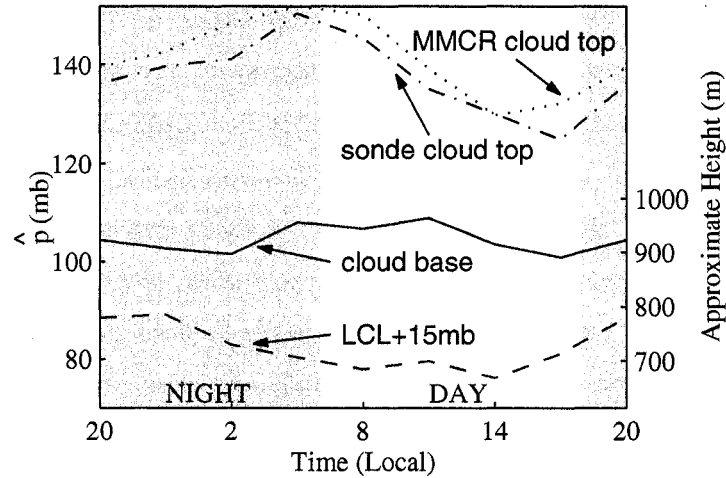
Figure 2.3: Comparison between the diurnal cycle of cloud base and that of the LCL. LCL values are shifted up 15mb to account for the effect of the surface layer. Also shown are $\hat{p}_i$ values diagnosed from radiosonde and from radar.

measurements taken on the RHB instrumented tower (14 m altitude) using the bulk flux algorithm described by Fairall et al. (1996), who estimated the error in these fluxes to be less than 5 W m^{-2}. The fluxes agreed to within this accuracy with similarly-derived fluxes from buoy measurements when the ship and buoy were collocated. Cloud base precipitation averaged over a 30 km radius centered on the ship was diagnosed from C-band radar, then expanded into below-cloud precipitation flux profiles by a sedimentation/evaporation model based on theoretical reflectivity profiles generated using ETL's millimeter-wavelength vertically pointing radar on the RHB as described in detail by Comstock et al. (2004). In cloud, a constant precipitation rate equal to the value at cloud-base is assumed. This approximation was suggested in Nicholls (1984) based on observational data showing that the increase towards cloud base in the precipitation rate for rain drops and the increase towards cloud top in the sedimentation rate for cloud droplets roughly cancel, resulting in a fairly constant precipitation flux throughout the cloud layer (since precipitation is taken in this study to be synonymous with total liquid water flux). Radiative fluxes are computed by BUGSrad, a two-stream correlated-K ra-

diative transfer scheme developed at Colorado State University (Stephens et al., 2001). Both satellite and cloud radar observations did not detect any cloud above the BL over the RHB during the six-day period. In order to obtain realistic fluxes for partly cloudy conditions, results from clear and cloudy sky radiative-transfer calculations were combined in an average which was weighted by the ceilometer-derived cloud fraction. The liquid water profile for purely cloudy conditions was taken to be the previously calculated q_l profile divided by the cloud fraction in order to account for the fact that the observed LWP was an average value of both cloudy and clear conditions. To overcome the lack of radiosonde data at higher altitudes, missing profile data below 15km were interpolated from neighboring profiles, and above 15km all profiles were blended into the McClatchey et al. (1971) standard tropical atmospheric profiles. Droplet number concentrations N_d were provided by Christopher Fairall at NOAA ETL. As discussed by Bretherton et al. (2004), this quantity was estimated during daylight hours from simultaneous measurements of cloud thickness, LWP, and cloud optical depth following Dong and Mace (2003). Nighttime values were then generated by linear interpolation. Effective radius r_e was calculated using the parameterization of Martin et al. (1994),

$$r_e = \left[\frac{3\rho q_l}{4\pi \rho_w k N_d} \right]^{\frac{1}{3}}$$
(2.12)

where $k = 0.8$ (as suggested for clean air) and ρ_w is the density of water. Droplet concentrations during EPIC ranged from 50 to 160 droplets per cubic centimeter, resulting in cloud-top effective radii of 8 to 18 μm.

Comparison between calculated and observed downwelling radiative fluxes at the surface are presented in Fig. 2.4. The left-hand plot shows that the computed SW flux matches the observations quite well on average. This is an improvement from the results presented in Caldwell et al. (2005). Better agreement in this case is due to corrected LWP measurements (Zuidema et al., 2005) in the time since Caldwell et al. (2005) went to press. Triangular markers denote times when the ship and buoy were collocated, so serve as a strict measure of instrument calibration uncertainty. Circular markers indicate times when the ship was away from the buoy (typically by less than 20km) and thus
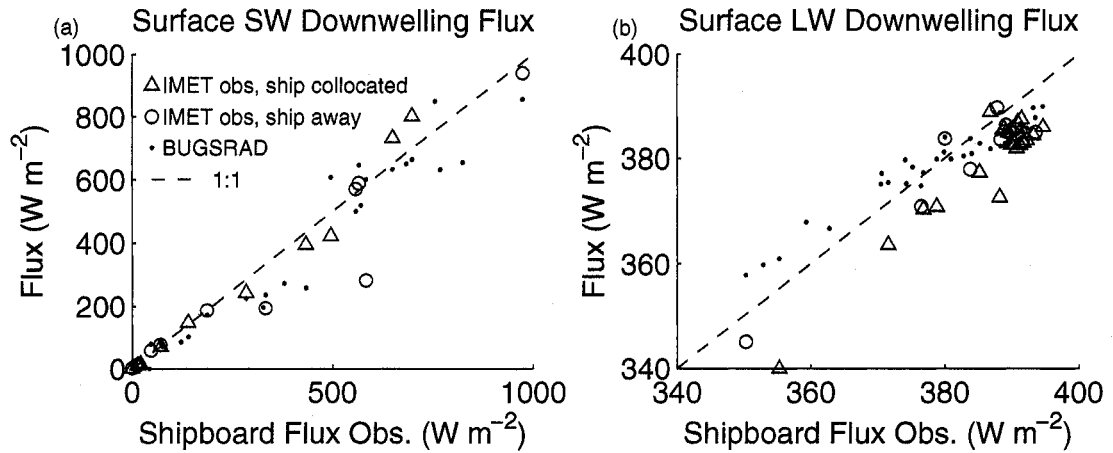
Figure 2.4: Comparison of observed downwelling flux at the surface with values calculated using the BUGSrad scheme. Coincident observations from the IMET buoy are included where available. Observations made when the RHB is located at the buoy are indicated by triangles. Values when the RHB is located near but not at the buoy are also included as circles.

show the effect of mesoscale variability on radiative fluxes. Since our radiative profiles are derived from a single sounding while the shipboard radiometer data is averaged over 3 hrs, it is unsurprising that the disagreement between the derived fluxes and the shipboard observations is of similar magnitude to that shown by the circular markers. Although the differences between ship observations and radiative transfer calculations are sometimes quite large, it is important to remember that our budgets depend only on the flux actually absorbed in the BL. Because the BL absorbs only a small fraction of the impinging solar radiation, errors in the BL net shortwave flux divergence can be expected to be much less than errors in the surface downwelling solar radiation. Calculated longwave fluxes (right-hand panel of Fig. 2.4) also agree quite well with the observations, with perhaps a 5 W m^{-2} high bias for lower fluxes (e.g. decreased cloudiness).

2.3.3 Cross-Inversion Jumps

A practical complication of imposing a mixed layer idealization on any real BL is how to optimally determine inversion jumps. An issue during EPIC was apparent systematic
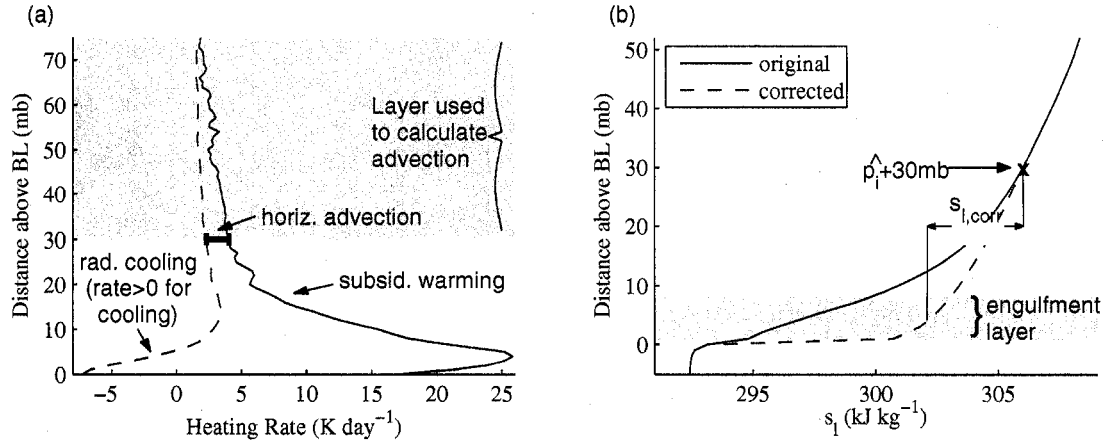
Figure 2.5: (a) Heating rate due to subsidence warming (solid lines, positive numbers indicate warming) and radiative cooling (dashed lines, positive numbers correspond to cooling). The layer used to calculate advection is indicated in the upper right-hand corner. In this region, the difference between subsidence warming and radiative cooling is interpreted as the advective tendency. A linear fit to this difference is used to diagnose advection in the region between this layer and cloud-top. (b) The uncorrected (solid) and corrected (dashed) s_l profiles along with a diagrammatic description of the engulfment layer.

errors in radiosonde-derived temperature profiles just above the inversion. Fig. 2.2 compares the q_v and T soundings from a typical radiosonde launch, 2 UTC on Oct 16. In this figure, the inversion thickness diagnosed from the q_v sounding is around 3mb ($\sim$30m) - a value consistent with the literature (Caughey et al., 1982; Lenschow et al., 2000). The T sounding, on the other hand, includes a 15mb ($\sim$150m) layer where T increases with height, rather than a jump-like inversion. The reason for this thick temperature inversion is still unclear. One possibility we have investigated is that the broad temperature inversion is a real response to enhanced radiative cooling in the air just above cloud top. This conclusion is inconsistent, however, with the radiative cooling profile in Fig. 2.5a, which shows that the region just above cloudtop is so cold that radiative transfer should be warming this region. Error due to temperature-sensor lag was also considered, but could not explain the nearly linear increase in temperature over such a deep layer. One possibility that we couldn't discredit is that cloud droplets wet the

sensor as it passes through cloud, and subsequently interfere with sensor response above cloud through evaporative cooling. Radiosonde inaccuracy in stratocumulus inversions have not, to our knowledge, been documented in other studies, a fact which is perhaps unsurprising because radiosondes have not previously been used to scrutinize the precise vertical structure above cloud in the presence of such strong inversions. Comparison of radiosonde data with simultaneous aircraft/dropsonde measurements, use of tethered balloons, or performance of laboratory experiments quantifying the effect of wetting on radiosonde temperature sensors would be useful for investigating the cause of this problem.

To avoid using temperature measurements in this uncertain region to compute cross-inversion jumps, we infer s_l at the top of the BL from its value some distance above. In order to account for the radiative cooling taking place as air subsides from the height where it is measured to the height at which it is entrained, a correction offset is applied. Ideally, this offset would depend on the time-varying entrainment rate and the above-inversion moisture profile, among other quantities difficult to assess from the available data. After discovering that more sophisticated approaches all occasionally predicted unreasonably large corrections due to this uncertainty, we applied a single correction to all soundings. This correction is derived by considering the evolution of s_l in the layer above the inversion base. Because this layer is defined relative to $\hat{p}_i$, switching to a cloud-top-relative coordinate system (with vertical coordinate $\zeta = \hat{p} - \hat{p}_i$) simplifies the analysis. In this context,

$$\frac{\partial s_l}{\partial t} + \mathbf{v} \cdot \nabla_h s_l - \hat{\omega}_e \frac{\partial s_l}{\partial \zeta} = -g \frac{\partial F_R}{\partial \zeta} \qquad (2.13)$$

where the horizontal gradient is taken here along a surface of constant ζ. Note that air above the BL is moving towards $\hat{p}_i$ at a rate $\hat{\omega}_s - (\partial \hat{p}_i / \partial t + \mathbf{v} \cdot \nabla_h \hat{p}_i)$ which, taking $\hat{\omega}_s$ to be constant over the depth of the shallow correction region and applying (2.3), is equal to $-\hat{\omega}_e$.

Averaged over the 6 day period, the soundings imply that $\partial s_l / \partial t$ is negligible. Thus (2.13) reduces to a balance between horizontal advection, subsidence warming and radia-

tive cooling. Corrections to the 6-day mean s_l profile just above the cloud top were made by forcing the s_l profile in the lowest 30mb above the inversion to obey this balance by running (2.13) to equilibrium holding all other thermodynamic quantities fixed and using upstream differencing to resolve the sharp gradient at cloud top. In this calculation, radiative fluxes were derived using the BUGSrad scheme and a zenith angle of 71°(chosen to yield the correct daily-mean insolation for Oct 16 at 20°S) was applied. Thermodynamic profiles were computed by rescaling the individual profiles at each time to have $\hat{p}_i$ equal to the mean inversion height over all soundings, then temporally averaging to create 6-day mean profiles with a sharp inversion. An $\hat{\omega}_e$ value of 3.5 mm s^{-1} was used for this calculation. This value is derived in section 2.4.1 using the mass budget (2.3) with ECMWF subsidence, which we show in 2.4.2 to be consistent with similar measures from the 6-day mean BL s_l and q_t budgets. We diagnose the vertical profile of advection in the correction region by extrapolating trusted advection values from above the correction region downward. These trusted $\mathbf{v} \cdot \nabla_h s_l$ values are diagnosed as the residual of (2.13) with $\partial s_l / \partial t = 0$. This residual, presented in Fig. 2.5a as the difference between subsidence warming and radiative cooling, appears to decrease linearly with height above about $\hat{p}_i$+30mb. Based on this observation, we approximate horizontal advection by a linear least-squares fit to the subsidence warming/radiative cooling residual in the region topping the inversion by 30 to 75 mb. This process results in a horizontal advection tendency given by

$$\mathbf{v} \cdot \nabla_h s_l = 8.5 \times 10^{-2} - 3.78 \times 10^{-4}\hat{p}. \tag{2.14}$$

Just above the inversion, this method suggests an s_l advection of 2.8 kJ kg^{-1} day^{-1}. Because this measure of advection ceases to match the predictions of Fig. 2.5a below $\hat{p}_i$+30mb, we choose our correction layer to extend from the inversion base to this level. The depth of this layer also happens to be the distance a typical air parcel will subside in a day, so correcting over this depth has the added advantage that it facilitates using an entrainment rate which has been averaged over the diurnal cycle and is therefore more robust.

By substituting the advection derived from (2.14) into (2.13) and running (2.13) to

equilibrium using upstream differencing, a corrected s_l profile may be generated. This profile is presented in Fig. 2.5b. Comparison of the original and corrected s_l profiles serves as a further illustration of how out of balance the uncorrected profiles were. Also indicated in this graphic is the engulfment layer - the region from which air is typically entrained. The depth of this layer is a rather uncertain quantity; we take the engulfment layer depth to be 8 mb based on recent analysis from aircraft flights in the Californian stratus region by Faloona et al. (2005) and estimate the liquid static energy of entrained air to be the mean value of the corrected s_l profile over this layer. Application of this definition to Fig. 2.5b implies that if we want to estimate s_l in the entrainment layer based on its value 30mb above, we must apply a correction $s_{l,\text{corr}}$ of -4.0 kJ kg^{-1} to $s_l|_{\hat{p}_i+30mb}$. Conceptually, this correction amounts to the radiative cooling occurring as air descends to the BL from 30mb above. In the absence of a reliable time-varying correction, we simply assume that $\Delta s_l = \left(s_l|_{\hat{p}_i+30mb} - 4.0 \text{kJkg}^{-1} - \langle s_l \rangle\right)$ for each sounding.

One of our main motivations for examining the s_l budget is to derive entrainment rates from (2.2). In fact, it was examination of uncorrected s_l budget entrainment rates (which average an implausible 15mm s^{-1} when $\Delta s_l = s_l|_{\hat{p}_i+3mb} - \langle s_l \rangle$) that provided our first indication of temperature sounding errors. Because we use the agreement between entrainment rates derived from the various budgets as an indicator of the uncertainty in our best-guess entrainment predictions, it is important to examine the sensitivity of the s_l budget entrainment rates to an error in our correction scheme. Propagation of error through (2.2) reveals that a fractional error in $s_{l,\text{corr}}$ will induce an error $s_{l,\text{corr}}/\Delta s_l \approx 0.4$ times as large in $\hat{\omega}_e$. Since $s_{l,\text{corr}}$ is an intuitively reasonable amount of cooling to occur at the top of the BL over the course of a day, error in this quantity is probably less than 25%, resulting in an entrainment uncertainty of a magnitude comparable to other terms in the budgets. Applying similar analysis to w_*^3, it appears that errors in $s_{l,\text{corr}}$ induce errors of roughly equal size in w_*^3. Because w_* is calculated through (2.8), which is technically only valid under idealized mixed-layer conditions, uncertainty in $s_{l,\text{corr}}$ is probably not the leading source of error in this calculation either. Further, applying perturbations to $s_{l,\text{corr}}$ does not seem to have a strong impact on the performance of the
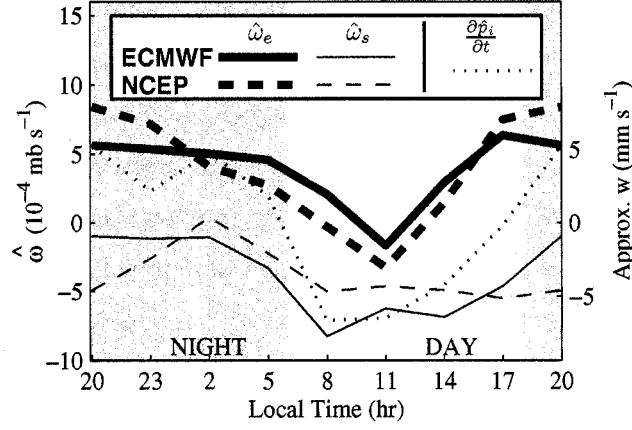
Figure 2.6: Diurnal cycle of entrainment as diagnosed from the BL mass budget. Entrainment rates are denoted by thick lines, subsidence rates by thin lines, and sonde-derived BL height tendency by dots. ECMWF values are presented in unbroken lines, while NCEP values are dashed.

entrainment parameterizations considered in section 2.4.4.

In an effort to avoid problems associated with variations in inversion depth, above-inversion total water mixing ratio is sampled at 10mb above the BL. Because q_t varies little with height just above the BL (see Fig. 2.2, for example), this value is used in Δq_t without adjustment.

2.4 Results

2.4.1 Entrainment from the Mass Budget

Fig. 2.6 presents the diurnal cycles of $\hat{\omega}_s$, $\partial \hat{p}_i / \partial t$, and $\hat{\omega}_e$ (calculated as a budget residual of (2.3) using $\hat{\omega}_s$, $\partial \hat{p}_i / \partial t$, and the assumed horizontal advective inversion-height tendency). Both ECMWF and NCEP analyses of $\hat{\omega}_s$ suggest a large diurnal cycle of subsidence, peaking around midday and damping to zero around midnight, although the NCEP analyses are noisier and have a larger semi-diurnal component. The large amplitude of this cycle is associated with a gravity wave driven by daytime heating on the Andean slopes 1500 km away (Garreaud and Muñoz, 2004). This causes a rapid increase

in BL thickness at night ($\partial \hat{p}_i / \partial t > 0$) and decrease in BL thickness during the day ($\partial \hat{p}_i / \partial t < 0$). With either analysis, the diurnal cycle of $\hat{\omega}_e$ is qualitatively in accord with expectation for radiatively driven stratocumulus. The implied entrainment rate is large at night ($\hat{\omega}_e = 5 \times 10^{-4}$ mb s^{-1}, or approximately 5 mm s^{-1}) and drops to zero near local noon when cloud heating due to solar absorption could be expected to be largest and most effective at suppressing in-cloud turbulence. The ECMWF results are more believable, since NCEP analysis implies significantly negative midday entrainment, which is physically implausible. Additionally, the ECMWF-implied $\hat{\omega}_e$ is quasi-steady throughout the night, which matches expectations since longwave radiative forcing is essentially steady and large during this time. Nonetheless, the discrepancy between ECMWF and NCEP subsidence rates can be taken as a measure of the uncertainty in this quantity. The average entrainment rates for the 6 days of study are 3.5 mm s^{-1} and 3.2 mm s^{-1} based on the ECMWF and NCEP analyses, respectively. Estimating $\hat{p}_i$ from the moisture inversion (as done for the q_t and s_l budgets) results in entrainment rates just 0.1mm s^{-1} higher in the mean and negligibly different in the diurnal cycle, which suggests that variation in $\partial \hat{p}_i / \partial t$ are not a large source of error in this study. The 6-day mean entrainment rates calculated from the mass budget compare well with the climatological value of just over 3 mm s^{-1} value obtained by Wood and Bretherton (2004).

2.4.2 Analysis of the q_t and s_l Budgets

Six-Day Mean

Each term in the mixed-layer moisture and energy budgets (2.1) and (2.2) was estimated at each radiosonde launch time using the data described in section 2.3. The resulting time series were averaged into 6-day means, which are presented in Tables 2.1 and 2.2. All terms are given in energy flux units for consistency. The entrainment rates are inferred from the mass budgets. In both budgets there are balances between dominant terms. Table 2.1 reveals that surface evaporation is balanced primarily by entrainment drying and secondarily by horizontal dry advection. The s_l budget, on the other hand, indicates that longwave cooling and (to a lesser extent) cold advection balance comparable

contributions from entrainment, shortwave warming, and sensible heating. Precipitation does not play a significant role in either budget. Although significant cloud base drizzle was observed on several of the study days, a high cloud base (ranging from 800 to 1100 m) meant that almost all precipitation evaporated before reaching the surface (Bretherton et al., 2004; Comstock et al., 2004). Wood (2005) suggests that the EPIC case is not unusual in this regard and that in general, drizzle tends to largely evaporate before reaching the surface below stratocumulus clouds with bases higher than 500m.

In each table, an estimate of the sampling uncertainty for the 6-day mean is given as

$$\sigma_{\text{mean}} = \sqrt{\frac{1}{48}\left[\frac{1}{8}\sum_{k=1}^{8}\sigma_k^2\right]} \qquad (2.15)$$

where σ_k is the standard deviation of the data at the kth time of day. In using this measure, we assume that error is independent of time of day, so our best guess as to the the standard deviation at any point in the data set is $\frac{1}{8}\sum_{k=1}^{8}\sigma_k^2$. Under these assumptions, (2.15) is the standard deviation in the 6-day mean. It is important to realize that this error statistic reflects only sampling variability and does not capture biases due to calibration error or to uncertainties in the analysis methods. Additionally, much of σ_k could be due to real synoptic variability rather than an inability to accurately sample quantities at individual times. In this case σ_{mean} may have little to do with the accuracy of a budget term, instead reflecting its representativeness as a longer-term mean to the extent this can be assessed from only 6 days of data. From this perspective, however, σ_k is only a lower bound, since synoptic variations are autocorrelated over periods of several days. In spite of these caveats, we will interpret σ_{mean} for individual budget terms as a rough guide to the representativeness of the balances in our 6-day mean. Taken in this context, the tendencies of both q_t and s_l in the 6-day mean are not significantly different than zero, which is encouraging since time invariance suggests that the averages captured here are representative of a longer-term mean rather than of only our particular 6 days of data. Another indication of useful budgets is that the sampling variability of all remaining budget terms are reassuringly small compared to the magnitude of their mean values.

A second, more robust measure of the uncertainty inherent in the budget calculations is available in the form of 6-day mean budget residuals. It is in assessing these residuals that our error analysis is most compelling, because this error really does reflect sampling inadequacy or biases. These residuals are presented in the last columns of Tables 2.1 and 2.2. That the budgets generally don't close to within the calculated uncertainties illustrates that sampling error analysis tends to underpredict the actual error in this type of study and that biases may exist in some of the estimated budget terms.

We saw in Fig. 2.6 that estimation of the time-series of subsidence at a remote ocean location from model analyses may be subject to large systematic errors which may depend on the diurnal cycle. These errors may affect the mass-budget estimate of entrainment. Hence, another perspective on the heat and moisture budgets is as a way to get independent estimates of $\hat{\omega}_e$ by solving for the entrainment fluxes as budget residuals in (2.1) and (2.2). Applied in this way, the q_t budget yields a 6-day mean entrainment rate of 4.3 mm s^{-1} , while the s_l budget yields 4.7 mm s^{-1} . Comparison of the three independent entrainment estimates for this period suggests a mean entrainment rate for the buoy period of roughly 4 ± 1 mm s^{-1}.

Diurnal Cycle

Only a few terms in the q_t and s_l budgets have diurnal cycles of significant amplitude. These terms are plotted in Fig. 2.7 (with entrainment fluxes based on $\hat{\omega}_e$ from the ECMWF mass budget and signs chosen so that a positive perturbation increases q_t or s_l). In the moisture budget, decreased entrainment drying during the day results in a buildup of BL moisture, which is then depleted by more vigorous entrainment at night. The diurnal cycle of liquid static energy involves an increase in $\langle s_l \rangle$ during the day due to solar heating, followed by a decrease after sunset which is partially mitigated by enhanced entrainment of warm air from the free troposphere at night.

An estimate of the sampling variability involved in these calculations is made following (2.15). Day-to-day variability in storage (= $\hat{p}_i \partial / \partial t$ - the rate at which a quantity accumulates in the BL) and entrainment warming/drying are assumed to be independent
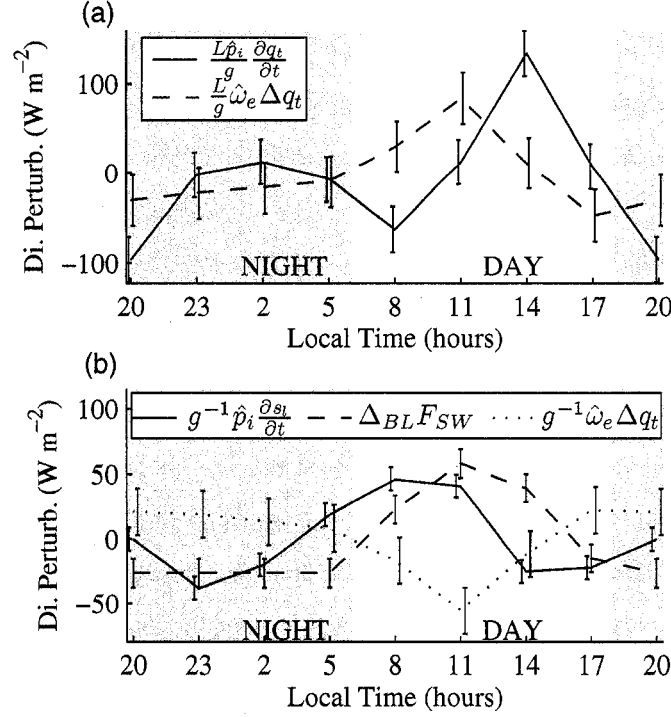
Figure 2.7: Diurnal cycle for budget terms with large diurnal amplitude (omitted terms have diurnal cycles of 10W m^{-2} or less). For ease of comparison, means have been removed from each term and the sign convention is such that a positive perturbation increases q_t or s_l. Errorbars represent standard deviations in the mean for each time of day (as described in the text).

of time of day, so the error in these quantities should be $\sigma_{di} = \sqrt{8}\sigma_{mean}$ since there are eight times fewer samples for each time of day than for the mean. Shortwave heating - important in the s_l budget - has zero variability at night, rendering (2.15) inappropriate. Instead, the error bars given on $\Delta_{BL}F_{SW}$ during the daytime are taken as the standard deviation of the data at that time of day.

By deriving entrainment fluxes for each time of day as residuals of (2.1) and (2.2), we are able to infer time series of entrainment, which are shown in Fig. 2.8 with error bounds again calculated as $\sqrt{8}\sigma_{mean}$. The estimates are broadly consistent with the subsidence-based entrainment prediction, with a nocturnal maximum of approximately 5 mm s^{-1} and
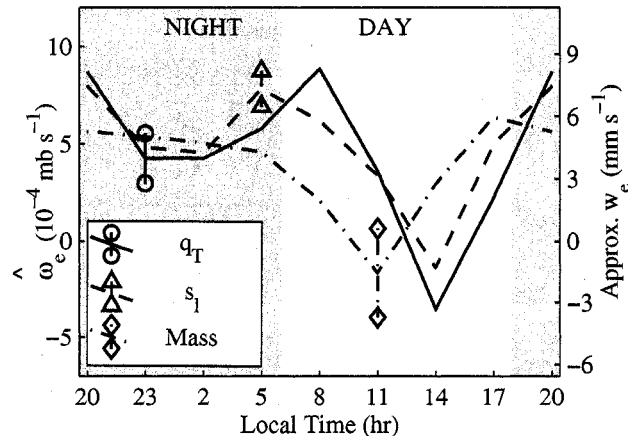
Figure 2.8: Comparison of the diurnal cycle of entrainment as calculated from the q_t budget (solid lines, circular endpoints on error bar), from the s_l budget (dashed lines, triangular endpoint), and from the subsidence method (dot-dashed lines, diamond end-point). Error bars represent one standard deviation limits on the mean associated with sample variability over the 6 days. Only one errorbar is presented for each method because the error is assumed identical for each time of day.

a sharp drop toward midday. Both estimates predict the $\hat{\omega}_e$ minimum to occur later than suggested by the mass budget. Again, the error bounds provide only a rough measure of sample variability, although evidence of systematic bias is present as well. For example, the q_t budget suggests negative entrainment around midday, which is clearly unphysical. Additionally, confidence bounds in Fig. 2.8 are disjoint for some methods at some times of day. Comparing Fig. 2.8 to Fig. 2.7, we see that our estimates of the diurnal cycle of entrainment from the q_t and s_l budgets are largely modulated by the diagnosed diurnal cycle of storage, which is one of the more uncertain measurements in the budgets because it is based on a single radiosonde profile every three hours. Nonetheless, all 3 budgets yield a similar diurnal profile and mean value of w_e, which increases our confidence in the entrainment estimates from the individual budgets. For the remainder of this Chapter, ECMWF mass-budget entrainment rates will be used wherever entrainment observations are required.
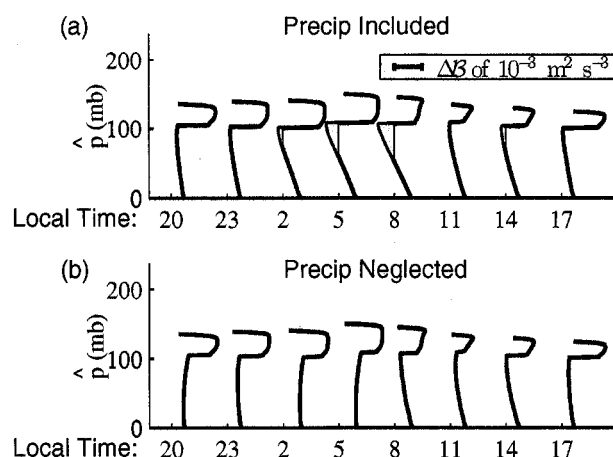
Figure 2.9: Diurnally-composited buoyancy flux profiles (a) including and (b) excluding the precipitation flux contribution. The tick mark above each time indicates the line of zero-B for that time; regions of negative buoyancy flux are shaded. A sense of the magnitude of B may be obtained from the scale in the upper-left corner of (a).

2.4.3 Diurnal Cycle of Turbulence

Using the method described in section 2.2.2, buoyancy flux profiles were calculated for each three-hour interval. Where possible, the data used in this calculation are presented in Table 2.3. Because calculation of the turbulent fluxes depends strongly on the mixed-layer assumption, we emphasize that when the BL is not well-mixed our method of inferring buoyancy flux becomes inappropriate.

Fig. 2.9a shows the 6-day mean diurnal cycle of mixed-layer inferred buoyancy flux. At all times of day, the profiles have the structure expected of a radiatively-driven cloud-topped mixed layer - small values near the surface decreasing to a minimum at cloud base, then jumping up to reach a maximum value in the cloud. Also apparent is a diurnal cycle in the intensity of buoyancy flux within the cloud. The night-time maximum is the result of strong longwave cooling at cloud top and the daytime minimum is the result of this cooling being canceled by shortwave heating. A related feature is the diurnal variation in the sub-cloud buoyancy flux minimum. Fig. 2.9a shows substantial negative B building up below the cloud before sunrise and persisting throughout the morning. The existence of

negative buoyancy fluxes during the day is an expected consequence of shortwave heating in the cloud. However, sub-cloud buoyancy flux becomes negative before dawn and reaches a minimum before 8 am, earlier than expected for a BL dominated by shortwave heating.

Fig. 2.9b suggests that the process responsible for these features is the evaporation of drizzle. This graphic shows the results of a sensitivity study in which the buoyancy flux has been recalculated with F_p set to zero. While changing the drizzle rate should, in reality, affect cloud thickness, BL depth, and other aspects of BL structure which would themselves affect the buoyancy flux profiles, this figure is useful as an illustration that drizzle is important to BL structure. In this graphic, we see that without drizzle the time of minimum buoyancy flux is around noon and that cloud-base buoyancy fluxes never become negative. Because significant negative B leads to BL decoupling (Bretherton and Wyant, 1997; Stevens, 2000), this suggests that drizzle may be contributing to partial early-morning BL decoupling. This hypothesis may be investigated by examining the ability of the lifting condensation level (LCL) derived from shipboard measurements to predict cloud base over the course of a day. In a well-mixed BL, surface and cloud base humidity are homogenized by mixing, so the surface LCL will be a good predictor of the actual cloud base. In practice a correction must be applied to the surface LCL to account for the moisture and temperature gradients within the surface layer. By comparing the average surface LCL to that computed from the sondes at 100m above the surface, we calculate the surface layer to cause an approximately -15mb bias to the surface LCL. This is consistent with the correction one would make using the observed air-sea moisture differences and assuming a log-layer between the 15m measurement height and 100m. Fig. 2.3 compares the 6-day mean diurnal cycle of surface LCL (shifted up 15mb) and the ceilometer-measured cloud base. This figure shows that the BL is more well-mixed during the night (though even then there is a slight residual moisture stratification), but rapidly becomes less so in the early morning and remains less well mixed throughout the daylight hours. This phasing corresponds closely to the onset of negative buoyancy flux presented in Fig. 2.9, corroborating the role of early-morning drizzle and later solar

Table 2.3: Quantities useful for the calculation of B or for testing parameterizations. Entrainment rates are taken from the ECMWF mass budget, which predict the entrainment value denoted by 0* to be less than zero; a value of zero is assumed for this study.

time Local hr	$\hat{p}_b$ mb	$\hat{p}_i$ mb	$q_l\|_{\hat{p}_i}$ g kg⁻¹	Δq_t g kg⁻¹	Δs_l kJ kg⁻¹	$\hat{\omega}_e$ Pa s⁻¹	$F_p(0)$ kg m⁻² s⁻¹	$F_p(\hat{p}_b)$ kg m⁻² s⁻¹	$\Delta_{BL}F_R$ W m⁻²	SHF W m⁻²	LHF W m⁻²	w_* m s⁻¹
2	102	141	0.71	-6.81	10.77	5.0e-02	-4.5e-06	-1.4e-05	79	17	108	1.19
5	108	151	0.71	-6.68	10.55	4.6e-02	-5.0e-06	-1.9e-05	78	17	105	1.12
8	107	146	0.61	-6.07	10.90	2.1e-02	-2.7e-06	-1.2e-05	29	17	102	0.88
11	109	135	0.48	-6.33	10.34	0*	-7.0e-07	-3.5e-06	-8	15	97	0.91
14	104	130	0.42	-6.86	9.72	2.9e-02	-2.8e-07	-2.3e-06	11	13	87	0.90
17	101	125	0.66	-6.61	9.27	6.4e-02	-4.5e-07	-3.3e-06	66	11	92	1.07
20	104	136	0.52	-6.70	10.59	5.6e-02	-1.4e-06	-5.8e-06	79	11	97	1.20
23	103	140	0.73	-6.52	10.93	5.4e-02	-1.2e-06	-4.7e-06	80	12	102	1.18
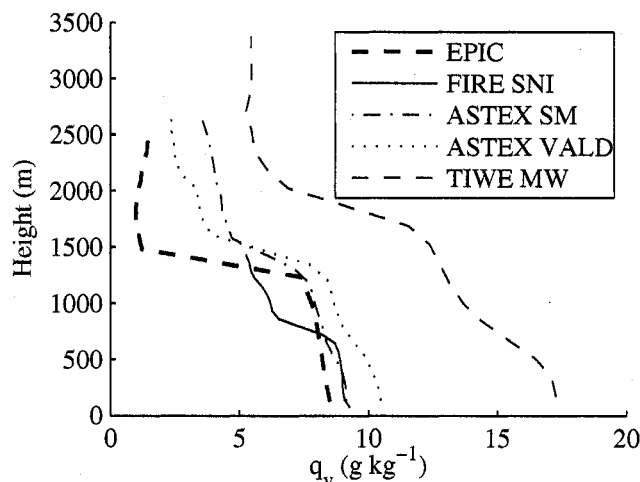
Figure 2.10: Comparison of EPIC composite q_v profile with similar profiles from San Nicholas Island (33°N, 119°W), Santa Maria Island (37°N 25°W), the R/V Valdivia (28°N, 24°W), and the R/V Moana Wave (0°, 140°). With the exception of EPIC, these data sets are described in Albrecht et al. (1995b).

absorption in inhibiting efficient vertical mixing of the BL. Fig. 2.9b is also worthwhile as a consistency check on our drizzle fluxes since this graphic shows that a BL with negligibly small drizzle rates would be better mixed than we observe, and thus that the true drizzle rate can't be too much lower than our estimates.

The stratification apparent in Fig. 2.3 is not entirely surprising. Previous studies (Albrecht et al., 1995b; Klein et al., 1995; Coakley et al., 2000; Wood and Bretherton, 2004) support the notion that deeper BLs tend to be more decoupled. This feature is illustrated in Fig. 2.10, which compares q_v profiles from various campaigns. In this graphic, deeper inversions tend to be associated with stronger BL moisture gradients. The Atlantic Stratocumulus Experiment (ASTEX) profiles are interesting because they have have roughly the same BL depth as EPIC, but show much *more* decoupling, with a scud-capped surface moist layer detraining into thin, patchy stratocumulus near the BL top (Albrecht et al., 1995a). Better mixing in the EPIC region may be related to the presence of a stronger inversion or drier free troposphere (allowing more cloudtop cooling)

in this area, although this relationship is the subject of ongoing investigation. The fact that no scud was observed during the 6 days of study, and that BL gradients in θ and q_t were found to be quite weak (as discussed in section 1.6) indicate that even during the day, mixing was sufficient to justify use of the mixed-layer assumption in calculating buoyancy flux profiles.

2.4.4 Entrainment Parameterization

Conceptually, entrainment results when large eddies penetrate the inversion capping the BL, lose momentum, and fall back through the inversion, drawing filaments of free-tropospheric air back down with them (Turner, 1973). As such, many entrainment parameterizations have tended to focus on quantifying the strength of these eddies and the efficiency with which they entrain the overlying air. In a cloud-free convectively driven BL the relation

$$\frac{w_e}{w_*} = A \mathrm{Ri}^{-1} \tag{2.16}$$

was found to hold well with w_* as defined in (2.11), bulk Richardson number $\mathrm{Ri} = \frac{\Delta b z_i}{w_*^2}$ (where the inversion density jump Δb is expressed in buoyancy units) and empirically-derived entrainment efficiency rate $A \approx 0.2$ (Driedonks, 1982; Deardorff, 1983). In the presence of cloud, however, (2.16) ceases to fit the data as written. In this regime, values of A between 1 and 5 have been inferred from aircraft observations (mostly during daytime), with considerable spread between experiments (Nicholls and Turton, 1986; de Roode and Duynkerke, 1997; Faloona et al., 2005). Such inferences are complicated by the possibility of decoupling, which could result in the appropriate vertical eddy scale being smaller than z_i and thus overpredicting A (since overpredicting z_i would cause an overprediction of Ri, resulting in an overestimation of A in (2.16)). The composite diurnal cycle of w_e and w_* inferred from the EPIC data is consistent with this hypothesis. Fig. 2.11 compares the relation between w_e and $w_* \mathrm{Ri}^{-1}$ for the 8 samples of the EPIC diurnal cycle with measurements from previous campaigns. The EPIC data supports an A value of 1.1, which is in line with the recent DYCOMS II findings but smaller than suggested by other, earlier experiments. The spread between experiments underscores
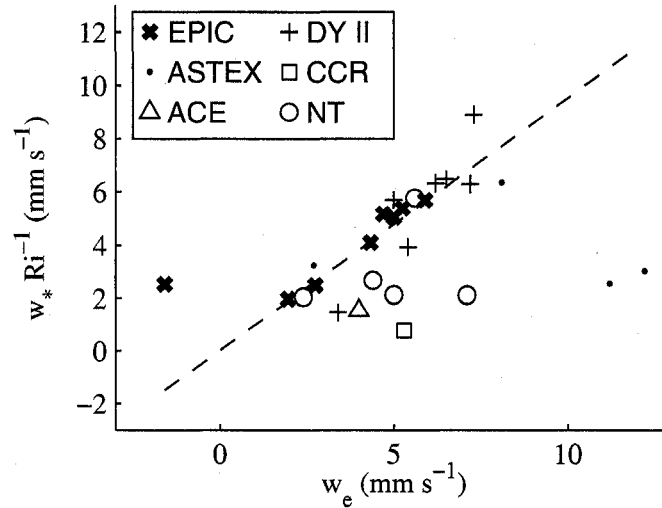
Figure 2.11: Comparison of entrainment efficiency from various campaigns. The dashed line is the best fit to the EPIC data (constrained to pass through the origin). The reciprocal of this slope is the best fit estimate of A. In this diagram, DY II (Faloona et al., 2005) involves DMS w_e from their Fig. 5 along with w_* and Ri from their Fig. 7. ASTEX uses w_* and Ri from Table 2 (flights 1-4 only) of de Roode and Duynkerke (1997) and w_e estimated from Fig. 12 the same paper. CCR (Caughey et al., 1982) involves w_* and Ri (derived from their eq. 7) from this paper and w_e from Roach et al. (1982). Aerosol Characterization Experiment (ACE) data are from Boers et al. (1997), which lists w_* and w_e, but yields Ri only after considerable estimation (using their Fig. 5, 6). NT refers to Nicholls and Turton (1986) and is directly from their Table 1. Note that NT uses Ri with z_i replaced by a (smaller) mixed layer depth.

the considerable uncertainty involved in this calculation. Also, the 'x' corresponding to 11am local time does not fall on the best-fit line because the entrainment inferred for this time is negative - an unphysical prediction. Further, entrainment from the mass budget is used both as the independent variable and in the w_* calculation, which could bias the results. Sensitivity calculations indicate that our estimated uncertainty in entrainment (about 25%) results in an uncertainty in A of around 50%. Finally, the mixed-layer approximation is employed here for all times of day in calculating w_*, even though Fig. 2.3 suggests that the well-mixed assumption is not perfectly satisfied during daylight hours.

Measurement uncertainty alone, however, is unlikely to account for the wide spread in A reported in the literature. There is no reason A should be a universal constant in cloud-topped mixed layers. Clouds affect turbulence (and thus, perhaps, entrainment) in a multitude of ways which could depend on environmental conditions in a manner not captured by (2.16) with A held constant. Choosing which of these processes are important and finding a way to include these processes in a parameterization is at the heart of the current entrainment debate.

We now compare our observations with the predictions of a few recent parameterizations, each of which emphasizes a different cloud process for diagnosing entrainment. The first of these schemes was proposed by Turton and Nicholls (1987). This scheme, hereafter denoted TN, accounts for the enhancement of turbulence by evaporative cooling at cloud top by replacing Δb in (2.16) with

$$\Delta b_{TN} = \frac{\Delta b}{1 + a_2 \left(1 - \frac{\Delta m}{\Delta b}\right)}$$

where $\Delta m = 2 \int_0^1 \Delta b(\chi) \, d\chi$. Here, $\Delta b(\chi)$ is the cloud-top buoyancy jump (including evaporative cooling) caused by mixing χ parts inversion-top air with $1 - \chi$ parts cloudy air so that Δm is proportional to the average evaporative buoyancy enhancement over all possible mixtures. Turton and Nicholls found $a_2 = 60$ to fit their data well, although a recent regional model simulation of subtropical stratocumulus suggests that $a_2 = 15$ provides better results when this scheme is implemented within a BL-turbulence parameterization. (McCaa and Bretherton, 2004). Entrainment predictions using both values are considered here. A value for A of 0.2 is assumed for this scheme.

The second parameterization comes from Lilly (2002a). This proposal (hereafter DL) also accounts for cloud-top evaporation, this time by replacing Δb in (2.16) with $\Delta b_{DL} = \alpha \Delta_{\text{sat}} b + (1 - \alpha) \Delta_b$ where $\Delta_{\text{sat}} b$ is the buoyancy jump across cloud top assuming the above-cloud top air is saturated. This correction was designed to fit Lilly's observation that cloud-top dynamics seem to be a combination of the values predicted independently for saturated and dry microphysics. The optimal combination of the two cases was chosen

empirically to be $\alpha = \tanh(2.45m_*)/\tanh(2.45)$ where m_* is the mixing fraction sufficient to just evaporate the cloud. The other interesting feature of the DL scheme is that turbulence generated at cloud top is weighted more heavily than that generated at the surface by replacing w_* in (2.16) with $w_{*,DL} = \left[3\int_0^{z_i} \frac{z}{z_i}\mathcal{B}dz\right]^{1/3}$. For this scheme, we adopt the suggested A of 3.0.

Finally, we consider the parameterization in Lewellen and Lewellen (1998) (hereafter LL), which is based on a rather different hypothesis - that entrainment is controlled by large-eddy energetics. LL assume that a fixed fraction of the TKE generated in the absence of entrainment is depleted through entrainment mixing of buoyant air from the inversion down into the BL. Assuming once again that buoyancy flux is the main source of TKE, the LL parameterization may be written

$$\eta = \int_0^{z_i} \left[\mathcal{B}_{NE} - \mathcal{B}\right] dz / \int_0^{z_i} \mathcal{B}_{NE} dz$$

where η is taken as .35 on the basis of large-eddy simulations and $\mathcal{B}_{NE}$ is the buoyancy flux in the absence of entrainment. They also include a correction for radiative cooling in the inversion layer which we omit on the basis that it is not clear how this value should be calculated from the EPIC data, or whether it is even physically relevant (Lilly, 2002b). Other parameterizations could be tested against our data; we selected these three because the comparison is straightforward yet the parameterizations are still fairly different.

A comparison of these parameterizations is presented in Fig. 2.12. Except for the TN parameterization with a_2=60, all of the schemes agree closely with each other and quite well with the EPIC data. The agreement between the three parameterizations is remarkable, especially since the LL closure completely neglects evaporative enhancement, which plays an essential role in the other two closures. These schemes performed similarly well in a comparison with entrainment observations from the first research flight of DYCOMS II (Stevens et al., 2003). Successful simulation of the entrainment rates from EPIC is impressive because it implies that the closures exhibit the proper sensitivity to the diurnal cycle. Like most other studies, however, our comparison involves large uncertainties. Longer-term measurements similar to those made in EPIC would be extremely useful for
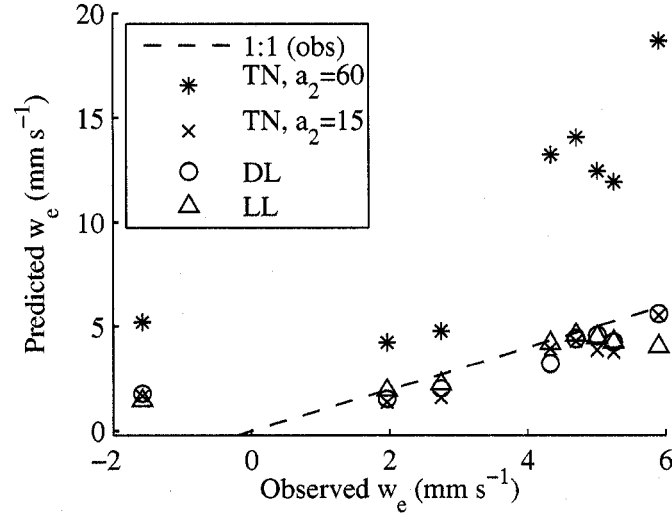
Figure 2.12: Entrainment rates predicted by the various schemes for each of the eight times of day plotted against the observed entrainment rate. The 1:1 line (dashed) depicts perfect agreement with the observations.

reducing these errors.

2.5 Conclusions

A clean diurnal cycle sampled by an extensive set of shipborne measurements during EPIC 2001 has provided an excellent opportunity to study the diurnally-varying mass, heat, and water budgets of the SE Pacific stratocumulus region and their implications for entrainment and decoupling. We have combined frequent radiosonde observations, ship-based remote sensing of cloud properties, a radiative-transfer model, and surface turbulent flux measurements with ECMWF and NCEP analyses of subsidence and horizontal advection to evaluate all terms in these budgets during a 6-day period. The mean budgets over this period showed balances expected for stratocumulus. The diurnal variation of entrainment and the associated warming and drying were balanced by diurnal variations in storage and in the absorption of insolation. Each budget provided an independent estimate of the diurnal cycle of entrainment rate as a budget residual. All three

estimates have similar daily means and a consistent diurnal cycle. This cycle consists of fairly constant entrainment rates of 5 mm s^{-1} throughout the night, dropping to near zero by midday before recovering in the evening for a daily mean value of 4 mm s^{-1}.

Buoyancy flux profiles inferred from this analysis show that drizzle, which is negligible in terms of its direct effect on the water and energy budgets (because it largely evaporates before reaching the surface), nonetheless exerts a strong influence on BL dynamics by limiting turbulent mixing below cloud base and thereby promoting decoupling. Independent evidence of partial decoupling is found in the form of increased LCL/cloud base difference from early morning to late afternoon, although even then residual mixing keeps BL internal gradients of conserved variables relatively small so a mixed layer approximation is still reasonable. The buoyancy flux profiles are used to test selected entrainment closures, which performed surprisingly well in predicting the correct diurnal cycle of entrainment. That such an internally consistent picture of entrainment into a stratocumulus-capped mixed layer could be obtained from ship-based observations alone is quite remarkable, and is a testament to the suite of ship-based measurements made during EPIC. Coordination of a similar set of measurements with an airborne field campaign could better test this approach and further advance our understanding of the interplay between entrainment, turbulence, drizzle, and the diurnal cycle in stratocumulus.

Chapter 3

LARGE EDDY SIMULATION

3.1 Introduction

As noted in previous chapters, using observational data to determine the dynamical response of the BL to changing forcings involves many challenges. One problem is that some important quantities (such as entrainment) are very difficult to measure accurately in a real-world setting. Another problem is that it is hard to isolate the effect of a single forcing because typically all forcings in the observed system are fluctuating. Further, the importance of each term cannot be determined solely by its direct budget impact because the BL state is determined by a complex web of feedbacks which are not captured by simple budgets. The effect of precipitation on buoyancy flux (discussed in Chapter 2) is a good example of this. While the direct effect of drizzle on the buoyancy flux budget is to decrease subcloud $\overline{w'b'}$ (Fig. 2.9), such analysis neglects the fact that drizzle also changes quantities such as z_i, z_b, and LWP which could themselves have an important effect on buoyancy flux. Because LES provides a means for examining individual forcing changes in a physically-consistent framework, it is an important tool for understanding the Sc-topped BL. We begin this chapter by investigating the extent to which LES is able to capture the observed BL behavior during EPIC. We then perform sensitivity studies to determine the impact of drizzle and the diurnal cycle of subsidence on the BL.

3.2 Model Formulation

The model we use for this study is the System for Atmospheric Modeling (SAM, Khairout-dinov and Randall, 2003) version 6.5. This is an anelastic model based on prognostic equations for precipitating water mixing ratio, s_l, and q_t[1]. Our version is modified to use

---

[1] In SAM, q_t is defined to be *nonprecipitating* water, though this distinction is unimportant for Sc, where precipitating water typically accounts for less than 0.1% of the total water.

the Khairoutdinov and Kogan (2000) (hereafter KK) drizzle parameterization with fixed N_d, requiring an additional prognostic equation for drizzle drop concentration. Effective radius (used for radiative transfer) is computed from N_d and LWP at each grid cell following Martin et al. (1994). Radiative fluxes are computed every 20 timesteps using the CAM3 radiation code (Collins et al., 2006) with time-varying zenith angle computed to match conditions during the EPIC cruise. A model timestep of 4 sec is imposed, though each step is broken by the model into smaller substeps as needed in order to maintain stability. Our domain is taken to be doubly periodic in the horizontal directions with a sponge layer occupying the top 30% of our domain.

Surface fluxes were computed from local windspeed and thermodynamic properties at the lowest gridpoint (2.5 m) following Monin-Obukhov theory. The Coriolis force is computed from geostrophic winds (assumed equal to EPIC radiosonde winds in the free troposphere and ramping linearly to a surface value computed as described in Appendix B). To keep surface winds (and hence surface fluxes) close to observed values, we nudge winds to the observations using a timescale which increases smoothly from 100 min near the surface to one day above the domain-mean inversion height. By nudging winds even in the free-troposphere where they are close to geostrophic, we damp inertial oscillations that may otherwise be excited as the winds change.

As noted in Chapter 1, correct entrainment rates are a prerequisite for accurate simulation of the Sc-topped BL. However, they are hard to obtain, even with a high-resolution LES. Bretherton et al. (1999) find high vertical resolution around cloud top (≤ 5 m) to be necessary in order to control overentrainment due to spurious numerical diffusion. In order to provide high resolution at cloud top while minimizing computational cost, we use a vertically-stretched grid with a minimum grid spacing of 5 m near the surface and inversion and larger grid spacing (up to 50 m) elsewhere (Fig. 3.1). To further decrease computational expense, we employ a relatively large (25 m) horizontal grid spacing. This is a reasonable tactic since studies using a variety of advection and subgrid turbulence schemes (Lewellen and Lewellen, 1998; Stevens et al., 1999) have found entrainment to be relatively insensitive to horizontal grid spacing. One study which did obtain dependence
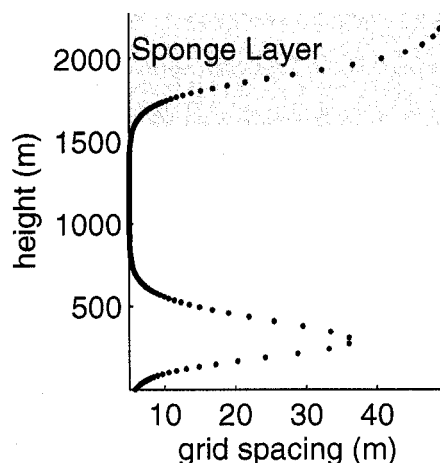
Figure 3.1: Vertical grid spacing for SAM runs. The sponge region is shaded.

on horizontal grid size (Stevens and Bretherton, 1999) found entrainment to decrease slightly with increasing horizontal resolution. If this last study is correct, increasing grid anisotropy may actually be a way to compensate for the typical LES overprediction of w_e. A sensitivity test (Section 3.4) suggests decreasing horizontal resolution does not significantly affect entrainment in SAM.

Creating an LES simulation of Sc which produces realistic entrainment also requires using a subgrid-scale (SGS) parameterization which limits mixing across the inversion (Stevens et al., 2005b). While this occurs naturally for dynamic SGS models (e.g. Germano et al., 1991), these models are complicated, computationally intensive, and involve assumptions which are hard to justify physically (Pope, 2000, p.626) and are therefore not widely used. More typical atmospheric SGS parameterizations such as that of Smagorinsky (1963) and Deardorff (1980) (both available in SAM), however, tend to produce too much mixing across z_i. Stevens et al. (2005b) found that for a nocturnal Sc simulation with the UCLA LES, simply turning off the SGS model for scalars resulted in good agreement with observations. We follow this procedure for our runs, though a sensitivity study presented in Section 3.4 suggests that this omission makes very little difference to our simulations. For momentum, we apply the Smagorinsky SGS scheme with horizontal

diffusivity scaled by $(\Delta x/\Delta z)^2$ (where Δx is the horizontal grid spacing and Δz is the vertical grid spacing) to account for the large anisotropy of our grid.

Ackerman et al. (2004) found entrainment to be significantly decreased by cloud droplet sedimentation. This is explained in Bretherton et al. (2007) as a consequence of removing liquid water in the cloud-top region, which decreases evaporative enhancement in entraining plumes and (to a lesser extent) decreases cloud-top radiative cooling. Sedimentation is included in SAM following equation 1 of Bretherton et al. (2007), which assumes cloud droplets are log-normally distributed with geometric standard deviation σ_g and fall at a rate given by Stokes' law. While observational evidence suggests σ_g should be between 1.2 and 1.5, we use this quantity as a tuning parameter to keep our model from overentraining. We find that $\sigma_g = 2.0$ provides reasonable results for 3D simulations while $\sigma_g = 1.9$ is optimal for 2D cases.

The difficulty of simulating the diurnal cycle of Sc with LES is evident from the dearth of such studies in the literature. The one study we are aware of, by Duynkerke et al. (2004), which simulated the diurnal cycle seen in the 1987 FIRE experiment off the coast of California, resorted to tuning the subsidence rate to compensate for overentrainment, resulting in simulated BLs which were too dry and warm.

An obvious challenge with a study of the diurnal cycle is that it requires relatively long model runs. In order to achieve the required spatial resolution yet keep these runs computationally feasible, either the domain size or the dimensionality must be limited. One compromise we make is to perform our sensitivity studies with 2D simulations. These simpler simulations are shown in Section 3.4 to behave quite similarly to their 3D analogues. Our runs use 128 gridpoints in the horizontal direction(s) and 272 gridpoints in the vertical, resulting in a domain size of 3.2km by 2.2 km. At this resolution, a 3D 6-day simulation on 16 nodes of our linux cluster takes about 100 hours. Each node of this cluster consists of 2 dual-core Opteron 2210 (1.8GHz) processors for a total of 64 cores per simulation.

A 3.2 km wide domain is too small to resolve multiple convective cells, so our simulation typically includes just one domain-filling cell at a time (Fig. 3.2). While one cell
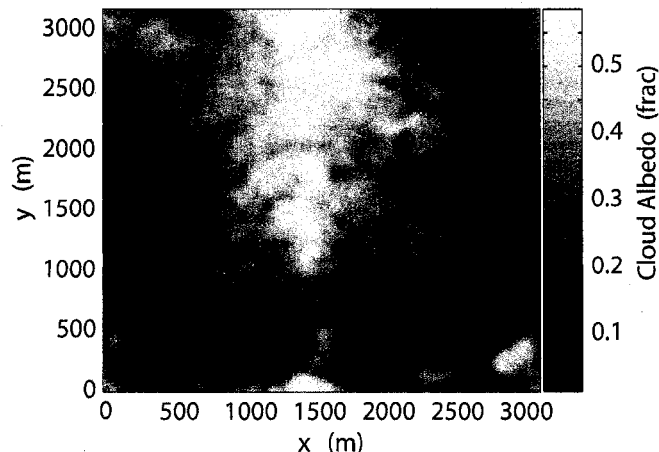
Figure 3.2: Snapshot of cloud albedo (calculated following Savic-Jovcic and Stevens (2007)) at 32 hrs into run (0400 LT).

is obviously not enough to use for statistical analysis, our simulations are long enough that temporal variations can, to some extent, make up for the lack of spatial resolution. To this effect, all model data is averaged up to 3 hr resolution for analysis unless otherwise noted. A larger question is whether our limited domain properly handles the effect of drizzle, which is thought to induce mesoscale BL organization with potentially important repercussions for domain-mean properties (e.g. Paluch and Lenschow, 1991; Stevens et al., 2005a). While this question has not been answered definitively, comparison of 6.4× 6.4 km and 12.4×12.4 km simulations in Xue et al. (2007) suggest it does (at least for this range of scales). Additionally, the 25×25 km simulations of Savic-Jovcic and Stevens (2007) show qualitatively the same drizzle response as similar simulations performed by Stevens et al. (1998) on a domain comparable to ours. In Section 3.4 we do a 2D sensitivity study which suggests that domain size has only minor effect on our results.

Another problem with long simulations is that large-scale processes typically omitted from LES become important. In particular, horizontal advection should be height-independent in the BL for well-mixed conditions, but may change discontinuously across cloud top. Since our ECMWF advective forcings are relatively uncertain and don't re-

solve the inversion very well, and because the depth of the BL changes in time and across columns, it is easier and more accurate for us to apply height-independent BL advections to the whole model domain, then to correct for this anomalous forcing by nudging free tropospheric θ_l and q_t towards the EPIC radiosonde profiles with a relatively short (3 hr) relaxation timescale. This procedure is essentially the same as that employed in de Szoeke and Bretherton (2004). Because nudging in the entrainment zone would artificially affect the entrainment process, we start nudging 75 m above the domain-averaged value of z_i (computed as the height of most negative domain-averaged $\partial q_t / \partial z$). A buffer depth of 75 m was chosen because it is the smallest depth which is always larger than the thickness of the region of significant q_t gradient in our simulations.

3.3 Initialization and Forcing

We initialize and force the model with data from the EPIC Sc dataset described in Section 1.6. In order to avoid nudging the modeled free-troposphere toward BL values when the model's z_i falls below that of the observations, we replace the BL component of the input θ_l and q_t profiles with data interpolated linearly from the overlying soundings. We apply ECMWF advection and w_s instead of NCEP values because these were found to be more believable in Chapter 2. The dataset only includes subsidence at 850 mb, so we construct profiles by assuming w_s increases linearly with height from a surface value of zero. Advection of z_i is absorbed into the subsidence by adding $-\mathbf{v} \cdot \nabla_h z_i$ to $w_s(850$ mb) before creating profiles. While estimates of N_d are included in the dataset, most of our simulations are based on fixed droplet concentrations because this timeseries is quite uncertain due to the lack of reliable in-situ aerosol and cloud microphysical measurements and because this assumption simplifies comparisons.

3.4 Results

3.4.1 Base Simulation

Our base run is a 3D simulation with fixed $N_d = 100$ cm^{-3}. Tables 3.1 and 3.2 compare the 6-day mean q_t and s_l budgets from this simulation with those derived in Chapter 2.

Table 3.1: Mean and standard deviation for each term in the q_t budget (2.1) from the 3D control run. Terms are derived and signed following the conventions for Table (2.1). Mean values from this earlier table (using ECMWF advections and subsidence) are included here for convenience.

	$-\frac{L\hat{p}_i}{g}\frac{\partial\langle q_t\rangle}{\partial t}$	$-\frac{L\hat{p}_i}{g}\langle \mathbf{v}\cdot\nabla_h q_t\rangle$	LHF	$LF_p(0)$	$\frac{L}{g}\hat{\omega}_e\Delta q_t$	Residual
Obs Mean:	-6	-26	99	-5	-68	-6
LES Mean:	1	-27	108	-4	-75	3
LES St. Dev:	6	6	3	1	4	1

Table 3.2: As for Table 3.1, but for the s_l budget (2.2).

	$-\frac{\hat{p}_i}{g}\frac{\partial\langle s_l\rangle}{\partial t}$	$-\frac{\hat{p}_i}{g}\langle \mathbf{v}\cdot\nabla_h s_l\rangle$	SHF	$-LF_p(0)$	$-\Delta_{\mathrm{BL}}F_R$	$\frac{1}{g}\hat{\omega}_e\Delta s_l$	Residual
Obs Mean:	1	-19	14	5	-52	41	-10
LES Mean:	-2	-20	13	4	-46	53	2
LES St. Dev:	4	3	1	1	2	3	3

The overall agreement is quite impressive, but we note that these budgets are strongly controlled by the mean entrainment rate, which has been tuned using σ_g to match observations. Modeled entrainment fluxes are slightly overestimated, which results in a drier BL and causes a slight increase in modeled LHF over observations. Radiative cooling is somewhat underestimated because model LWP is underpredicted.

The timeseries of modeled LWP is compared to the EPIC observations in Fig. 3.3a. Aside from day 293, the model does a reasonable job of reproducing the observed LWP timeseries, albeit with a bias toward low values. In particular, this run captures the observed diurnal variability in LWP very well, suggesting that sensitivity studies with SAM are a useful tool for better understanding the variations sampled during EPIC. Model cloud fraction is frequently lower than observed (Fig. 3.3b).

The strong decrease in LWP and cloud fraction around day 293 appears to be due to the combination of strong dry advection and weak cold advection which begins on day 292 (Fig. 3.4). Simulations using 6-day mean advections (not shown) did not show this decrease around day 292-293, but were unsuitable for analysis because they had much
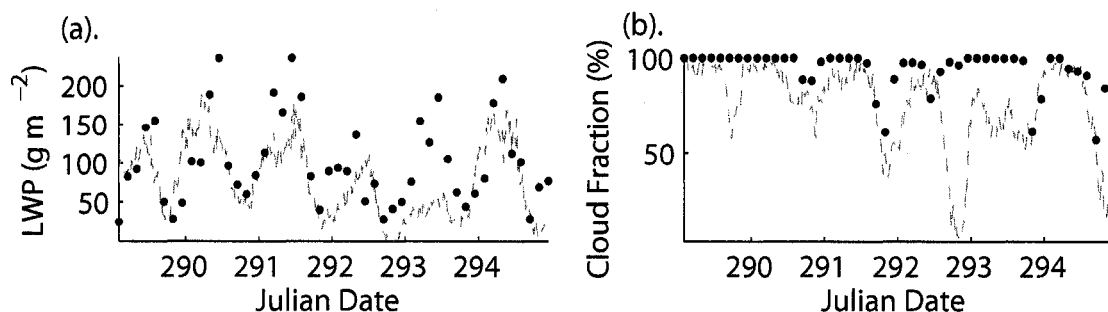
Figure 3.3: Timeseries of (a) LWP and (b) cloud fraction from the 3D base simulation (dashed line) and the observations (dots).
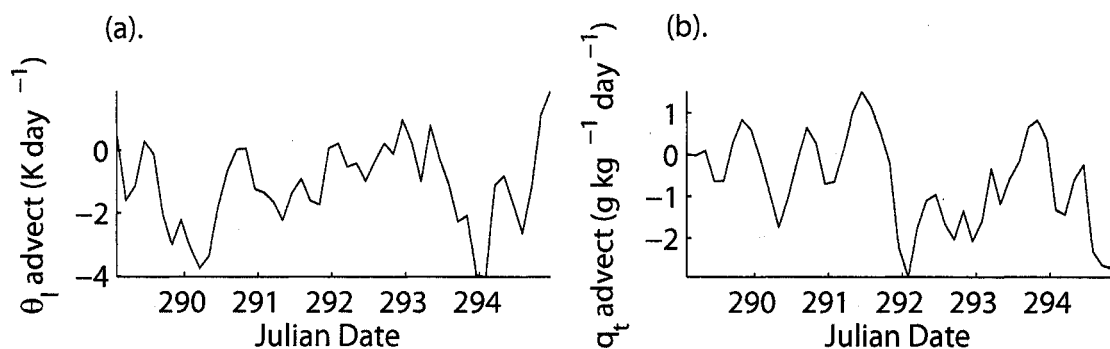
Figure 3.4: Horizontal advection used to force the LES simulations.

thinner clouds in general.

Fig. 3.5a shows the timeseries of modeled and observed surface drizzle. The model appears to capture drizzle events fairly well in all cases except during the previously discussed period between day 292 and 293, but with a tendency towards premature initiation. Additionally, the strength of surface precipitation is significantly overestimated by the model. Both early initiation and overprediction suggest that the drizzle scheme is too sensitive to LWP. This hypothesis is substantiated in Fig. 3.5b, which shows the relation between cloudbase drizzle and LWP/N_d. Since both axes on this plot are

(a).

(b).
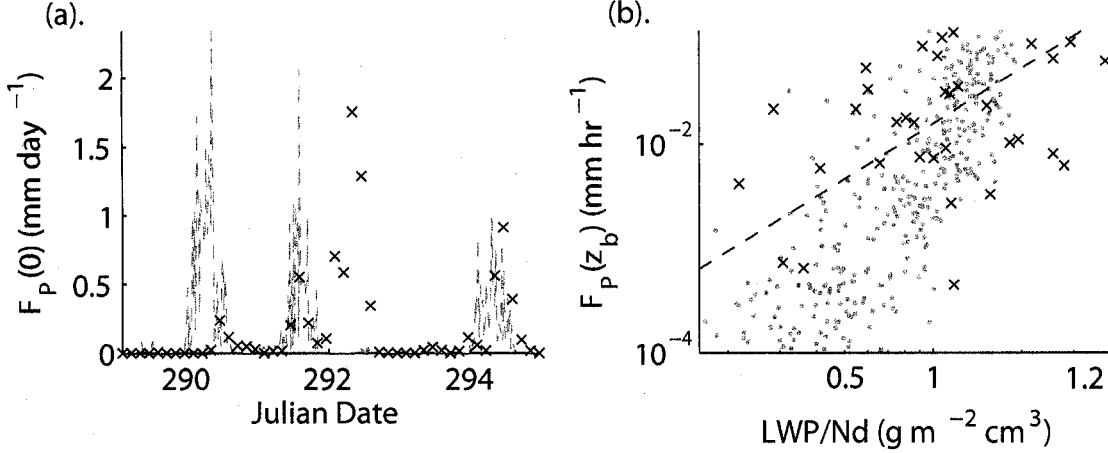
Figure 3.5: (a) Timeseries of surface drizzle from base simulation (gray line) and as observed by C-band radar (black crosses). (b) Comparison of control-simulation cloud-base drizzle rates (gray dots) with values computed from the 5 cm scanning radar (black crosses) and with the empirical relation to LWP and N_d derived in Comstock et al. (2004) (black dashed line).

log-scaled, straight lines on this graph denote a relation of the form

$$F_P(z_b) = A \left[\frac{\text{LWP}}{N_d} \right]^B \tag{3.1}$$

where A and B are constants related to the line's y-intercept and slope, respectively. The best-fit line to mm-wavelength vertically pointing radar from EPIC (derived in Comstock et al., 2004) has $A = 0.0156$ and $B = 1.75$ and is included in this figure as a black dashed line. The best-fit relation from SAM data, on the other hand, takes $A = 0.007$ and $B = 3.58$. Clearly, the KK scheme is much more sensitive to LWP[2] than expected from the EPIC data. Similarly, the relationship between $F_P(z_b)$ and cloud thickness in our simulation is stronger than found in previous studies (Pawlowska H. and J.-L. Brenguier, 2003; Vanzanten et al., 2005; Wood, 2005). Part of this discrepancy may result from the fact that drizzle increases nonlinearly with LWP, so A and B will be decreased when $F_P(z_b)$ and LWP are averaged over non-drizzly regions. The model A and B are based on

---

[2]N_d sensitivity can't be tested here since N_d is fixed at 100 cm^{-3} in this run.
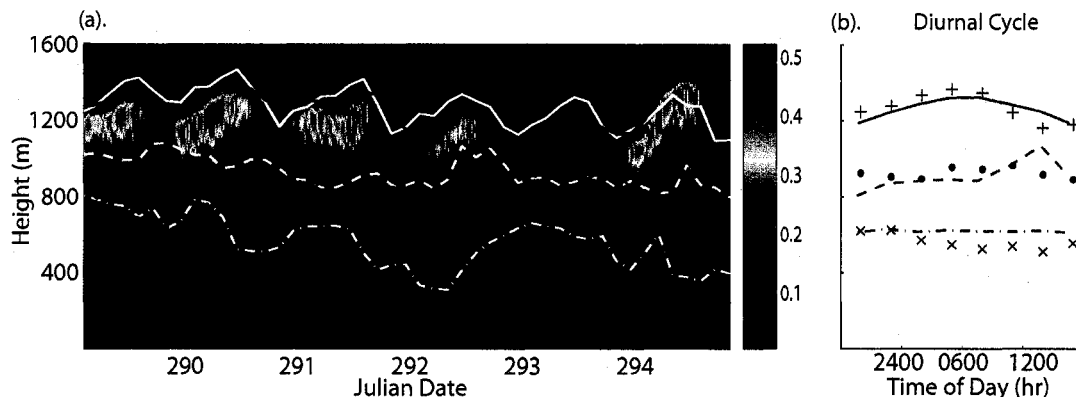
Figure 3.6: (a) Timeseries of model q_l in g kg^{-1} (color) along with model (red) and observations (white) of z_i (solid lines), z_b (dashed lines), and LCL (dot-dashed lines). (b) Diurnal cycle of z_i, z_b, and LCL. Color and linestyle for model are as in (a) while observations are in black pluses, dots, and xs, respectively.

data averaged over the domain and over 20 min intervals (longer averaging doesn't change the results), while the Comstock et al. (2004) relationship is based on 3 hr averages from a single spatial point. As a result, it is difficult to detangle which is "more averaged". On the other hand, the small domain size of the model may be preventing regions of intermediate LWP (and hence lower $F_P(z_b)$) from forming, which would artificially increase A and B. It should also be noted that (as in all precipitation measurements) there is substantial uncertainty in the Comstock et al. (2004) parameterization. Evidence of this can be found in Fig. 3.5b by noting that the cm-wavelength data don't follow the same slope as the Comstock et al. (2004) line, which was computed by sampling the same clouds, but with a mm-wavelength vertically-pointing radar.

The timeseries of q_l, z_i, z_b, and LCL from the base simulation are compared with the observations in Fig. 3.6. As expected for well-mixed Sc, the modeled liquid water content increases smoothly with height and there is no sign of scud or cumulus detraining into the Sc. Peak q_l is relatively modest at around 0.5 g kg^{-1}. The modeled cloud-top height matches the observations quite well in the mean, but underestimates the diurnal cycle (panel (b)). Since entrainment is directly related to cloud-top evolution through (2.3), this implies that the model is reproducing the mean entrainment rate, but is underpredicting

its diurnal amplitude relative to the observations. The question of whether this reflects an error in the model or in the observations is examined further in Section 3.4.1.

For this study, cloud base is taken as the domain-median value from each 3D output timestep for consistency with the observed value. While the observed cloudbase remains approximately constant throughout the study period, the modeled z_b tends to rise during the day and descend at night. This is probably due to extra entrainment warming and drying in the model during the day and enhanced entrainment cooling and moistening at night. Interestingly, model-observation agreement in LWP is improved by cancellation of z_i and z_b errors. This cancellation emphasizes the necessity of using multiple metrics for assessing model performance.

Also included in Fig. 3.6 are observed and modeled LCL. The difference in composite diurnal cycle LCL between model and observations is again consistent with larger daytime entrainment in the model. While the observed LCL drops during the day in response to decreased entrainment (as described in Section 2.4.2), the modeled LCL (which sees much steadier entrainment) remains constant. The difference between LCL and cloudbase is useful as a measure of BL stratification and therefore mixing. The fact that this difference is approximately the same in both model and observations suggests that both experience about the same level of mixing. Extensive examination of q_t and s_l profiles (not shown) support this conclusion.

To the extent that our LES simulation parallels reality, it provides us with a wealth of data fields not sampled during the EPIC cruise. With these "synthetic observations", we can investigate a variety of questions which would be intractible based on the EPIC data alone. One such question is what determines the degree of stratification found in the EPIC BL. Since vertical velocity variance $\overline{w'w'}$ measures the strength of the motions which mix the BL, examination of this quantity is a natural starting point. Profiles of $\overline{w'w'}$ averaged over each 3-hr period of the simulation and grouped by day are plotted in Fig. 3.7. Unsurprisingly, $\overline{w'w'}$ is weaker during the day (gray lines) than at night (black lines). As noted in Section 1.4, this is the result of decreased cloud-top radiative cooling due to SW absorption. More interesting, almost all $\overline{w'w'}$ profiles show a bimodal
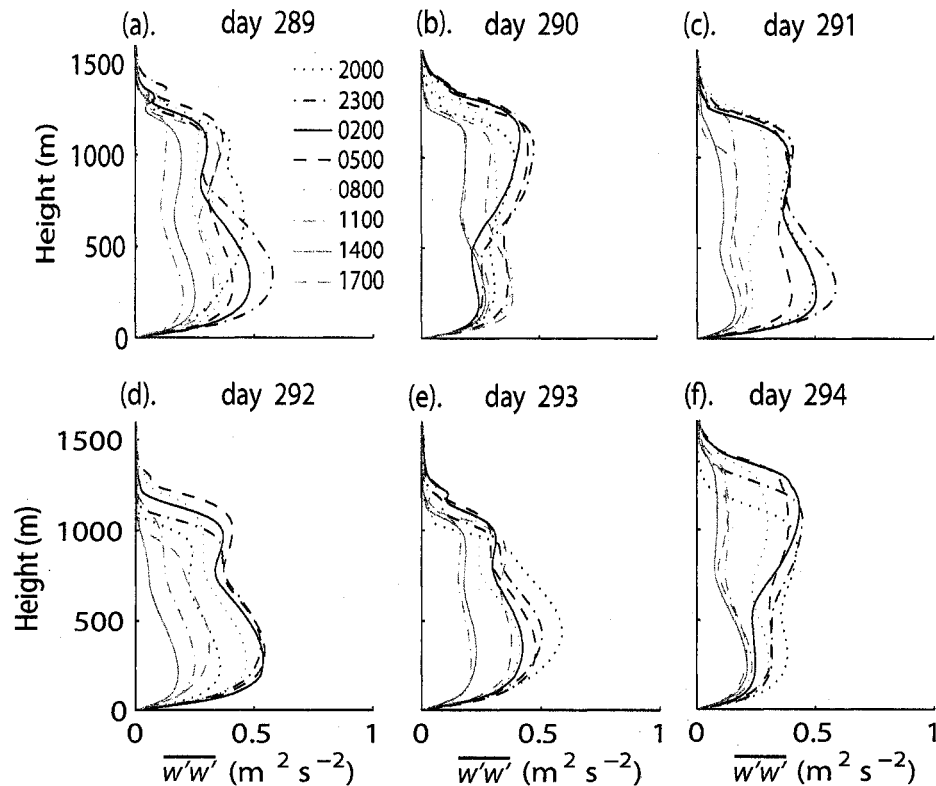
Figure 3.7: Profiles of $\overline{w'w'}$ from the 3d control run. Each profile is computed by averaging over the domain and over the 3 hr period centered at the time noted on the legend.

structure with a distinct minimum in the middle of the BL. This indicates that even at night the BL is not fully coupled. At some point comparison with observed $\overline{w'w'}$ below cloudbase should be possible based on vertical air velocity measurements from a NOAA ETL upward-pointing Doppler lidar which was operating during the cruise, but this data is yet to be processed.

An odd feature of Fig. 3.7 is that the subcloud peak in $\overline{w'w'}$ is often larger than the cloudy peak. This behavior seems to be associated with convective bursts which may be an artifact of our small domain size. These pulses are buoyancy-driven and are easily visible against a background state of near-zero subcloud buoyancy flux in Fig. 3.8a. Aside from these pulses, the BL shows the typical top-heavy $\overline{w'b'}$ structure described in

62
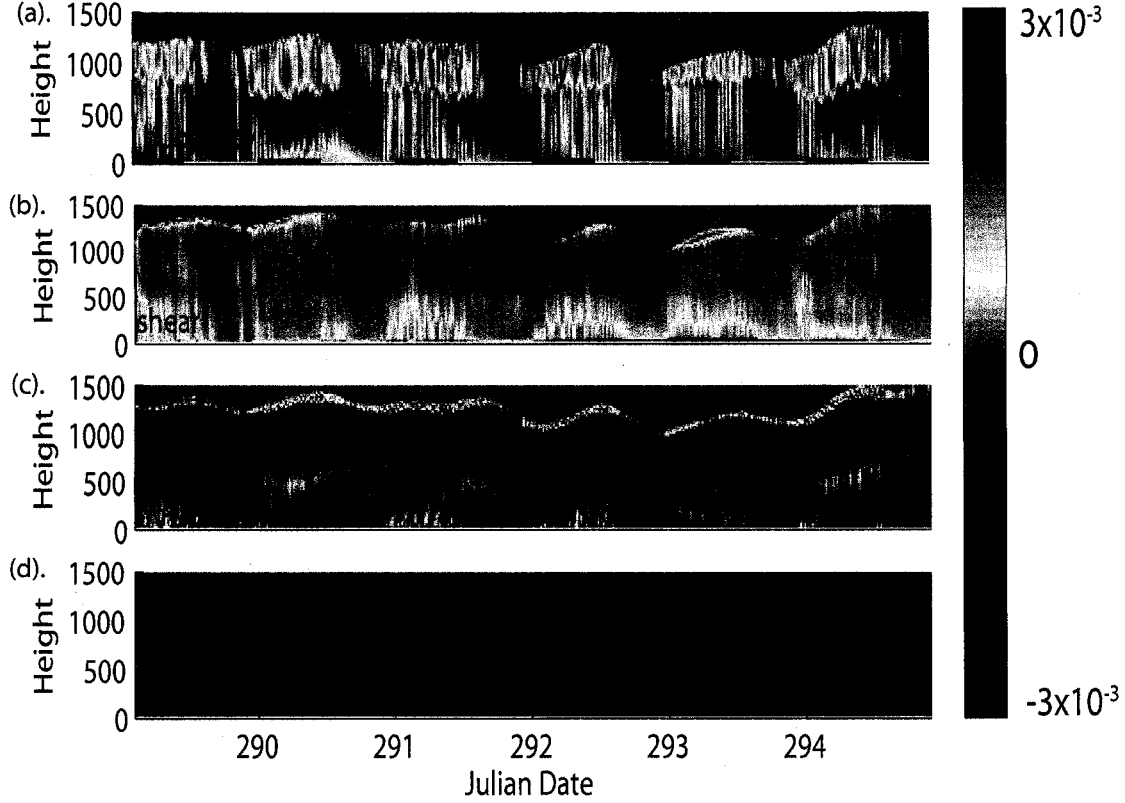
Figure 3.8: Timeseries of TKE budget terms from 3D base simulation (in m^2 s^{-3}). Storage (negligibly small) is omitted. Nighttime values are indicated by black lines along the base of panel (a).

Section 1.4. Buoyancy flux is much stronger during nighttime hours (indicated by black lines at the bottom of the plot), and almost dies out completely during daylight hours. The model fails to capture the pre-dawn decrease in subcloud $\overline{w'b'}$ noted in Section 2.4.3. This is unsurprising because this decrease was hypothesized to result from the observed early-morning peak in drizzle which is not present in the model (Fig. 3.5a).

The remaining terms in the BL TKE budget are included in panels (b)-(d) of Fig. 3.8. In accordance with expectations, $\overline{w'b'}$ is seen to be the dominant source of TKE away from the surface layer. Nonetheless, shear does occasionally play an important role near the surface when turbulence (and therefore the potential for wind shear) is strong.
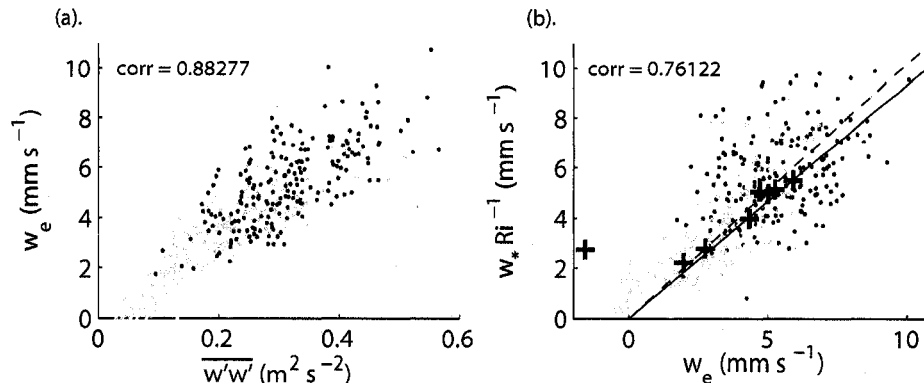
Figure 3.9: (a). Relation between w_e and $\overline{w'w'}$ for 3D base simulation and (b) relation between w_e and buoyancy driving (following Fig. 2.11). In each panel, model values are dots and observations are pluses. Daytime values are light gray and nighttime values are dark gray except for the diurnal mean observations in panel (b), which are all colored black.

It is possible that our nudging procedure is artificially enhancing shear, but since shear is relatively small anyways this is probably not a major concern. An odd and unexplained feature of this simulation is that the TKE generated in the cloud layer by buoyancy flux is not generally dissipated in situ, but rather transported downward and removed near the surface. This is in contrast to LES of shallower marine Sc layers, which show substantial TKE dissipation in the cloud layer (e.g. the intercomparison by Stevens et al. (2005b), in which the SAM TKE budget was quite typical).

Entrainment

In addition to controlling the degree of mixing in the BL, turbulence determines entrainment. Evidence of this is found in Fig. 3.9a, which compares model w_e^3 to the vertical velocity variance at $0.9\,z_i$. The extremely tight correlation between these quantities suggests that entrainment in SAM is driven by eddies rather than numerical diffusion. Because of this, weaker turbulence during the night (as noted in regard to Fig. 3.7) results in lower entrainment rates during the day (light dots) than at night (dark dots).

[3]computed as the residual of the mass budget (2.3).

64
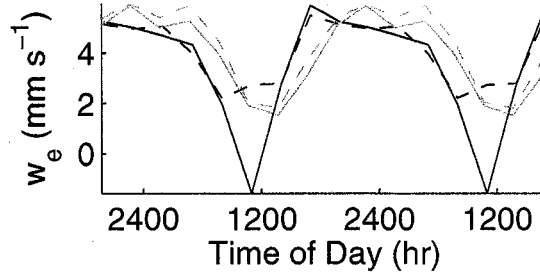
Figure 3.10: Comparison between composite diurnal cycle of w_e (solid lines) and $w_* \text{Ri}^{-1}$ (dashed lines) for model (gray) and observations (black). The diurnal cycle has been repeated twice for clarity.

For turbulence parameterization, one must also predict any turbulence statistics (e.g. w'w') used to deduce the entrainment. It is often simpler to predict the energy source for the turbulence (typically the buoyancy flux in convective boundary layers), and relate the entrainment rate to this. Several such parameterizations were compared to the observed data in Section 2.4.4. The most basic of these relations, which simply relates entrainment to the buoyancy driving (embodied by $w_* \text{Ri}^{-1} = w_*^3/(\Delta b z_i)$) was found to match the observations quite well, with slope $A = w_e \text{Ri}/w_*$ of 1.1. In Fig. 2.4.4b, this analysis is repeated for the LES data. The model fit to the data is quite good (correlation 0.76) and the least-squares slope (constrained to pass through the origin) of $A = 1.0$ is almost indistinguishable from that of the observations. Such agreement is quite surprising in light of the model's apparent inability to reproduce the observed diurnal cycle of entrainment.

This mystery is investigated further in Fig. 3.10, which compares the diurnal cycle of $w_* \text{Ri}^{-1}$ and w_e for model and observations. As expected on the basis of Fig. 3.9b, $w_* \text{Ri}^{-1}$ is a good predictor of entrainment most of the time. Further, we see that the diurnal amplitude of model w_e is only too weak because of the single very low value of observed w_e at 1100 LT. This time is also the only point on this figure which doesn't obey the $w_* \text{Ri}^{-1}$ scaling.

There are two possibilities for why the observed 1100 LT point doesn't match this scaling. One possibility is that some sort of regime transition is occurring around midday,

during which time entrainment is limited by some other process. Since it is hard to imagine what this process may be, this option seems unlikely. The other possibility is that the 1100 LT point from the mass budget is wrong. This must be somewhat the case since the midday entrainment observation is negative, which is unphysical. Further, partial decoupling is likely around midday, making the observed w_* for this time (computed assuming well-mixed conditions) relatively uncertain. At first glance, the discrepancy between modeled and observed diurnal amplitude in z_i appears to provide independent verification that it is the model which is wrong. This is not the case since the observed w_e was derived from the mass budget relation $w_e + w_s - \mathbf{v} \cdot \nabla_h z_i = \partial z_i / \partial t$. Since the model was forced with the same $w_s - \mathbf{v} \cdot \nabla_h z_i$ as used the mass budget, disagreement about the diurnal cycle of w_e is a direct consequence of the disagreement in z_i. It is possible that the observed midday z_i is underpredicted since the difference between cloud top and BL top increases during the day (making it difficult to accurately assess z_i) and because the uncertainty implicit in determining z_i from a single radiosonde profile every three hours is substantial. Nonetheless, all three independent budgets support the notion that entrainment is lower around midday than predicted by the LES.

It should be noted that good model-observation agreement in entrainment efficiency A is potentially the result of tuning σ_g. Without this tuning, the entrainment efficiency would likely be much higher. Still, this tuning is unlikely to affect the impressively tight correlation between w_e and $w_*\text{Ri}^{-1}$ found in the model.

Additionally, tuning σ_g may actually be artificially damping the diurnal cycle of w_e since the effectiveness of σ_g damping is proportional to the amount of liquid water at cloud top, which is much higher at night (when entrainment should be high). An alternative technique for dealing with overentrainment (employed in Duynkerke et al., 2004) is to allow entrainment to evolve freely while tuning w_s to keep z_i in check. We performed a 2D sensitivity study employing this technique and did find it to increase the diurnal cycle of z_i by about 100 m over the first day (compared to a 2D base simulation). Unfortunately, allowing the model to overentrain causes the BL to dry and warm, resulting in a complete loss of cloud after 2 days of simulation. How to optimally deal with model

overentrainment is a question which becomes increasingly important as LES are run for longer periods. Obviously, using a model which correctly simulates entrainment would be ideal. Increasing vertical resolution beyond 5 m may be a step in this direction, but this would add considerable expense to simulations which are already computationally taxing. In the absence of a perfect model, one must choose between techniques which artificially influence the entrainment process and those which attempt to correct for overentrainment by changing forcings. Determining the best way to do this is an important problem for future studies.

Another interesting feature of Fig. 3.10 is the timing of the diurnal cycle, which appears to be shifted about 3 hours later in the LES. Since the onset of decreased turbulence in the observations is theorized to result from an early-morning drizzle maximum which is absent in the model (which instead drizzles all night, Fig. 3.5a), this shift is perhaps unsurprising. Additionally, the 3 hr delay in the upswing of model w_e is consistent with the fact that more spin-up time is required to restore mixing to the almost cloud-free BL found in the model in late afternoon (Fig. 3.3). Another possibility is that the timing of the mass-budget is wrong since entrainment from the s_l and q_t budget w_e show a lag similar to the model (Fig. 2.8). Still, incorrect timing in the mass budget w_e implies a systematic error in all of the daytime z_i profiles, which seems improbable.

The typical lengthscale of eddies driving entrainment is still unclear. Some studies (such as Lewellen and Lewellen, 1998) theorize that entrainment arises from the largest-scale motions, while others (e.g. Lilly, 2002b) suggest that entrainment is a more localized phenomenon. We investigate this issue in Fig. 3.11 by looking at the correlation between turbulence and entrainment as a function of height. Unsurprisingly, entrainment is better correlated to vertical velocity variance (panel (a)), than to buoyancy flux (panel (b)) or buoyant forcing (Fig. 3.9b) since $\overline{w'w'}$ measures the motions responsible for entrainment while $\overline{w'b'}$ measures the energy source for these motions. Better understanding of the transfer function relating these two quantities would be very useful for improving entrainment parameterizations, but is outside the scope of this research. The extremely high correlation with vertical motions in the top 70-90% of the BL (as well as the double-
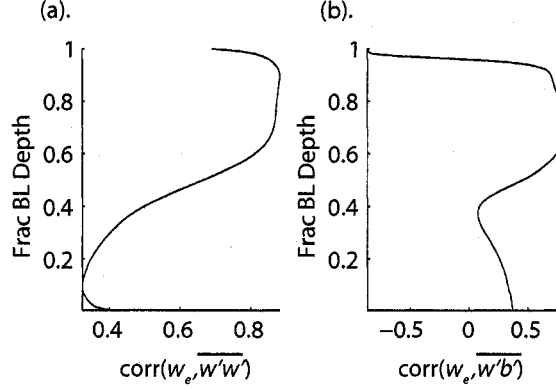
Figure 3.11: Correlation between domain-averaged values of entrainment and $\overline{w'w'}$ (panel (a)) or buoyancy flux (panel (b)) calculated at various fractions of the BL depth from the 3d control run.

peaked structure of vertical velocity variance, which suggests a separation of the eddy structures in the surface and cloud layers) suggests that the vertical motions responsible for entrainment have lengthscale less than 30% of the BL depth. This implies that Lilly's approach of weighting turbulence generation near cloud-top more heavily than near the surface is probably preferable to the w_* approach of Turton and Nicholls (1987).

3.4.2 Sensitivity to Model Configuration

The impact of our various modeling assumptions is compared in Fig. 3.12, which shows timeseries of z_i, z_b, and LCL for various run configurations. In panel (a), results from a 2D base simulation are compared with those from the 3D base simulation discussed above. This comparison is important because, as noted in Section 3.1, we lack the computational resources to do all of our sensitivity studies in 3D. Agreement between the two runs is quite good until day 292, when the cloud essentially disappears from both simulations (due, as noted in Section 3.4.1, to advection). While cloud rapidly reforms in the 3D simulation, the 2D run remains cloud free, which causes the BL to collapse due to a lack of cloud-top radiative cooling. The reason for this differing behavior is unclear, but could be related to the ability of the 3D simulation to store more TKE in horizontal motions.
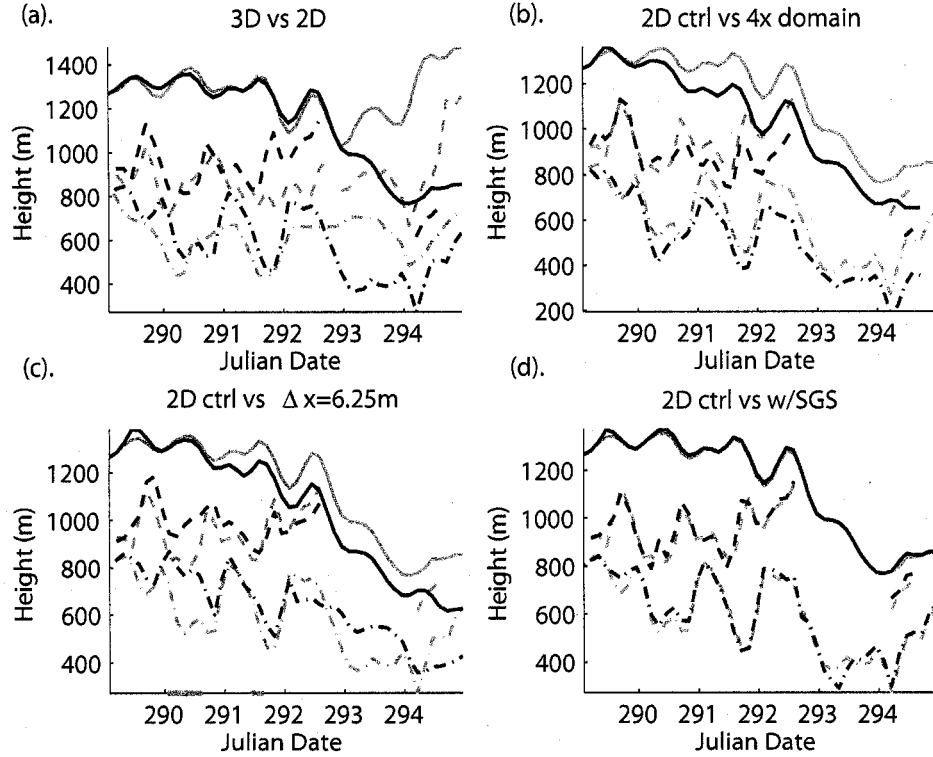
Figure 3.12: Comparison of z_i, z_b, and LCL from (a) 3D versus 2D base simulations, (b) 2D base simulation versus a similar simulation with 4 times larger domain, (c) 2D base simulation versus a similar simulation with $\Delta x = 6.25$ m, and (d) 2D base simulation versus 2D simulation with scalar SGS fluxes computed using Smagorinsky. In panel (c), times of surface drizzle > 0.25 mm day^{-1} are indicated by dots near the bottom of the plot. In all plots, the first run mentioned is shown in gray, the second in black.

This may result in a slower TKE loss rate and hence provide enough residual mixing to allow for reformation of cloud once the warm/dry advection spike passes. Another noteworthy difference between the 2D and 3D runs is the entrainment rate. While z_i (and thus entrainment) is approximately the same for the initial cloudy days of both runs, σ_g had to be slightly decreased to 1.9 in order to achieve this agreement. When σ_g is kept at 2.0, 2D runs underentrain significantly. The reasons for this are still unknown. The 2D case seems to have slightly less diurnal variation in z_i and thus w_e, again for reasons unknown.

The effect of increasing domain size on 2D simulations is investigated in panel (b). The larger domain run entrains slightly less (perhaps because pulses of $\overline{w'b'}$ are less common), resulting in slightly higher average LCL and z_b than found in the 2D base simulation. Nonetheless, model behavior in the large-domain simulation is qualitatively similar to that from the base run, suggesting that increased domain size is unlikely to change our results. Similarly, decreasing horizontal grid spacing from 25 m to 6.25 m causes entrainment and drizzle to decrease slightly, but otherwise makes little difference. This sensitivity is in the opposite sense as found in Stevens and Bretherton (1999), perhaps due to our use of an anisotropic eddy diffusivity. Since previous runs do not show this sensitivity, we regard the entrainment grid-size relation we find here to be spurious.

Finally, model sensitivity to use of the Smagorinsky SGS scheme for computing scalar fluxes is considered in panel (d). Differences in model behavior are almost imperceptible, leading us to conclude that inclusion of a SGS scheme for scalars neither helps nor hurts our simulation, a striking difference from the results reported in Stevens et al. (2005b) for the UCLA LES.

3.4.3 Sensitivity to Model Microphysics and Forcings

A great benefit of LES studies is that the effect of individual forcings can be isolated in a physically-consistent setting by repeating the control simulation with the forcing of interest changed. In Fig. 3.13 we use this technique to investigate the effect of diurnally-varying subsidence. In panel (a), we see that removing the diurnal cycle of subsidence results in a simulation with very little variation in z_i on the timescale of a day. If the real diurnal cycle of w_e is closer to the model-predicted value than to the observations as discussed in Section 3.4.1, this implies that subsidence is largely responsible for the observed diurnal cycle in cloud top. In the sensitivity simulation, decreases in cloudbase generally make up for damped variation in z_i, resulting in little change to the LWP. Other BL quantities, such as drizzle, surface fluxes, and mixing are quite similar for both simulations (not shown).

The effect of drizzle on the simulations is examined in Fig. 3.14. Four cases are con-

70
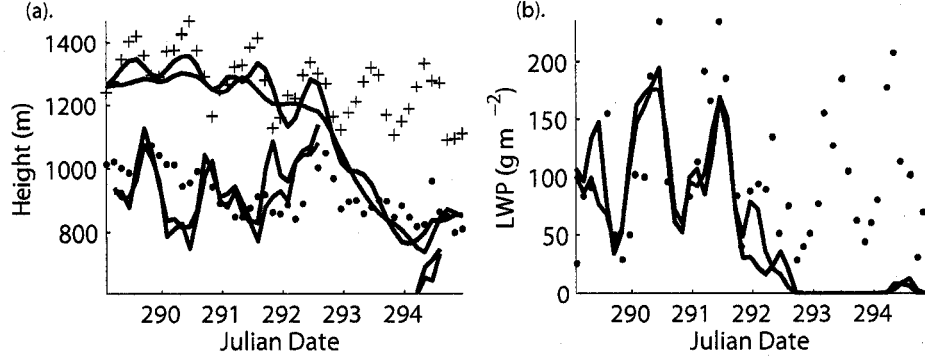
Figure 3.13: Timeseries of (a) z_i and z_b and (b) LWP from observations (black dots and pluses), from the 2D base simulation (blue lines), and from a run forced by the 24 hr running mean of the observed w_s (red lines).

sidered: drizzly cases with N_d fixed at 100 cm^{-3} and N_d fixed at 25 cm^{-3}, and companion runs at each of these droplet concentrations where drizzle has been artificially suppressed by turning off autoconversion. The drizzly run at $N_d = 100$ cm^{-3} only precipitates intermittently (panel (a)), while precipitation is frequent and substantial at $N_d = 25$ cm^{-3}. Interestingly, while the low-N_d case typically has much higher surface precipitation than the observations, cloudbase drizzle is frequently higher in the observations than in of any of the simulations. This suggests that the model underpredicts evaporation of falling droplets, perhaps because it neglects ventilation. Interestingly, in the shallower RF02 case, SAM predicted the fraction of drizzle evaporated below cloud base quite well (GCSS web site, Ackerman et al. 2007, unpublished manuscript). Early initiation of drizzle (compared to observations) is apparent in both the $N_d = 25$ cm^{-3} and $N_d = 100$ cm^{-3} simulations. This is probably associated with the model's oversensitivity of drizzle to LWP as discussed in Section 3.4.1.

Panel (b) shows that increasing drizzle susceptibility causes a strong decrease in daily-maximum LWP, but has little effect on the daily minimum (daytime) LWP. This appears to be due to LWP falling to such low values during the day that drizzle can't be sustained in any simulation (panel (a)), in which case model physics is essentially identical for all simulations until night falls and the LWP picks up again. Panel (c) shows that the
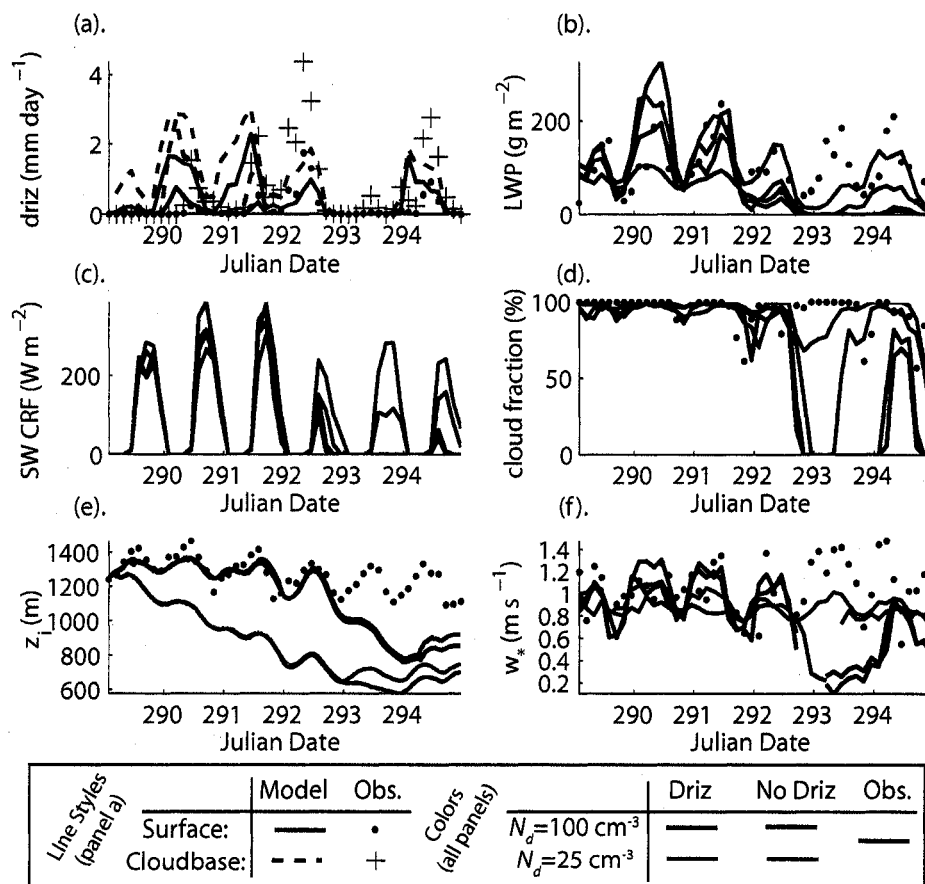
Figure 3.14: Effect of drizzle on 2D simulations.

non-drizzly simulation can nevertheless result in an enhancement of the shortwave cloud forcing of over 100 W m^{-2} relative to the heavily drizzling case due to the Twomey effect and to enhanced LWP during morning and evening hours.

Panel (d) shows that cloud fraction is essentially the same in all 4 simulations until the disappearance of cloud on day 293. This is somewhat surprising since the average LWP in the heavily drizzling simulation is half that in the non-drizzly case.

Perhaps the most interesting feature of this graphic is that the response of model z_i (and thus w_e) to N_d changes seems to be entirely unrelated to drizzle processes (panel (e)). Further runs with both drizzle and cloud droplet sedimentation turned off did not exhibit
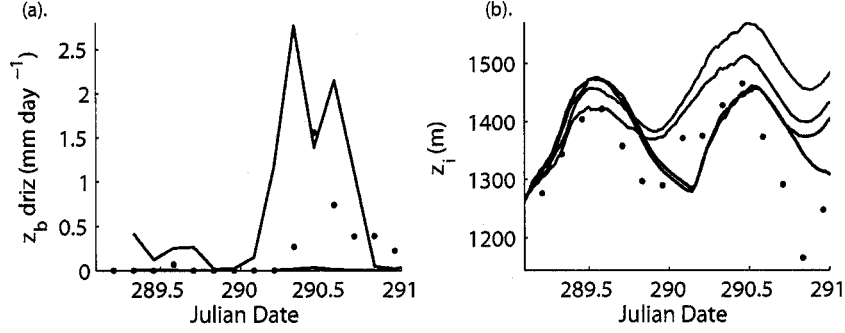
Figure 3.15: Cloudbase drizzle (panel (a)) and z_i (panel (b)) from simulations using $\sigma_g = 1.2$. Colors are as in Fig. 3.14.

N_d dependence (not shown), which leads us to conclude that entrainment is controlled entirely through cloud droplet sedimentation. It should be noted that the importance of cloud droplet sedimentation is enhanced in our simulations by artificially increasing σ_g. Subsequent runs with $\sigma_g = 1.2$ (Fig. 3.15) show more sensitivity to drizzle, but sedimentation still seems to dominate. In light of our results it seems inappropriate to associate entrainment response to N_d with drizzle processes as commonly assumed (e.g. Savic-Jovcic and Stevens, 2007).

It is interesting to note that the more weakly-entraining cases are better able to maintain cloud towards the end of the run. This is because z_i is much lower in these runs, making it easier to keep the BL well-mixed. This behavior reaffirms that we can associate decreased entrainment with longer cloud lifetime (as suggested by Stevens et al., 1998, and others).

Fig. 3.16 shows the timeseries of N_d taken from the EPIC-Sc dataset (described in Section 2.3.2) and the timeseries of $F_P(0)$, LWP, and z_i from a 2D run forced by these droplet concentrations. Unsurprisingly, drizzle is larger or smaller than that of the control simulation in rough accord with whether N_d is lower or higher than 100 cm^{-3}. What is more interesting is that the relation between increased drizzle and decreased LWP found for fixed N_d doesn't appear to hold in the varying case. For example, near the beginning of the run the $N_d = 100$ cm^{-3} simulation has more drizzle *and* higher
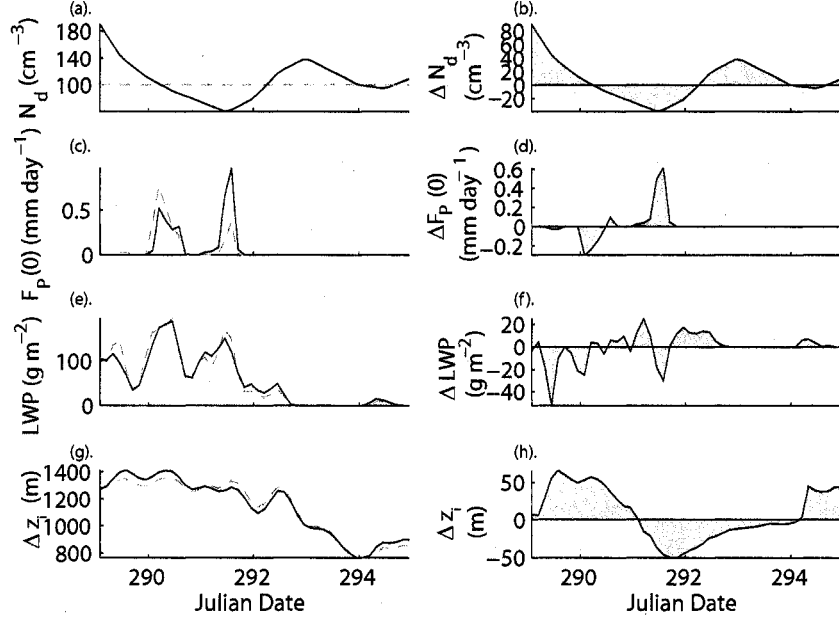
Figure 3.16: (a)-(b) Droplet concentration, (c)-(d) surface drizzle rate, (e)-(f) LWP, and (g)-(h) z_i from (1) the varying N_d run (black solid line) and (2) the 2D control simulation (dashed gray line). Panels on the right show the difference between the N_d-varying and control simulation.

LWP, then toward the end of day 291 the situation reverses. The situation is somewhat clarified by the last two panels, which show that entrainment tends to be larger for higher N_d (as discussed above). Thus changes in LWP with increasing N_d are a balance between decreased removal of moisture through precipitation and increased entrainment drying due to drizzle and droplet sedimentation.

3.5 Conclusions

In this study, we were able to reproduce many of the observed features from the EPIC-Sc dataset using the SAM LES. In particular, the model was able to reproduce the mean q_t and s_l budgets very well and to capture the observed BL stratification. In addition, the diurnal cycle of LWP was well-simulated, although this appears to be partially the result of canceling errors in z_i and z_b.

A surprising result of this study is that model entrainment appears to closely follow the relation $w_e = w_* \mathrm{Ri}^{-1}$ found in Chapter 2 even though comparison of the diurnal cycle of w_e and z_i suggests that the LES underpredicts the amplitude of the diurnal cycles of these quantities. The explanation for this seeming paradox is that while the observations fit the above relation most of the time, the midday w_e is significantly less than that predicted by the $w_* \mathrm{Ri}^{-1}$ relation. This suggests that entrainment observations are underestimated at this time in the observations or that the processes governing midday entrainment are different than those operating at other times.

Comparison between radar-derived precipitation profiles and the profiles generated by the Khairoutdinov and Kogan (2000) scheme suggest that the model is too sensitive to LWP and evaporation of drizzle below cloudbase is underpredicted.

Since the model was able to reproduce most of the observed aspects of the BL sampled during EPIC, it is a useful tool for understanding aspects of the BL not captured during the EPIC cruise. Vertical velocity variance (which was measured during the cruise but hasn't been processed) is one such quantity. Profiles of this quantity from the model typically had a double-peaked profile and below cloud base, intermittent pulsing of turbulence was common. These suggest that the LES is maintaining a marginally-decoupled state much of the time, even when it is is relatively well-mixed as measured by vertical moisture stratification. Correlation between $\overline{w'w'}$ and w_e for various heights in the BL suggests that the typical lengthscale of entraining eddies in the model is less than 0.3 times the BL depth, which suggests that a transfer function between buoyancy flux and entrainment which is weighted more towards cloud top is probably superior to the BL average typically used.

Sensitivity studies were also performed to investigate the importance of subsidence and drizzle to BL dynamics. Removing the diurnal cycle of subsidence resulted in weaker diurnal variation in cloud top. This change had little impact on the LWP due to compensating variations in cloudbase. Two sensitivity studies were performed to assess the importance of drizzle. In one study, autoconversion is turned off, preventing the formation of drizzle. This results in much stronger daily-maximum LWP and resultingly stronger

SW cloud forcing during the early morning and late afternoon but had little effect on daily minimum LWP. Surprisingly, BL depth was almost entirely unaffected by eliminating drizzle as long as cloud droplet sedimentation is left unaltered. However, when droplet concentration was decreased to 25 cm^{-3} (a factor of 4 decrease), entrainment was substantially decreased and LWP was substantially reduced from the control run. This w_e difference appears to be the result of increased droplet sedimentation associated with dividing cloud-top liquid water into fewer drops. On the other hand, simulation-mean cloud fraction was substantially enhanced in this run due to the improved ability for the BL to mix associated with decreased z_i.

This study provides hope that LES simulations of the diurnal cycle of Sc are not only possible but also illuminating. Better understanding of how to handle model overentrainment and the computational resources to simulate a larger region less susceptible to domain-scale convective pulsation would also aid our understanding.

Chapter 4

RESPONSE OF A SUBTROPICAL STRATOCUMULUS-CAPPED MIXED LAYER TO CLIMATE AND AEROSOL CHANGES

4.1 Introduction

As noted in Chapter 1, Sc response to global warming may play a major role in shaping our future climate, but the nature of that role is still unclear. Because of the relative steadiness of airflow in the subtropics, an idealized model of subtropical Sc response to global warming is a natural starting point for investigating BL cloud feedbacks.

Several models of this type have already been proposed. Pierrehumbert (1995); Miller (1997); Larson et al. (1999) and Clement and Seager (1999) have devised models which divide the tropics into two boxes, one for deep convective regions and the other for Sc regions. In each case, simple parameterizations for thermodynamic properties in each box and for the coupling between boxes were provided and tests were performed to investigate model response to climate change. Several of these models (Miller, 1997; Larson et al., 1999; Clement and Seager, 1999) have included the positive empirical correlation between cloud fraction and lower tropospheric stability (LTS) found by Klein and Hartmann (1993). Since lower tropospheric stability increases with warming, these models predict that Sc will provide a negative feedback on warming due to increased cloud albedo. However, while LTS has proven useful for predicting geographical and seasonal variability in the current climate, it may not be an appropriate measure of low cloudiness in a warmer climate where free-tropospheric lapse rate is systematically decreased (Williams et al., 2006; Wood and Bretherton, 2006; Medeiros et al., 2007). Other potentially important BL cloud feedbacks, such as increased albedo due to cloud thickening or to increased liquid water path at fixed cloud depth (e.g. Somerville and Remer 1984), have not been investigated in the context of a simple model.

In this study we develop an idealized single column-model which includes these miss-

ing feedbacks. As in previous 2-box models, the free troposphere above the Sc-topped BL in our model is determined by a moist adiabat based on ITCZ SST. Unlike previous work, where BL cloud properties are essentially computed as a residual of large-scale balance conditions, our model is based on physically-consistent parameterizations of BL processes. For example, our model is the first to include precipitation in the Sc region and we handle radiative transfer more carefully. Additionally, we extend the mixing-line parameterization used in previous studies under the assumption of well-mixedness to derive buoyancy flux profiles (following the methodology of Chapter 2)and hence entrainment rates which are consistent with BL energetics. The resulting framework, first introduced by Lilly (1968), is commonly called the mixed-layer model (MLM). The MLM is only physically correct under well-mixed and horizontally homogeneous conditions. Such conditions are only found in the heart of the subtropical Sc regimes, not in the area of transition from Sc to trade cumulus convection. While our approach could easily be generalized to include these regions by replacing the MLM with a single column or LES model of BL, we use the MLM because its simplicity and internal consistency permit an attractive physical understanding of its cloud feedbacks. Our study also differs from 2-box models in that ITCZ SST is a free parameter. This leaves us with a 2-parameter (SST_{ITCZ} and SST_{Sc}) family of solutions, but frees us from making assumptions about how the Sc region feeds back on the ITCZ.

Section 4.2 documents our model design, section 4.3 discusses numerical model solutions, and section 4.4 provides insight into model behavior by developing and analyzing analytic model solutions in a simplified setting. Section 4.5 presents conclusions from this Chapter.

4.2 Model Design

Our model is explained diagrammatically in Fig. 4.1. The ITCZ region is included as a degenerate box completely determined by SST_{ITCZ}. It influences the Sc region directly by determining the free-tropospheric temperature profile (taken to be horizontally uniform and to follow a modified moist adiabat) and indirectly by setting free-tropospheric
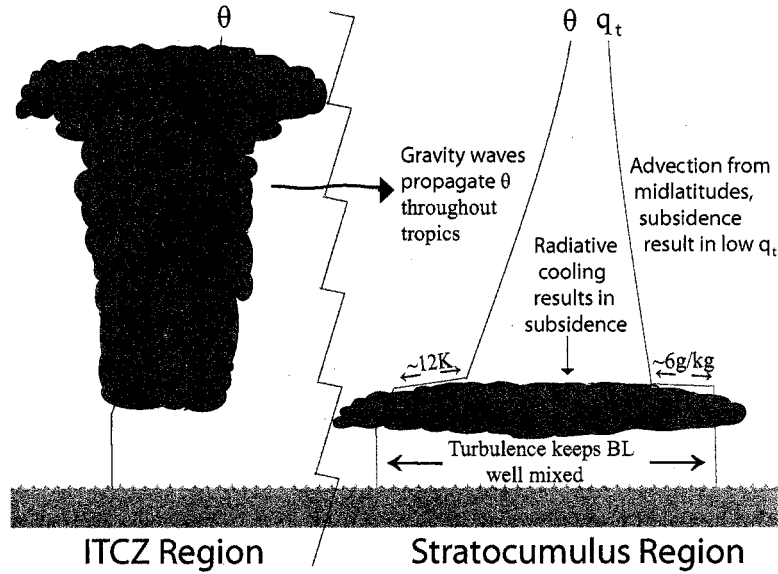
Figure 4.1: A diagrammatic description our modeling philosophy.

humidity (assuming a constant relative humidity) and subsidence rate (assuming steady-state energy balance). The MLM interacts with this free-tropospheric profile and the underlying SST_{ITCZ}. Although the theory is straightforward, translating this concept into a faithful model of an actual Sc-topped BL requires attention to many details, to which the remainder of this section is devoted. Free-tropospheric model parameters are chosen to roughly correspond to observations over the SE Pacific - the world's largest low-latitude Sc region.

4.2.1 Free-Tropospheric Model

Because of the large Rossby radius, horizontal temperature variations in the tropics tend to be small (Charney, 1963; Sobel et al., 2001). As a result, free tropospheric temperature in the subtropical Sc regions is strongly dependent on the ITCZ temperature profile and

responds roughly in lockstep to changes in the latter (Wyant et al., 2006).

The ITCZ temperature profile is assumed to be nearly moist adiabatic due to deep convective adjustment, with slight conditional instability in the lower free-troposphere due to lateral entrainment/detrainment in convecting plumes. We follow Betts (1986) and Betts and Miller (1986), who empirically estimated the stratification in regions of persistent tropical deep convection to be

$$\frac{\partial \theta_0}{\partial z} = \gamma \left(\frac{\partial \theta_0}{\partial z} \right)_{\text{moist adiabat}} \quad \text{with } \gamma = 0.85. \tag{4.1}$$

where θ_0 is a 'reference' ITCZ-average free-tropospheric potential temperature. A temperature profile is calculated by integrating this equation up from an ITCZ cloud base, determined as the lifting condensation level of a near-surface parcel with temperature $SST_{ITCZ} - 1$ K, pressure 1008 mb, and 80% relative humidity (RH). Below ITCZ cloud base, a smooth reference temperature profile is maintained by integrating (4.1) down to the surface. While Betts (1986) applies a separate parameterization above the freezing level to account for latent heat release due to freezing, we apply (4.1) to all tropospheric levels to better match observations from the EPIC and Pan American Climate Studies (PACS, Kollias et al. 2004) campaigns at 20°S, 85°W. The tropopause is diagnosed as the level where the reference temperature profile crosses the 195 K isotherm. Stratospheric temperature and humidity are taken from the McClatchey et al. (1971) tropical sounding with pressure levels regridded to fit between the diagnosed tropopause and the top of the atmosphere.

In Fig. 4.2, our $SST_{ITCZ}=302$ K reference temperature profile is compared to radiosonde data from EPIC. In this plot, dots are the average of three-hourly data taken between Oct. 16th and 22nd 2001 as part of EPIC, squares are from data at roughly 6-hourly increments taken between Nov. 14th and 25th during the PACS 2003 cruise, and triangles are from similar data taken between Dec. 5th and 22nd 2004 as part of PACS 2004. The Betts parameterization fits the data quite well and is obviously superior to the moist adiabat, included as a dashed line. Above- and below-freezing regions of this plot are separated by a dotted line. There is no clear difference in lapse rate on either
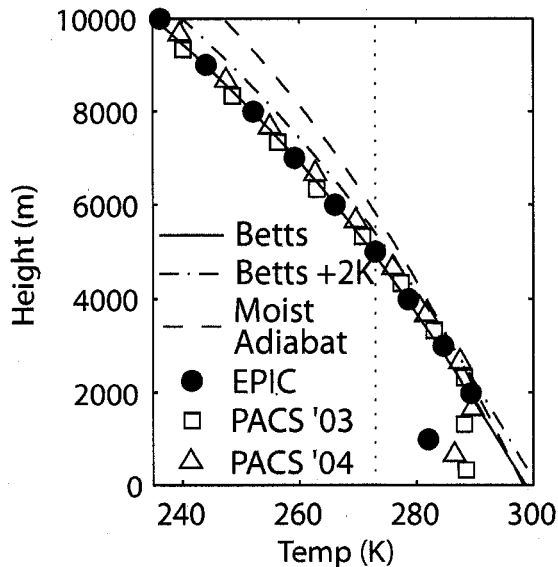
Figure 4.2: Comparison of Betts' temperature parameterization with data from the EPIC, PACS 2003, and PACS 2004 campaigns at 20°S, 85°W. A moist adiabat is included to illustrate its poor fit. A dotted line is drawn through 273 K to emphasize that the slope of the observations doesn't seem to change at the freezing level.

side of the freezing line.

Also included as a dot-dashed line on this plot is the Betts parameterization based on an SST_{ITCZ} which has been warmed by +2K. This line has been included to illustrate the lapse rate feedback operating in our model. This feedback results from the exponential-like increase in saturation mixing ratio with temperature (as embodied in the Clausius-Clapeyron relationship), which causes condensational heating to increase for a moist adiabat tied to warmer SST. As a result, temperature perturbations increase with height in a model using a moist adiabatic temperature profile. This well-documented effect (e.g. Hansen et al. 1984) plays an important role in our model response.

Both modeling and observational studies suggest that RH is relatively unaffected by small climate perturbations (Houghton et al., 2001; Soden et al., 2002). For this reason we assume a fixed 10% RH at all free-tropospheric levels, a value that matches cruise-mean profiles of water vapor mixing ratio q_v at 20°S, 85°W to within synoptic variability,
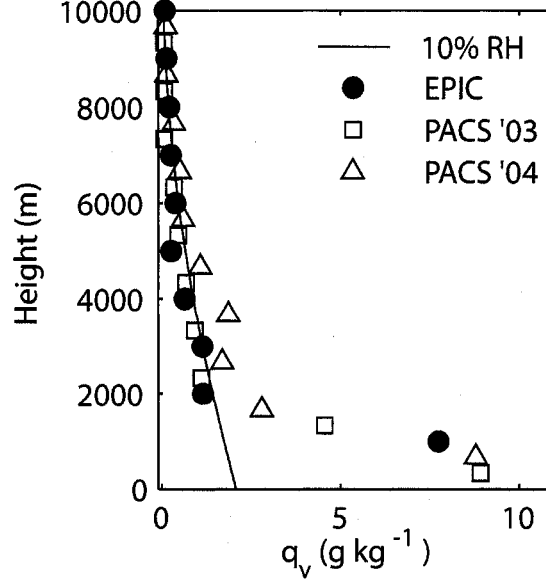
Figure 4.3: Comparison of 10% RH profile with data from EPIC, PACS 2003, and PACS 2004.

as seen in Fig. 4.3.

From these temperature and moisture soundings, reference radiative flux profiles F_{R0} may be generated. We use the 2-stream correlated-K radiative transfer model BUGSrad (Stephens et al., 2001) with solar constant multiplied by a factor of 0.48 (the daytime length divided by 24hrs) and a zenith angle of 52°(computed to get the right diurnally-averaged insolation for Oct. 16 at 20°S, 85°W). The albedo of the sea surface is fixed at 6% (Payne, 1986).

If the reference diabatic forcing Q_0^+ consists only of radiative cooling, a reference subsidence rate profile $w_{s0}(z)$ may be obtained from the steady-state free-tropospheric energy balance,

$$\mathbf{v} \cdot \nabla \theta_0 + w_{s0} \frac{\partial \theta_0}{\partial z} = Q_0^+. \tag{4.2}$$

In this equation, horizontal advection of free-tropospheric potential temperature θ_0 is

taken to be

$$-\mathbf{v} \cdot \nabla \theta_0 = \begin{cases} 0.36 \text{ K day}^{-1} \text{ above 3km} \\ (1 - \frac{z}{3000}) + \frac{0.36\,z}{3000} \text{ K day}^{-1} \text{ below 3 km.} \end{cases} \qquad (4.3)$$

This is an idealization of daily values averaged over Sept-Dec 1998-2001 (the season of peak Sc) from ECMWF 40 Year Re-Analysis (ERA-40, Uppala et al. 2005) at 20°S, 85°W.

The subsidence rate generated from (4.2) with Q_0^+ equal to the radiative cooling rate, however, does not obey the surface boundary condition $w_{s0}(0) = 0$. To correct for this, we add a BL turbulent heat flux convergence $\mathcal{T}(z)$ to Q_0^+ near the surface. We assume $\mathcal{T} = 0$ above 1.8km and choose $\mathcal{T}$ below this level so as to make w_{s0} decrease linearly to a surface value of zero. The depth of this correction layer was chosen to be just larger than the maximum equilibrium BL depth obtained in our experiments in order to optimize agreement with ERA-40 data.

4.2.2 Representation of BL Feedbacks on the Free Troposphere

The above approach neglects a subtle but important detail. The radiative flux profile used in (4.2) is based on thermodynamic profiles with no BL. Because the BL is much cooler than the overlying air, its presence enhances the radiative flux divergence just above cloud top. If this enhancement is neglected, the modeled inversion strength becomes too strong and the BL collapses. On the other hand, if all of the BL-induced radiative flux divergence is used to change the temperature profile, the inversion becomes too weak and cloud top becomes unreasonably high. This issue is illustrated in Fig. 4.4, which compares the EPIC observed potential temperature profile (normalized by inversion height then averaged over all 6 days of data) with a model profile where BL effects are ignored and with another profile where all BL-induced radiative enhancement is assumed to reduce the temperature of the subsiding air. The model profiles are based on a well-mixed BL with cloud base, cloud top, and SST matching the 6-day mean EPIC data and with a virtual moist adiabatic free-tropospheric θ_0 with SST$_{\text{ITCZ}}$ = 302K. Clearly neither of these approaches is able to capture the observed temperature trend. This
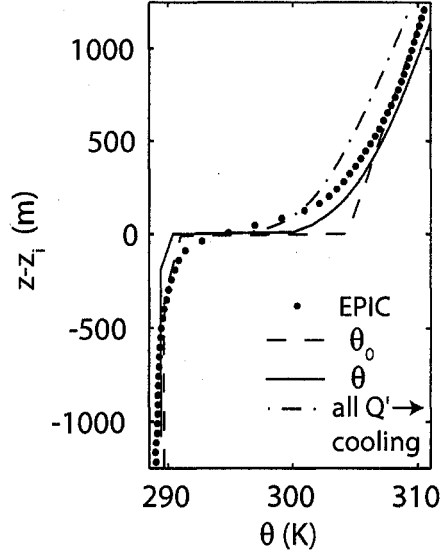
Figure 4.4: Potential temperature profiles from EPIC observations (composite of 48 soundings normalized by cloud top), from the model without applying a BL radiative correction (θ_0), from the model as implemented (θ), and from assuming that all BL-induced radiative enhancement acts directly on the temperature profile.

section is devoted to improving model-observation agreement, and ultimately yields the better-agreeing solid line in Fig. 4.4.

A related problem is seen in Fig. 4.5. The reference subsidence profile $w_{s0}(z)$ is too weak compared to ERA-40. This disagreement suggests that the increased subsidence warming required to balance the BL-induced radiative flux divergence in the free-tropospheric energy balance is achieved through a combination of increased cooling near cloud top and strengthened w_s.

Clearly, some modification to (4.2) is required in order to adequately represent the temperature and subsidence profiles that develop in the vicinity of the inversion in response to the departure $Q'(p, t)$ of the diabatic heating from the reference heating profile $Q_0^+(p)$. We explored several possibilities for how to do this. Each method yields a different model prediction for the current climate, but reassuringly all show the same response to changing SST. We settled on the method outlined below because we feel it best represents
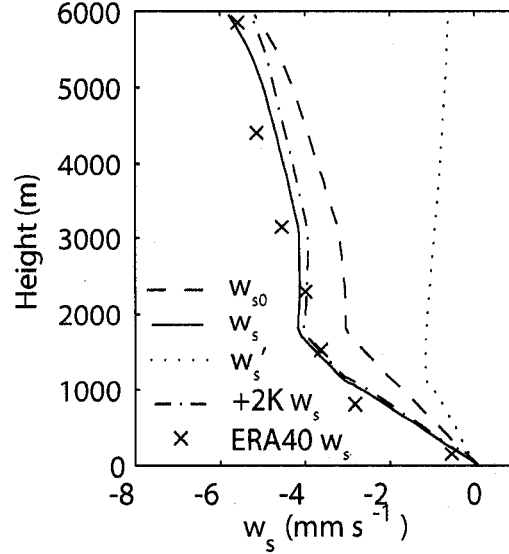
Figure 4.5: Comparison of subsidence profiles from ERA-40 data (averaged over Sept-Dec 1998-2001) at 20°S 85°W) with modeled subsidence rate neglecting (w_{s0}) and including (w_s) BL-induced radiative flux enhancement. This plot also includes the enhancement w'_s to the subsidence rate induced by the BL and the modeled subsidence rate for a +2 K perturbation in SST_{ITCZ} and SST_{Sc}.

the underlying physics given the constraints of a single column approach.

Our strategy is to estimate the linear response of vertical velocity and temperature to $Q'(p,t)$ by assuming this diabatic heating perturbation is horizontally localized over the stratocumulus region. The resulting horizontal heating and buoyancy gradients will affect the vertical motion and temperature profiles via stratified adjustment in a manner analogous to the tropical response to deep convection. We use the simplest theoretical framework that encapsulates this process, adjusting the one free parameter that emerges from this framework to best match observed SE Pacific temperature and subsidence rate profiles above the Sc layer.

We start by assuming the tropical perturbation diabatic heating $Q^*(x,p,t)$ varies sinusoidally with horizontal position x, diminishing to zero at a distance Λ from the Sc

column (positioned at $x = 0$:

$$Q^*(x,p,t) = Q'(p,t)\cos(\pi x/2\Lambda), \; 0 < x < \Lambda. \tag{4.4}$$

For simplicity, we assume that variations in perturbation heating and in the induced flow are confined to the x direction and are constant in the transverse (y) direction. The reference state is treated as horizontally homogeneous, reflecting the quasi-uniform free-tropospheric radiation-advection heat balance that dominates over the subsidence regions of the Tropics. The mass required to balance the reference-state subsidence rate $\omega_0(p)$ is assumed to be supplied by mean reference state horizontal divergence in the y direction (perpendicular to the heating gradients). This divergence does not produce any horizontal advection of flow perturbations, which depend only on x.

In the following description, as in (4.4), reference profiles are subscripted with '0', and perturbations from these reference profiles are superscripted with an asterisk (if they contain x dependence) or primed (if they represent the vertical structure over the Sc column at $x = 0$). For consistency with the BL parameterization which is phrased in terms of liquid water potential temperature θ_l (Betts, 1973), we use θ_l as an approximation to the virtual potential temperature in this analysis. Neglecting virtual effects is reasonable since humidity is very low through almost the entire tropospheric depth in subtropical Sc regions. Since $\theta_l = \theta$ in the absence of liquid water, θ_0 is an appropriate measure of θ_l in our cloud-free reference profile.

To simplify the algebra, we use pressure coordinates for the remainder of this section. We translate our results to height coordinates for use in the MLM via the hydrostatic relation (1.1).

We assume hydrostatic f-plane dynamics linearized about the reference state in a layer between pressures $p = p_s$ (surface) and $p = p_T$ (tropopause), where $\omega = 0$. The only linearized advection term is due to mean subsidence. As noted above, there is no effect of perturbations on the assumed mean horizontal heat and moisture advection. The

perturbation equations of motion then reduce to:

$$\frac{D_l u^*}{Dt} - f v^* = -\frac{\partial \phi^*}{\partial x}, \tag{4.5}$$

$$\frac{D_l v^*}{Dt} + f u^* = 0, \tag{4.6}$$

$$\frac{\partial \phi^*}{\partial p} = -R_d \Pi \frac{\theta_l^*}{p}, \tag{4.7}$$

$$\frac{\partial u^*}{\partial x} + \frac{\partial \omega^*}{\partial p} = 0, \tag{4.8}$$

$$\frac{D_l \theta_l^*}{Dt} - S_0 \omega^* = Q^*. \tag{4.9}$$

In the above equations, $D_l/Dt = \partial/\partial t + \omega_0(p)\partial/\partial p$ is the linearized material derivative, u^* and v^* are the east-west and north-south wind perturbations respectively, ϕ^* is the geopotential perturbation, R_d is the gas constant for dry air, $\Pi = (p/p_s)^{R_d/c_p}$ is the Exner function, f is the coriolis parameter, and $S_0 = -\partial\theta_0/\partial p$. All variables in (4.5) - (4.9) are assumed independent of y. Note that D_l/Dt commutes with x and t-derivatives but not p-derivatives.

We cross-differentiate (4.5) and (4.6) to eliminate v^* in favor of u^*, take a further x-derivative to phrase the equation in terms of $\partial u^*/\partial x$, and use mass continuity (4.8) to eliminate $\partial u^*/\partial x$ in favor of ω^*:

$$\left(\frac{D_l^2}{Dt^2} + f^2\right)\frac{\partial \omega^*}{\partial p} = \frac{\partial^2}{\partial x^2}\frac{D_l \phi^*}{Dt}. \tag{4.10}$$

We aim to integrate (4.10) to steady-state, so we can reasonably assume $\partial/\partial t \ll f$. The following scale analysis suggests that we can similarly neglect $\omega_0 \partial\omega^*/\partial p$ compared to $f\omega^*$. For troposphere-deep ω perturbations, the inverse subsidence timescale $\omega_0\partial/\partial p$ can be estimated assuming a 400 hPa deep gradient layer for ω^* and taking a typical value $\omega_0 \approx 0.04$ Pa s^{-1}. This gives an inverse subsidence timescale 0.04 Pa s^{-1}/400 hPa $=$ 10^{-6}s^{-1}, which is much smaller than subtropical values of f, which are on the order of

10^{-5}s^{-1}. Thus, we neglect D_l/Dt compared to f in (4.10) to obtain

$$f^2\frac{\partial\omega^*}{\partial p} \approx \frac{\partial^2}{\partial x^2}\frac{D_l\phi^*}{Dt}.$$ (4.11)

Next, we take the p-derivative of (4.11) and substitute hydrostatic balance (4.7) to eliminate ϕ^* in favor of θ_l^*:

$$-\frac{f^2 p}{R_d\Pi}\frac{\partial^2\omega^*}{\partial p^2} = \frac{\partial^2}{\partial x^2}\left[\frac{D_l}{Dt} - \left(1 - \frac{R_d}{c_p}\right)\frac{\omega_0}{p} + \frac{d\omega_0}{dp}\right]\theta_l^*.$$ (4.12)

Equation (4.12), together with the heat equation (4.9), constitute a closed set of equations for $\omega^*(x, z, t)$ and $\theta_l^*(x, z, t)$.

We seek a separable solution of the same form as the heating perturbation Q^*,

$$\begin{bmatrix}\theta_l^* \\ \omega^*\end{bmatrix}(x, p, t) = \begin{bmatrix}\theta_l' \\ \omega'\end{bmatrix}(p, t)\cos(\pi x/2\Lambda),$$ (4.13)

We substitute these forms into (4.12) and evaluate at $x = 0$. We will use a posteriori scale analysis to neglect $-(1 - R_d/c_p)\,\omega_0/p + d\omega_0/dp$ in (4.12). Assuming for now that this is valid, we obtain

$$\frac{D_l\theta_l'}{Dt} = \frac{4\Lambda^2 f^2 p}{\pi^2 R_d\Pi}\frac{\partial^2\omega'}{\partial p^2}.$$ (4.14)

We then substitute into (4.9) to obtain a single equation for ω':

$$\left(-P_0^2\frac{\partial^2}{\partial p^2} + 1\right)\omega' = -H'(p, t)$$ (4.15)

where $H' = Q'/S_0$ and $P_0(p) = (4f^2\Lambda^2 p/\pi^2 R_d\Pi S_0)^{1/2}$. We can interpret P_0 as a Rossby adjustment pressure-depth for the horizontal scale Λ. In the limit $P_0 \to \infty$, $\omega' \to 0$ and our scheme reduces to (4.2). In the 'weak temperature gradient' limit $P_0 \to 0$, stratified adjustment efficiently suppresses temperature perturbations, and the diabatic heating perturbations are entirely balanced by changes in subsidence. For finite P_0, heating perturbations with vertical scales less than P_0 will mainly induce local temperature

perturbations,while those on larger vertical scales will mainly induce ω perturbations.

In practice, the best choice for P_0 is uncertain. One reason for this is that the Sc regions are geographically distributed, so there are no single correct values of λ and f. After some experimentation, we chose a constant value of $P_0 = 300\text{hPa}$ in our model to produce a realistic subsidence rate at 1km (the typical BL inversion height) when applied with current-day forcings. Such a value of P_0 may be obtained by taking $f = 4 \times 10^{-5}$ s^{-1} (corresponding to a mean latitude of 15°, intermediate between the ITCZ and the main subsidence regions), $\Lambda = 1650$ km, and $S_0 = 0.04$ K hPa^{-1} at $p = 500$ hPa.

In our derivation we assumed that $-\left(1 - R_d/c_p\right)\omega_0/p + d\omega_0/dp \ll D_l\theta_l'/dp$ This can now be seen to be justifiable if P_0 is smaller than the tropospheric depth. By the above equation and arguments, the dominant vertical half-wavelength of θ_l' perturbations will be P_0 or less, while the half-wavelength of $\omega_0(p)$ variations is the tropospheric pressure depth Δp_T. Thus the ratio of the scales of $\left(1 - R_d/c_p\right)\omega_0/p$ and $(d\omega_0/dp)\theta_l'$ to $D_l\theta_l'/dp$ will be $P_0/\Delta p_T$. Our neglect of the former terms is justified if this ratio is much less than one, which is marginally satisfied with our parameter choices.

The total diabatic heating for the Sc column is given by

$$Q'(p,t) + Q_0(p) = -\frac{\partial F_{\theta_l}}{\partial z} + \frac{L}{c_p}\left[\frac{\partial F_P}{\partial z} + \frac{\partial F_{\text{sed}}}{\partial z}\right] - \frac{1}{\rho c_p}\frac{\partial F_R}{\partial z}, \qquad (4.16)$$

where F_R, F_P, F_{sed}, and F_{θ_l} are the radiative, precipitation, sedimentation, and turbulent θ_l fluxes (positive upward and in W m^{-2}, mm s^{-1}, mm s^{-1}, and K m s^{-1} respectively). The reference, perturbation, and net diabatic heating profiles are included in Fig. 4.6. The reference profile Q_0 consists of radiative cooling above 1.8km, but includes an increasingly positive $\mathcal{T}$ component near the surface as required to balance (4.2) by offsetting the low level advective cooling. Q is dominated by a large cooling spike at cloud top caused by removal of warm air just above the inversion by entrainment and enhanced by strong radiative cooling in the air just below cloud top. Lower in the cloud Q is positive due mainly to radiative absorption. There is weak warming below cloud base due to sensible heating from the warmer underlying ocean.

Given the incremental diabatic heating $Q'(p)$ induced by the Sc-topped BL and the
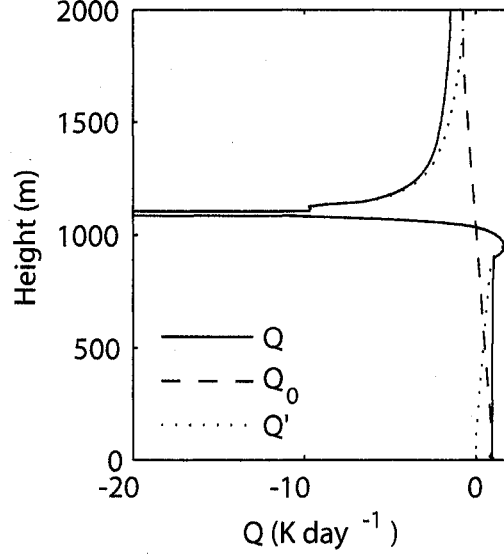
Figure 4.6: Reference, perturbation, and total diabatic heating profiles from the current-condition steady-state model solution.

boundary conditions $\omega'(p_s) = 0$ and $\omega'(p_T) = 0$, (4.15) may be solved numerically for $\omega'(p)$ using a tridiagonal solver. Once ω' has been calculated, the total pressure-subsidence rate $\omega = \omega_0 + \omega'$ is generated, then converted to w_s via the hydrostatic relation (1.1). As shown in Fig. 4.5, w_s now agrees well with ERA-40 in the vicinity of cloud top (around 1km).

Also included in this figure is the w_s profile for a $+2$ K SST perturbation. This profile displays the 'subsidence rate feedback', where lapse rate increases faster than Q as $\mathrm{SST_{ITCZ}}$ rises, necessitating a decrease in subsidence to maintain energy balance. The weakening of the tropical overturning circulation implied by this decrease is a common feature of simple tropical models and has also been documented in general circulation models, reanalysis data, and observations (Knutson and Manabe, 1995; Held and Soden, 2006; Zhang and Soon, 2006; Vecchi et al., 2006).

Using as forcings the total diabatic heating, the vertical advection with corrected w_s, and the horizontal advection, the physically consistent θ_l is prognosed from a time-space

discretization of

$$\frac{\partial \theta_l}{\partial t} = -\mathbf{v} \cdot \nabla \theta - w_s \frac{\partial \theta_l}{\partial z} + Q. \tag{4.17}$$

and integrated to steady-state concurrently with the MLM.

A problem unique to the MLM is how to deal with radiative cooling near the inversion. Since the MLM assumes an infinitely thin inversion layer, radiative cooling is exaggerated just above cloud top. Numerically resolving such an inversion introduces a resolution sensitivity because of the strong discontinuity in radiative cooling across cloud top. To sidestep these difficulties, we simply prescribe the radiative flux divergence in the 50 m layer overlying cloud top. We have found that 6 W m^{-2}, partitioned evenly across the layer, produces reasonable BL depths for the current climate. This simplification is clearly apparent as a 50 m deep region of constant Q just above cloud top in Fig. 4.6. The details of how this cooling is distributed are relatively unimportant since the second derivative in (4.15) smears out the forcing. The θ profile obtained using this method is included in Fig. 4.4. This profile fits the observations much better than either of the previously mentioned options. Model performance is actually likely to be even better than Fig. 4.4 suggests because, as shown in Chapter 2, the EPIC θ profiles have a cold bias just above cloud top.

4.2.3 Sc-topped BL Model

The MLM is based on prognostic equations for q_t and θ_l (both taken to be uniform throughout the BL) and cloud top z_i (assumed coincident with the inversion base). These equations are similar to the moisture, energy, and mass budgets (2.1)-(2.3) of Chapter 2, but are based on geometric height and use θ_l instead of s_l ($s_l \approx c_p \theta_l$). Since these prognostic equations form the backbone of our current analysis, we include them below even though they could be derived from the earlier budget equations:

$$z_i \left(\frac{\partial q_t}{\partial t} + \mathbf{v} \cdot \nabla q_t \right) = \eta \left[q_s(\text{SST}_{\text{Sc}}, p_{\text{surf}}) - q_t \right] + w_e \left[q^+ - q_t \right] + \frac{F_P(0)}{\rho}, \tag{4.18}$$

$$z_i \left(\frac{\partial \theta_l}{\partial t} + \mathbf{v} \cdot \nabla \theta_l \right) = \eta \left[\text{SST}_{\text{Sc}} - \theta_l \right] + w_e \left[\theta_l^+ - \theta_l \right] + \Delta R_{\text{BL}} - \frac{L}{\rho c_p} F_P(0), \tag{4.19}$$

and

$$\frac{\partial z_i}{\partial t} + \mathbf{v} \cdot \nabla z_i = w_e + w_s(z_i). \tag{4.20}$$

In these equations, q^+ and θ_l^+ are the mixing ratio and liquid water potential temperature just above cloud top, and $\Delta R_{\mathrm{BL}} = -\int_0^{z_i} (\rho c_p)^{-1} \partial F_R / \partial z\, dz$ is the net radiative cooling in the BL. The surface sensible and latent heat fluxes are parameterized using the bulk formulation with bulk transfer coefficient η computed as $\eta = c_T ||\mathbf{v}_{\mathrm{surf}}||$ with $c_T = 0.001$ and surface wind speed $||\mathbf{v}_{\mathrm{surf}}||$ fixed at 6.2 m s^{-1} to match the climatological ocean heat transport at 20°S, 85°W. This value is lower than observed during EPIC ($\sim$7 m s^{-1}); this decrease is used to compensate the overestimation of surface fluxes due to neglect of the BL temperature and moisture stratification and to adjust the cloud thickness to match the diurnally-averaged net surface radiation balance. Although surface wind speeds may change in a changing climate, we ignore this effect in the present paper because it is unclear how to tie surface wind speed to the difference between local and ITCZ SST. Horizontal advection of BL temperature and moisture were taken to be 1.0 K day^{-1} and 1.3 g kg^{-1} day^{-1} respectively. An alternative approach, making advection proportional to the difference in SST between the ITCZ and the Sc regions, had an insignificant effect on the solutions. Pressure in the BL is computed consistently by integrating the free-tropospheric pressure downwards. Advection of z_i is taken to be 42 m day^{-1}, a value diagnosed from a SE Pacific satellite-derived cloud-top climatology for Oct-Nov 2004 as discussed in Wood and Bretherton (2004).

The precipitation flux incorporates contributions from cloud droplet sedimentation and drizzle. The sedimentation flux is calculated following Bretherton et al. (2007) by assuming a log-normal size distribution (with geometric standard deviation $\sigma_g = 1.2$) and Stokes' regime fall speed. The drizzle flux follows the recommendation of Wood (2006, pers. comm.),

$$F_p(z) = \begin{cases} \exp\left\{-k\left(\frac{z_b-z}{\bar{r}^{2.5}}\right)^{1.5}\right\} F_p(z_b) & : \quad z < z_b \\ \left[1 - \left(\frac{z}{z_i - z_b}\right)^3\right] F_p(z_b) & : \quad z_b < z < z_i \end{cases} \tag{4.21}$$

with

$$F_p(z_b) = -4.3 \times 10^{-6} \left(\frac{\text{LWP}}{N_d}\right)^{1.75}.$$
(4.22)

This combines the parameterization of Comstock et al. (2004) at and below cloud with a simple fit to the data from Fig. 6d of Wood (2005) within cloud. In these equations, $\bar{r} = 60\mu$m is the mean radius of the truncated exponential distribution at cloud base and $k = 320\mu$m$^{3.75}$ m$^{-1.5}$. The liquid water path (LWP), droplet concentration N_d, and F_p are assumed to have units of g m^{-2}, cm^{-3}, and mm s^{-1}, respectively. In the control simulation, N_d is fixed at 100 cm^{-3} (which matches the estimated mean value from the EPIC data set).

Entrainment is deduced in the control simulation following Turton and Nicholls (1987) (hereafter TN) as modified in Bretherton et al. (2007) to account for sedimentation effects. We compared the MLM entrainment with recent GEWEX Cloud System Study single-column model intercomparisons of a nonprecipitating and heavily precipitating nocturnal Sc-topped BL as described by Zhu et al. (2005) and Wyant et al. (2007), respectively, as well as with Caldwell et al.'s (2005) observational study of the diurnal cycle of entrainment and turbulence in the SE Pacific Sc. We found the MLM was underentraining, prompting us to adopt $a_2 = 30$ and $a_{\text{sed}} = 4$, which gives much better agreement with the entrainment rates found in the above studies. The entrainment parameterization depends on the BL-integrated buoyancy flux, which is computed using the mixed-layer assumptions and the radiation and precipitation profiles as described in Chapter 2. Sensitivity to the use of a different entrainment closure is explored in Section 4.3.3.

4.2.4 Model Runs

For each pair of (SST$_{\text{Sc}}$,SST$_{\text{ITCZ}}$) with SST$_{\text{Sc}} \in \{289, 290, 291, 292, 293, 294, 295\}$ and SST$_{\text{ITCZ}} \in \{299, 300, 301, 302, 303, 304, 305\}$, equilibrium solutions are obtained by running the model for 80 days and checking visually for convergence. This creates a 7×7 array of equilibrium states for each model output. These arrays are contour plotted and analyzed in the next section.

Table 4.1: Comparison of "current condition" ($SST_{Sc} = 292K$, $SST_{ITCZ} = 302K$) model output for $1\times$ and $2\times CO_2$ with z_i, z_b observations from EPIC radiosondes and climatological surface flux observations from the WHOI buoy.

Units	z_b m	z_i m	SHF W m^{-2}	LHF W m^{-2}	H_{ocn} W m^{-2}
Obs.	920	1270	8	108	38
ctrl	899	1085	12	112	37
$2\times CO_2$	867	1005	12	109	46

4.3 Numerical Model Results

In Table 4.1, the model's prediction of the current climate ($SST_{Sc} = 292K$, $SST_{ITCZ} = 302K$) is compared with observations. The observed cloud base and cloud top are taken from the EPIC campaign; values from PACS campaigns are similar. Surface fluxes are annually-averaged values taken from the Woods Hole Oceanographic Institute (WHOI) buoy at $20°S$, $85°W$ (Kolbo and Weller, 2004 personal communication). In this table, H_{ocn} is the heat export out of the ocean mixed layer in the Sc region,

$$H_{ocn} = -SHF - LHF - F_R(0), \tag{4.23}$$

where SHF and LHF are the sensible and latent heat fluxes, respectively, and all radiation is assumed to be absorbed in the ocean mixed layer. Overall, the agreement is quite good given the simplicity of our model. Since we neglect the observed Sc thinning during the day, the modeled cloud thickness and LWP must be much smaller than the observed daily mean in order to match the observed diurnally-averaged shortwave radiation at the surface as required to obtain a reasonable H_{ocn}. Since drizzle is proportional to LWP in our model (through (4.22)), this results in an underestimate of precipitation. Sensitivity studies with higher precipitation rates (Section 4.3.4) suggest that this underestimate does not significantly affect our conclusions.

This table also includes results from a run with current climate SSTs but doubled CO_2. Results from this run are similar to those of the control simulation, though the
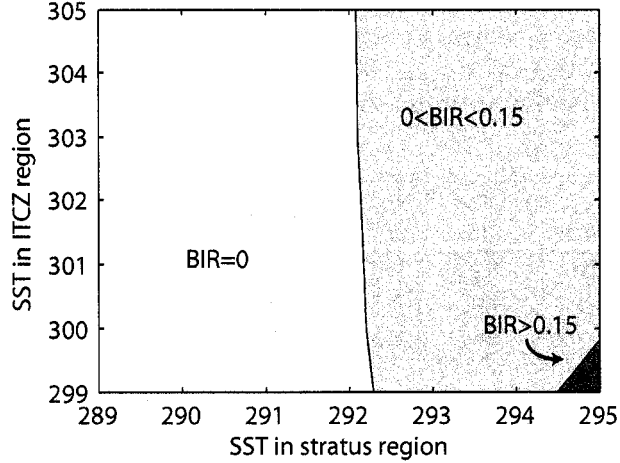
Figure 4.7: Contour plot of BIR for each of the SST pairs considered in the model.

added infrared opacity of the atmosphere slightly reduces BL radiative cooling (from 36.7 W m^{-2} to 35.7 W m^{-2}) which decreases entrainment, resulting in slightly thinner cloud with lower z_b and z_i and higher q_t. This results in more sunlight reaching the ocean and reduced ocean heat loss by latent heat fluxes, enhancing H_{ocn} by 9 W m^{-2}.

An estimate of the suitability of the mixed layer approximation for each SST pair may be obtained by considering the buoyancy integral ratio (BIR)

$$\text{BIR} = \frac{\int_0^{z_i} \overline{w'b'}\mathcal{H}(-\overline{w'b'})dz}{\int_0^{z_i} \overline{w'b'}\mathcal{H}(\overline{w'b'})dz} \qquad (4.24)$$

where $\overline{w'b'}$ is the buoyancy flux and $\mathcal{H}$ is the Heaviside function. This quantity measures the fraction of buoyancy production of turbulent kinetic energy generation depleted by eddies pushing negatively-buoyant air upward and positively-buoyant air downward. Bretherton and Wyant (1997) suggest on the basis of observations and large-eddy simulations that the mixed-layer approach remains tenable for BIR<0.15, while Stevens (2000) suggests on the basis of large-eddy simulations that some decoupling occurs for any BIR>0. Figure 4.7 shows the regions of our domain satisfying each of these criteria. By any measure the MLM is appropriate over much of the domain, and using the

Bretherton-Wyant cut-off the model is tenable for all but the very weakest inversions.

Steady-state values of various output fields for all SST combinations are plotted in Fig. 4.8. For a given SST_{ITCZ}, this figure shows the BL response to local (e.g. geographic) variations. As SST_{Sc} rises, cloud base and top both rise due to increased entrainment through a weaker inversion. In the MLM this results in a thicker cloud layer with higher LWP. By looking at how the outputs change as both SSTs are varied, a sense of the model response to a changing climate may be obtained, though the direct radiative effect of changing CO_2 is not included. Table 4.1 suggests this effect is secondary but not negligible. For some variables (such as q_t), simply assuming that global warming will cause both SST_{Sc} and SST_{ITCZ} to increase is enough to get a sense of the model response (e.g. q_t should increase). For outputs which show one response to increasing SST_{Sc} but do the opposite for increasing SST_{ITCZ} however, the climate response depends strongly on how SST_{ITCZ} changes in proportion to SST_{Sc}. This relationship between SSTs determines a path through the (SST_{Sc}, SST_{ITCZ}) parameter space which can be depicted as a curve on the contour plots of Fig. 4.8. Two scenarios discussed below are presented as thick lines on these plots.

4.3.1 Geographically-Uniform SST Increase

Cess et al. (1989) assessed cloud feedbacks on climate sensitivity by assuming a globally-uniform warming of SST, corresponding to the dashed line $dSST_{ITCZ}/dSST_{Sc} = 1$ in Fig. 4.8. Along this line, cloud top increases much more rapidly than cloud base as the climate warms and LWP rises rapidly.

As pointed out in Somerville and Remer (1984), even if cloud thickness remains the same, some increase in LWP is expected at warmer temperatures because $\partial q_l/\partial z$ increases with T. Although Somerville and Remer argue from observational data, this relation may be shown mathematically for the case of a well-mixed Sc-topped BL by noting that a cloud with fixed boundaries will contain more liquid if $\partial q_l/\partial z$ increases. Since $q_l = q_t - q_s$ is a

96
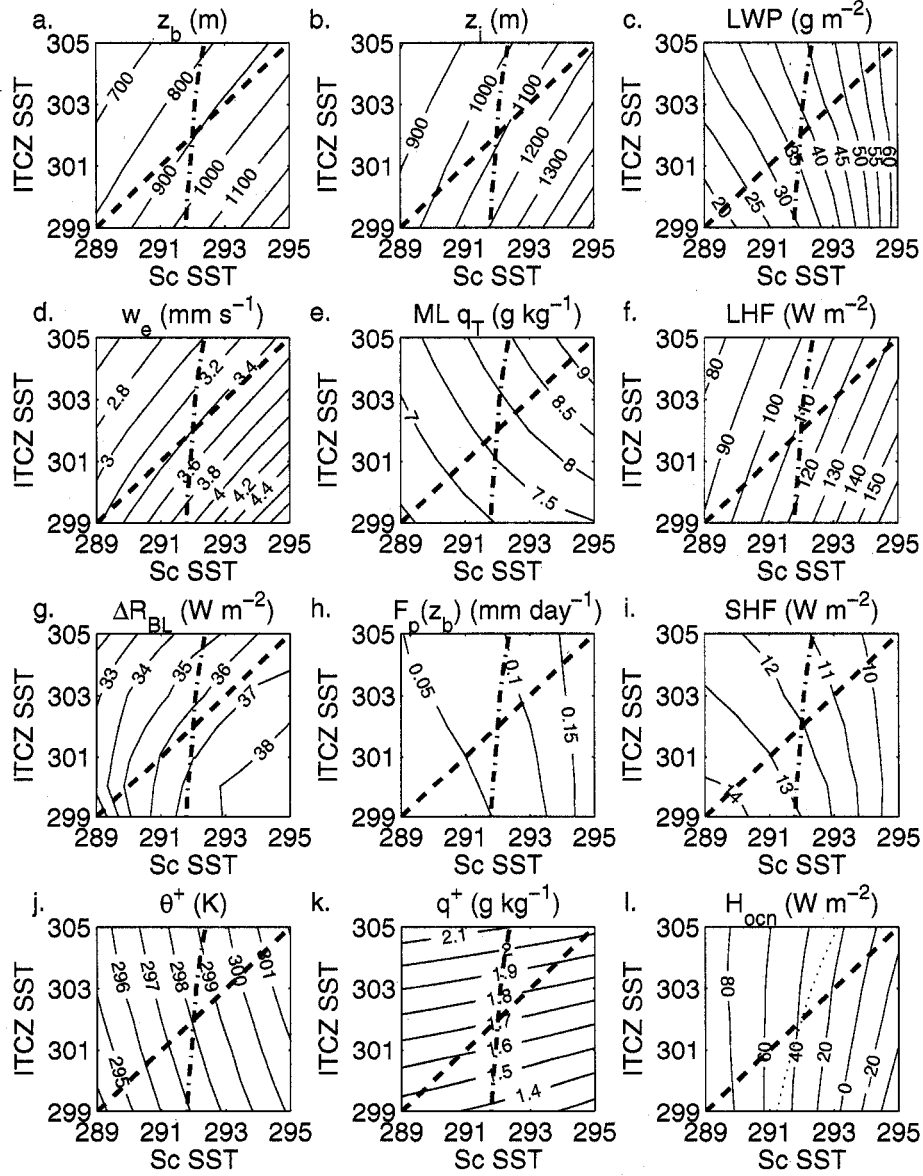
Figure 4.8: Results of control MLM runs. In each subplot, the solid contour denotes the quantity given in the title, the dashed line represents equal warming in both the Sc and the ITCZ regions and the dot-dashed line indicates the path where the surface energy budget is balanced, assuming oceanic heat transport remains constant. The dotted line in panel l shows the approximate path for surface energy balance including the direct CO_2 contribution.

smooth function in the cloud interior and $\partial q_t/\partial z = 0$ for well-mixed conditions,

$$\frac{\partial}{\partial T}\left(\frac{\partial q_l}{\partial z}\right) = -\frac{\partial}{\partial z}\left(\frac{\partial q_s}{\partial T}\right) \tag{4.25}$$

$$= -\frac{L}{R_v}\frac{\partial}{\partial z}\left(\frac{q_s}{T^2}\right) \tag{4.26}$$

$$= \frac{-Lq_s}{R_v T^2}\left(\frac{\partial \ln q_s}{\partial z} - 2\frac{\partial \ln T}{\partial z}\right) \tag{4.27}$$

where the second line follows from Clausius-Clapeyron, the third line uses the chain rule, and R_v is the gas constant for water vapor. Since q_s decreases by a factor of two over the lowest 1km while T only decreases by about 3%, this last line is strongly positive and LWP increases with T. In our model, we find over 90% of the change in LWP to be due to change in cloud thickness, with the Somerville-Remer mechanism explaining the remainder. Thus changes in $\partial q_l/\partial z$ make a small but non-negligible contribution to LWP feedback under the Cess framework.

It is also interesting to compare Sc cloud feedback in our model with the feedback predicted by arguments based on LTS. As mentioned in section 4.1, LTS increases with uniform SST rise due to the lapse rate feedback, resulting in a negative Sc feedback in models including this effect. Our model also exhibits a negative Sc feedback with uniform SST rise, which suggests that LTS effects may be playing a role. When SST_{ITCZ} is fixed, however, our model predicts an increase in LWP and hence albedo even though LTS decreases. Thus LTS is generally not a skillful predictor of MLM-predicted cloud albedo across the entire spectrum of Sc and ITCZ SSTs. This disagreement is perhaps unsurprising since LTS is generally correlated with cloud fraction, which is constrained to be zero or one in the MLM. Thus a more sophisticated Sc-topped BL model would be required to rigorously test the connection between LTS and albedo.

4.3.2 SST Increase at Constant H_{ocn}

Another possible path through the SST space is obtained by assuming that H_{ocn} remains invariant under climate change (dot-dashed line). This is the assumption tacitly made in

most previous simple tropical atmospheric models (Miller, 1997; Larson et al., 1999) and is also commonly used in GCM climate sensitivity studies using 'slab oceans' (e.g. Kiehl et al. 2006). In this case, we can determine $d\text{SST}_{\text{ITCZ}}/d\text{SST}_{\text{Sc}}$ from (4.23).

The MLM-implied heat flux into the ocean is shown in Fig. 4.8l. This quantity decreases strongly as LHF rises or LWP increases (which decreases the amount of sunlight transmitted to the ocean surface). In order to maintain a balanced surface energy budget, SST_{Sc} must adjust such that the decrease in net downward radiative flux is balanced by a corresponding decrease in the turbulent energy flux out of the ocean surface. In order to accomplish this, SST_{Sc} rises little as SST_{ITCZ} increases, z_b and z_i decrease, and LWP increases much less rapidly than in the Cess scenario. Surface shading and surface latent heating act as negative feedbacks on LWP by cooling Sc region SST relative to SST_{ITCZ}. This increases inversion strength, causing w_e to decrease and hence lowering z_b and z_i, and limiting LWP growth. As in the Cess case, the cloud thickness contribution to LWP increase is much larger than that from change in $\partial q_l/\partial z$, which accounts for only a tenth of the LWP increase along the energy balance line.

It is interesting to note that previous 2-box models have also shown an increase in SST difference between the ITCZ and Sc regions, but for a different reason (in fact, previous models have mostly used fixed cloud properties). In these models, the subsidence rate is diagnosed much the same way as in the current study, so the tropical circulation slows as the climate warms. This results in decreased heat export from the ITCZ, causing it to warm faster than the Sc region. The fact that an increase in SST difference can be justified on the basis of both local and large scale considerations suggests that this may be a robust response to warming. The 2-box model of Larson et al. (1999) also predicts the decrease in cloud base and cloud top that we see in our model. In their model these decreases occur due to reduced BL radiative cooling as water vapor builds up in the free troposphere, increasing infrared opacity. This mechanism is also seen in Fig. 4.8g to play a role in our model, since ΔR_{BL} decreases with increasing SST along the energy balance line. Additionally, z_i in our model is decreased by increased free-tropospheric relative humidity through a reduction in evaporative entrainment enhancement as well

as directly through an increase in inversion strength as the cold- and warm-pool SST difference grows. Since our ΔR_{BL} change is relatively small in proportion to our z_i change, it is likely that these latter effects are playing a substantial role in our simulations.

We should also consider the direct radiative effect of changed CO_2 on the oceanic energy balance, which the above argument neglects. If we assume a typical tropical climate sensitivity of 2 K SST_{ITCZ} increase for CO_2 doubling, Table 4.1 suggests that we should add 9 W m^{-2} to H_{ocn} per 2 K increase in SST_{ITCZ}. To keep H_{ocn} at current levels requires a slightly different path through Fig. 4.8 with $dH_{ocn}/dSST_{Sc}$ decreasing by 9 W m^{-2} for each 2 K of SST_{ITCZ} increase. This path is included as a dotted line in Fig. 4.8l, which shows that the direct effect of CO_2 adds an additional increase of about 1 K in SST_{Sc} for each 4 K increase in SST_{ITCZ}.

4.3.3 Sensitivity to Entrainment

A crucial but still quite uncertain ingredient of a MLM is its entrainment closure. Although the broad behavior of a MLM as SST_{Sc} is warmed relative to SST_{ITCZ} is not highly sensitive to the entrainment closure (Bretherton and Wyant, 1997), different closures lead to marked differences between steady-state LWP (Stevens, 2002). Additionally, different parameterizations yield differing estimates of BIR, which affects the domain of applicability of the MLM. Thus we tested the response of our MLM to use of a fundamentally different closure due to Lewellen and Lewellen (1998) (hereafter LL). As described in section 2.4.4, the TN closure relates entrainment to a convective velocity diagnosed from the buoyancy flux profile, the inversion density jump, and an entrainment efficiency that increases linearly with cloud top liquid water. The LL closure, on the other hand, calculates an entrainment rate sufficient to reduce the convective velocity by a specified fraction. BIR for this simulation (not shown) is zero for all SST, suggesting a wider range of applicability. Fig. 4.9b, which shows z_b, z_i, and LWP fields from our model when entrainment is diagnosed following LL, is surprisingly similar to the control simulation (Fig. 4.9a). The NT entrainment rate is increasingly larger than that for LL at higher z_i (up to a maximum difference of 0.44 mm s^{-1} for the deepest BLs). This results in slightly lower
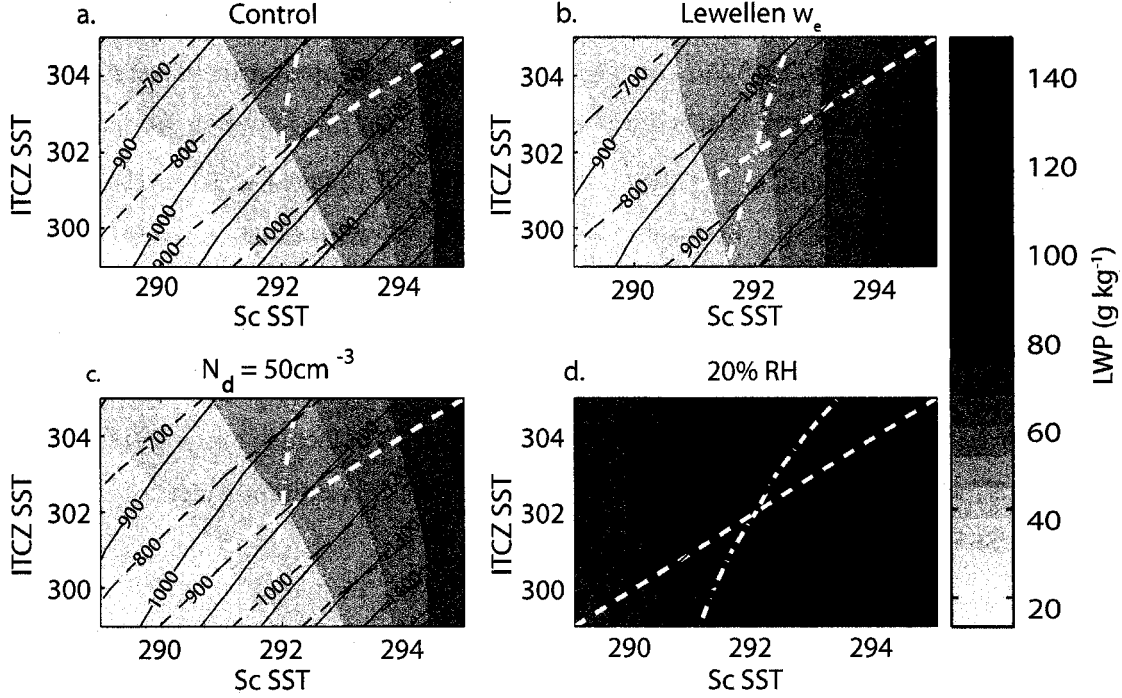
Figure 4.9: Cloud top (in m, solid black line), cloud base (in m, dashed black line), and LWP (shading, in g m^{-2}) for the control run and various sensitivity studies. The dashed white line represents equal cooling in both the Sc and the ITCZ regions. The dot-dashed white line indicates the path where the surface energy budget is balanced, assuming that oceanic heat transport remains constant. Regions of zero cloud thickness are shaded black.

z_b and z_i values for the LL parameterization at higher z_i (with maximum discrepancies of 186m and 141m, respectively). These effects have canceling effects on LWP, which is generally higher (by less than 29 g m^{-2}) in the LL run, particularly at high z_i. In general, the agreement between the two entrainment closures is quite remarkable considering the wide range of conditions simulated by our model.

4.3.4 Sensitivity to Sedimentation and Drizzle

Another open question in the study of Sc is the effect of precipitation processes on LWP. Because surface precipitation rates are usually quite low in these clouds, drizzle has

little direct impact on the moisture and energy balances of the BL both in observations (Chapter 2 and in our MLM simulations across all considered SST combinations. On the other hand, evaporative cooling below cloud decreases buoyancy flux, decreasing the amount of energy available to drive entrainment (Bretherton and Wyant (1997) and Chapter 2). The importance of drizzle in this evaporative regime is proportional to the cloud-base drizzle rate $F_P(z_b)$, which is included in Fig. 4.8h for the control run. Additionally, sedimentation of cloud droplets near cloud top has recently been found to have an important effect on entrainment and LWP (Ackerman et al., 2004; Bretherton et al., 2007).

As noted in 4.3, our model has a significant bias towards low LWP and thus low drizzle rates. To test the importance of this bias, we perform another run with drizzle artificially enhanced by decreasing the droplet concentration N_d to 50 cm^{-3}. Results from this case are included in Fig. 4.9c. Note that (4.22) implies that a decrease in droplet concentration of 50% at fixed LWP causes cloud base drizzle to increase by a factor of more than three. Even with this large fractional increase in cloud base drizzle, LWP differs from the control simulation by less than 10% for all SST pairs, with LWP decreasing with increasing N_d for LWP < 30 g m^{-2} due to sedimentation-entrainment feedback (as suggested by Ackerman et al. 2004) and LWP increasing with N_d at larger LWP as drizzle plays a more significant role (Fig. 4.10).

Following Wood (2007b), we can assess the relative importance of the first and second indirect aerosol effects (described in section 1.5) by considering the optical depth τ. Boers and Mitchell (1994) derived a relationship between τ, N_d, and cloud depth under the assumption of an adiabatic cloud layer. Noting that LWP $\propto (z_i - z_b)^2$ for such a cloud, this relation can be written $\tau \propto N_d^{1/3} LWP^{5/6}$. Thus for small perturbations,

$$\frac{\Delta\tau}{\tau} = \frac{1}{3}\frac{\Delta N_d}{N_d} + \frac{5}{6}\frac{\Delta LWP}{LWP} \qquad (4.28)$$

where the first indirect aerosol effect is contained in the first term on the right-hand side and the second indirect aerosol effect is is given by the second term. For our $\Delta N_d/N_d$ of 1/2, $\Delta LWP/LWP$ would have to be 1/5 for the second indirect aerosol effect to be
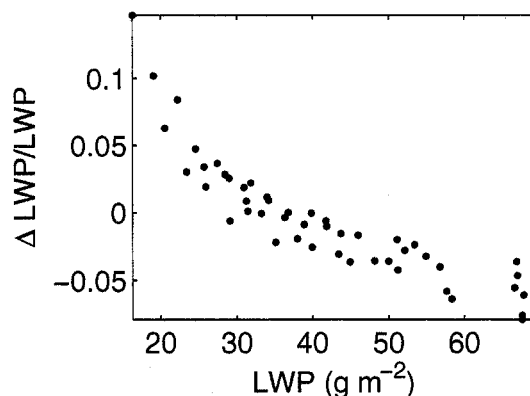
Figure 4.10: Scatterplot of the fractional change in LWP due to increasing droplet concentration from 50 cm^{-3} to 100 cm^{-3} for all SST pairs.

as important as the first. Since this quantity is generally less than 1/10 in Fig. 4.10, we conclude that the second indirect aerosol effect does not play an important role in our simulations. This contrasts with Pincus and Baker's (1994) study, which used a simpler entrainment closure and more idealized microphysics to conclude that the second indirect aerosol effect strongly reinforces the first, and also with the results of Wood (2007b), which supported Pincus and Baker (1994) for low z_b and found the second effect to oppose the first for larger z_b. Extensive comparison between our model and Wood's suggests that lower LWP in our model (required to get the correct diurnally-averaged surface insolation without simulating the diurnal cycle) is responsible for our decreased sensitivity.

4.3.5 Sensitivity to Free-Tropospheric Humidity

As a final sensitivity study, we examined the effect of varying the free-tropospheric RH from 10 to 20% (Fig. 4.9d). Increased moisture above z_i results in a lower cloud base, both because entrained air is relatively moister and because entrainment is decreased due to the weakening of cloud-top radiative cooling under an optically-thicker atmosphere. However, subsidence also decreases due to weakened free-tropospheric radiative cooling

at z_*, so cloud top height is actually slightly higher in this experiment. The increased z_i and decreased z_b go along with the large LWP increase (compared to the control) for all SST pairs seen in Fig. 4.9d. The dependence of LWP on SST is qualitatively similar to the control, increasing strongly with $\mathrm{SST_{Sc}}$ and showing a much weaker dependence on $\mathrm{SST_{ITCZ}}$.

4.4 Minimal Model

A major result of section 4.3 is that equilibrium LWP increases rapidly when $\mathrm{SST_{ITCZ}}$ and $\mathrm{SST_{Sc}}$ increase at equal rates, resulting in a strongly negative Sc cloud feedback. The goal of this section is to present a physical explanation for this behavior. We do this by simplifying our model to the point where we can analytically derive equilibrium solutions while still reproducing the basic features observed in the full model. The simplifications we make are as follows:

1. The BL is assumed in steady state and advection is neglected, so the left-hand sides of (4.18), (4.19) and (4.20) become zero.

2. The free-tropospheric θ_0 profile is linearized.

3. Free-tropospheric moisture is neglected since $q^+ \ll q_t$.

4. Drizzle is omitted.

5. Surface pressure is assumed equal to 1000 mb, so $\theta(0) = T(0)$.

6. We employ an "energy-balance" entrainment closure (Bretherton and Wyant, 1997), under which entrainment is diagnosed as the value needed to keep the surface air temperature equal to the local SST and hence set the subcloud thermal buoyancy flux equal to zero.

7. Fixed values are assumed for Q_0^+ and ΔR_{BL}. Fig. 4.8 shows this second quantity to vary by less than 20% across our control simulations.

Table 4.2: Values used for computation of simplest MLM solution.

	η	ΔR_{BL}	Q_0^+	z^*	Γ^+	β
Units:	mm s^{-1}	K m day^{-1}	K day^{-1}	m	K m^{-1}	m^{-1}
Val:	4.9	-2.9×10^3	-2.1	1800	$4.8 - 5.3 \times 10^{-3}$	$5.1 - 5.3 \times 10^{-4}$

8. Corrections to the free-tropospheric temperature and subsidence profiles due to near-BL radiative enhancement are neglected.

In the next 3 sections, these simplifications are used to derive expressions for entrainment rate, cloud base z_b, and cloud top. Section 4.4.4 explores the ramifications of these solutions.

4.4.1 Entrainment and Mean Subsidence

As in the full model, we assume that subsidence decreases linearly (i.e. divergence is constant) below a reference height of $z^* = 1.8$ km. Because w_{s0} captures the bulk of the subsidence rate in Fig. 4.5, we use the no-BL free-tropospheric energy budget (4.2) to diagnose $w_s(z^*)$, ignoring the BL-induced radiative cooling correction. Although cold advection plays a significant role in balancing this budget, its effect can be incorporated by increasing lower free-tropospheric Q_0^+ to about 2 K day^{-1}. Under these conditions, the cloud-top subsidence rate can be written

$$w_s(z_i) = \frac{Q_0^+ z_i}{\Gamma^+ z^*},$$

(4.29)

where $\Gamma^+ = \partial \theta_0^+ / \partial z \approx 5$ K km^{-1} for the SST$_{ITCZ}$ range considered here (Table 4.2).

Further, under steady-state conditions with negligible $\mathbf{v} \cdot \nabla z_i$, (4.20) reduces to

$$w_e = -w_s(z_i)$$

(4.30)

$$= \frac{|Q_0^+| z_i}{\Gamma^+ z^*}.$$

(4.31)

4.4.2 Cloud Base

By noting that RH= $q_t/q_s(T,p)$, making use of the Clausius-Clapeyron relationship, and assuming well-mixed conditions, an equation for the dry-adiabatic change in RH with height may be derived:

$$\frac{\partial \text{RH}}{\partial z} = \frac{g}{R_d T}\left(\frac{L R_d}{c_p R_v T} - 1\right)\text{RH}. \tag{4.32}$$

If T is approximated by a constant reference value $\tilde{T}$, this equation can be integrated from the surface to cloud base (where RH=1) and rearranged to give a very good approximation for z_b,

$$z_b = -\beta^{-1}\ln\left(\text{RH}(0)\right), \tag{4.33}$$

with

$$\beta = \frac{g}{R_d \tilde{T}}\left(\frac{L R_d}{c_p R_v \tilde{T}} - 1\right). \tag{4.34}$$

We find that assuming $\tilde{T} = \text{SST}_{\text{Sc}} - 4$ K introduces negligible error over the range of z_b considered. A typical value of β is 0.5 km^{-1}, though this quantity varies slightly over the range of SSTs considered in this paper (as documented in Table 4.2).

A simple expression for RH(0) may be obtained by applying our simplifications to (4.18), solving for q_t, and dividing through by $q_s(\text{SST}, p_{\text{surf}})$,

$$\text{RH}(0) = \frac{\eta}{w_e + \eta}. \tag{4.35}$$

The surface turbulent transfer velocity $\eta = 6.1$ mm s^{-1} in the full model, but will be adjusted in the minimal model to keep cloud base comparable to the full model. Combining (4.33) and (4.35) yields

$$z_b = \beta^{-1}\ln\left(1 + \frac{w_e}{\eta}\right). \tag{4.36}$$

We can understand (4.36) as the product of the RH e-folding depth β^{-1} and the fraction of an e-folding depth that must be traversed for the RH to change from its surface to its

cloud base value. Substituting (4.31) into (4.36) leaves us with

$$z_b = \beta^{-1} \ln \left(1 + \frac{|Q_0^+| z_i}{\eta \Gamma^+ z^*} \right). \tag{4.37}$$

4.4.3 Cloud Top

Under our simplifications, (4.19) reduces to

$$w_e \left(\theta_0^+ - \theta_l \right) = -\Delta R_{\mathrm{BL}}. \tag{4.38}$$

In words, (4.38) states that heat lost to radiative cooling must be replaced by the entrainment flux of relatively warmer air in order to keep the BL in equilibrium.

Recall that we are making a linear approximation to the free- tropospheric temperature profile, so $\theta_0^+ = T_{s,\mathrm{ITCZ}} + \Gamma^+ z_i$. In this equation $T_{s,\mathrm{ITCZ}}$ is the surface temperature in the ITCZ assuming the modified moist adiabat continues down to the surface. Because the full model does not assume a modified moist adiabat to the surface, instead using a dry-adiabatic lapse rate between the surface and an ITCZ cloud base (as explained in section 4.2.1), the actual value of $T_{s,\mathrm{ITCZ}}$ required for our linearization (with Γ^+ evaluated at 1 km) to match θ_0^+ as predicted from the full model is 3.2-3.5K less than $\mathrm{SST}_{\mathrm{ITCZ}}$. Because this variation is so slight, we assume $T_{s,\mathrm{ITCZ}} = \mathrm{SST}_{\mathrm{ITCZ}} - 3.35$ for the remainder of this paper.

Substituting (4.29) into (4.38) leaves us with a quadratic equation for z_i,

$$I(z_i) = z_i^2 + \frac{T_{s,\mathrm{ITCZ}} - \mathrm{SST}_{\mathrm{Sc}}}{\Gamma^+} z_i - \frac{\Delta R_{\mathrm{BL}} z^*}{Q_0^+} = 0. \tag{4.39}$$

Since the z_i^2 term is positive and the constant term is negative, this equation is guaranteed to have a unique positive solution for z_i. The dependence of z_i on the SSTs occurs purely through the coefficient of the linear term, which can be interpreted as a form of lower tropospheric stability or estimated inversion strength (Wood and Bretherton, 2006) normalized into a length scale. Physically, z_i decreases as $T_{s,\mathrm{ITCZ}} - \mathrm{SST}_{\mathrm{Sc}}$ rises because less entrainment is needed to balance a given BL radiative cooling when the

inversion strength is higher. The sensitivity to the free-tropospheric stability Γ^+ can be understood similarly - as Γ^+ increases, $-w_s(z_i) = w_e$ decreases. For entrainment heating to come back into balance with BL radiative cooling, z_i must increase. Since increasing z_i rebuilds entrainment heating by increasing inversion strength in addition to raising w_e, energy balance is reestablished at a lower entrainment rate.

Thus, in the minimal model a geographically-uniform warming (in which $T_{s,\text{ITCZ}}$ − SST_{Sc} remains constant as $T_{s,\text{ITCZ}}$ warms and hence Γ^+ increases) leads to less subsidence, increased z_i, and weakened entrainment. Since (4.36) shows z_b to be an increasing function of w_e, our minimal model predicts z_b to decrease. In combination with the z_i increase, this implies LWP rises as SST warms. This mechanism, which we call subsidence-lapse rate feedback, is the physical explanation suggested by our simple model for the full model's increased LWP in warmer climates.

4.4.4   Analysis

For our simple model to have any predictive value, we must choose representative values for each of the parameters in the above equations. Table 4.2 lists the values used for this purpose. Since these quantities are used to absorb the processes neglected by our simple model, the values in Table 4.2 generally differ from the domain-averaged values from the full-physics run. The quantity z^* was chosen to match the top of the linear w_{s0} region in the full model (which in turn was chosen to be just above the highest diagnosed z_i). The specification of this quantity is arbitrary in the simple model since z^* only appears in combination with Q_0^+. We chose Q_0^+ to make the divergence from the full and simple models agree for current-climate conditions, then determined ΔR_{BL} such that z_i from (4.39) matched the current-climate z_i from the full model. Similarly, full-model current-climate z_b was substituted into (4.37) to determine η. The remaining two parameters, Γ^+ and β, are specified by (4.1) and (4.34), respectively, as in the full-physics model. The lapse rate is calculated at 1 km since in all cases Γ^+ varies by less than 1.1% over all heights below z^*. The ranges for Γ^+ and β given in Table 4.2 are the minimum to maximum over the set of SSTs considered.
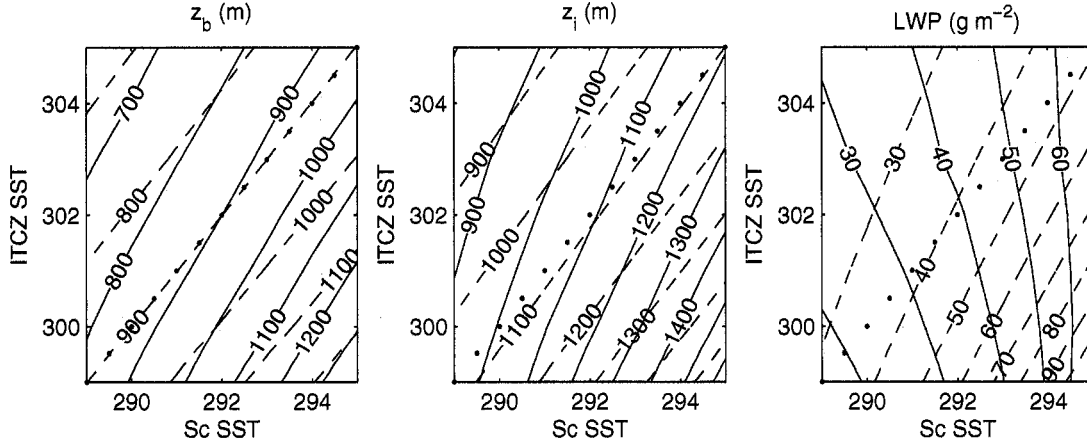
Figure 4.11: Comparison of z_b, z_i from full-physics MLM run (solid lines) with algebraic approximations (dashed lines). For reference, the 1:1 line is included as a dotted line.

Values of z_i, z_b, and LWP generated using the minimal model with the parameters listed in Table 4.2 are plotted against results from the full model in Fig. 4.11. LWP is computed from

$$\text{LWP} = 0.5\rho \left(\frac{\partial q_l}{\partial z} \right)_{\text{adiabatic}} (z_i - z_b)^2 . \qquad (4.40)$$

with ρ and $(\partial q_l/\partial z)_{\text{adiabatic}}$ computed at a reference temperature of $\text{SST}_{\text{Sc}} - 4.5\text{K}$ and a reference pressure of 966mb. The minimal model version of z_i and z_b match the full-model results fairly well, and the LWP is of the right magnitude and displays the right response to SST_{Sc}, though the (weaker) sensitivity to SST_{ITCZ} is of the opposite sign. Nonetheless, the degree to which the full and minimal models agree suggests that subsidence-lapse rate feedback may explain a significant fraction of the LWP rise with uniform SST increase.

Fig. 4.12 shows the profile of full-model cloud base and cloud top along the 1:1 line. Since z_b rises with SST in this figure (while our simple model suggests it should decrease), we must conclude that subsidence-lapse rate feedback does not capture the behavior of the full model in its entirety. Since z_i rises more quickly than z_b, Fig. 4.12 is instead consistent with superposition of the subsidence-lapse rate feedback on top of other dynamics not included in the simple model. Also included in this figure are z_b and
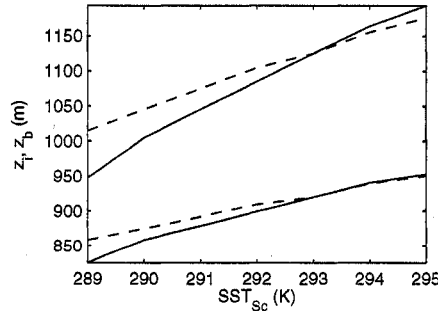
Figure 4.12: Cloud top and cloud base from full model (solid line) and from full model with fixed Γ^+ (dashed line).

z_i from a full-physics run where the subsidence-lapse rate feedback has been artificially removed by fixing the lapse rate to match current conditions (dashed lines). The simple model predicts that z_i should remain constant in this case, but the plotted z_i continues to rise with SST. Note, however, that the rise rate of z_i with fixed lapse rate (no subsidence-lapse rate feedback) is weaker than that of the full model (including subsidence-lapse rate feedback). This is again consistent with the premise that subsidence-lapse rate feedback is one of a number of processes operating in this system. The natural question at this point is what key processes are missing from the simple model.

This is a challenging question because model components interact nonlinearly with each other and their behavior varies depending the solution state. For example, if $\mathbf{v} \cdot \nabla \theta_l$ is taken to be constant with height in the BL (as assumed in the full model), BL-integrated cold advection increases as cloud top rises, requiring an increase in entrainment warming to maintain energy balance. This creates a positive feedback on cloud-top height variations, enhancing (but not causing) the z_i rise in Fig. 4.12. Although this feedback is arguably unphysical because neighboring regions are not infinite sources of cold air, parameterizing advection as a flux per unit vertical distance is standard practice and it is unclear how to improve upon this standard.

One term that can be objectively analyzed is BL horizontal divergence $D = w_s(z_i)/z_i$, which can be extracted from the full model. According to (4.29), $D = Q_0^+/(\Gamma^+ z^*)$. Since

110
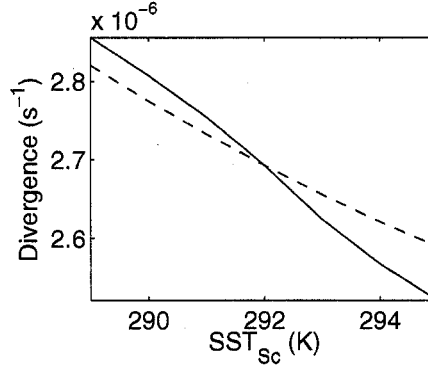
Figure 4.13: Divergence from full model (solid line) compared to divergence predicted by simple model (dashed line).

Γ^+ is calculated almost exactly by the simple model, any error in D can be attributed to our constant Q_0^+ assumption (here, Q_0^+ includes both the effect of BL-induced cooling on w_s, horizontal temperature advection, and the effects of temperature and moisture on the free-tropospheric cooling rate). Fig. 4.13 documents D from the full and the simple models. The difference is slight, accounting for less than 3% error in $w_s(z^*)$ for any SST. Thus it must be other omitted terms that account for the different behavior between the simple and full models.

Objective headway is difficult beyond this example. The interplay between a turbulence-based entrainment scheme (either TN or LL) and drizzle seems to be necessary to capture the trends in both z_b and z_i (not shown). Entrainment in these schemes (and consequently z_i) is enhanced as cloud thickens but is damped by drizzle, which also increases with cloud thickness. These rather complex interactions have prevented us from reaching a complete and satisfying explanation for that part of the behavior of the full model not reflecting subsidence-lapse rate feedback.

4.5 Conclusions

In this chapter, the response of low-latitude Sc to climate change is investigated by coupling a mixed-layer model for a Sc-topped BL to a model of the overlying free troposphere

in which the temperature profile is moist-adiabatically related to ITCZ SST. Equilibrium Sc properties are obtained as a function of local and ITCZ SSTs. This model is simple in spirit, but the radiative feedback of the cold BL on the temperature and subsidence rate of the overlying air complicates both modeling and interpretation. To account for this feedback, we develop a new linear model of the dynamical response of local subsidence to the local diabatic heating profile by regarding the latter as defining a sinusoidal horizontal pattern of heating perturbations whose scale is the distance from the Sc to the ITCZ. Our approach is general and could easily be adapted to use a large-eddy simulation or a single-column model in place of a MLM for the BL. The direct radiative effect of CO_2 change is not included in the model. Off-line calculations suggest this effect is small but not entirely quantitatively negligible.

A robust prediction of this model is that LWP should increase in response to a uniform increase in tropical SST. This finding is insensitive to changes in entrainment or drizzle parameterization, or to any other model details and in fact held up in all of the countless simulations we ran over the course of model development. We were able to prove in a simplified setting that this should be the case for all relevant meteorological conditions, although details omitted from this minimal model play an important role in the quantitative behavior of the full-physics model. This simple model suggests that the cloud thickens in response to the increased static stability of the moist adiabat over a warmer ITCZ. In particular, the increased stability leads to a decrease in the radiatively induced subsidence rate, allowing cloud top to rise. The inversion also strengthens, causing decreased entrainment of dry free-tropospheric air and a lower cloud base. We call these effects, which combine to thicken the Sc, the subsidence-lapse rate feedback.

If the local SST instead responds to the change in forcing in such a way as to maintain a fixed ocean energy balance, LWP rises less rapidly with increasing SST. This is due to a negative feedback - increasing SST causes LWP to increase, decreasing the surface insolation and inhibiting the SST rise. This increases the inversion strength, lowering cloud top and limiting cloud thickness increase. Hence the response of subtropical Sc to warming and its feedback on the global radiation balance is predicted to interact

significantly with the geographical pattern of SST increase.

Lastly, we considered the model response to a simulated indirect aerosol effect, halving the assumed droplet concentration from 100 to 50 cm^{-3}. The equilibrium LWP change was less than 10% for all SST pairs tested, and the resulting second indirect aerosol effect was small compared to the first (Twomey) effect.

While we took care to conduct this study only in a range of conditions under which our MLM is self-consistent (i.e. does not predict significant subcloud decoupling), the results may be quite sensitive to vertical and horizontal inhomogeneity and should be repeated with a suite of more sophisticated single-column and large-eddy simulation models. This will be particularly important in ascertaining the importance of LTS feedback to the tropics-wide response of BL clouds on climate change.

Chapter 5

CONCLUSIONS

The goal of this work is to improve understanding of the processes controlling the Sc-topped BL in an effort to better predict how Sc will respond to climate change. As noted in Chapter 1, this work is important because changes in low cloudiness have the potential to greatly amplify or damp global warming, yet not only the magnitude but also the sign of this feedback is completely unknown.

In Chapter 4 we approach the problem directly by developing a simple model of the Sc region which includes the large-scale effects expected of a warming planet. In this study, the Sc-topped BL is represented by a MLM. Tropical free-tropospheric moisture is computed assuming fixed 10% relative humidity. Away from the BL, free-tropospheric temperature is assumed to be horizontally invariant and set by deep convection to a virtual moist adiabat based on an externally-specified ITCZ SST. Subsidence in this region is computed from the free-tropospheric energy budget. We find enhanced radiative cooling in the air just above z_i (ignored in previous simple models of the tropics) to significantly affect temperature and subsidence profiles just above the BL, and develop a new parameterization to account for this effect.

Steady-state output from our model is then analyzed as a function of local and ITCZ SST. By allowing SST to vary independently in these two regions, we maintain the flexibility to handle any possible geographical pattern of SST change. For concreteness we focus on two cases. In the first case, a balanced surface energy budget with fixed ocean heat transport is assumed. In this case, ITCZ SST is specified and local SST adjusts to balance the budget. In the other case, geographically uniform warming, both local and ITCZ SST are specified. In both cases we find LWP to increase with increasing SST. Since cloud albedo increases with LWP, our results suggest that subtropical Sc feedback will act to substantially decrease climate sensitivity. In a simplified analytical version

of the model, uniformly increased SST was found to raise LWP by decreasing subsidence (which allows BL depth to increase) and simultaneously increasing the lapse rate (which increases inversion strength, resulting in less entrainment and hence a relatively lower cloudbase); we call this mechanism the subsidence lapse-rate feedback. Changes in complex parameterizations such as entrainment, radiation, and drizzle also seem to be playing a role in the full model, making further analysis difficult. When a balanced surface energy budget is used, increased cloud shading causes local SST to warm less rapidly than ITCZ SST. This increases inversion strength, which results in decreased z_i and ultimately damps the LWP response relative to that of uniform SST increase.

As z_i increases, cloud-topped boundary layers tend to develop a cumulus-coupled structure with very different cloud cover and albedo than a MLM. This effect could easily be included in our modeling framework by replacing the MLM used in our study with a more sophisticated BL model such as the LES employed in Chapter 3.

A major problem with modeling studies of this sort is that confidence in the conclusions is severely limited by uncertainties in the parameterizations used. Our ability to represent important processes such as drizzle and entrainment in models is limited by a scarcity of reliable observations and a resulting lack of model-observation comparisons.

To improve this situation, we analyze new observational data from the EPIC 2001 campaign in Chapter 2. In particular, we use BL-averaged budgets of mass, moisture, and liquid water static energy to derive estimates of entrainment at three-hourly resolution over the entire 6-day study period. This is the first time entrainment measurements have been made over an entire diurnal cycle. We find entrainment to be fairly steady at around 5 mm s^{-1} at night, then to drop rapidly to near-zero values by midday (although comparison with LES data in Chapter 3 suggests that this midday value might be underestimated). Under the additional assumption that the BL is well-mixed, we are also able to derive profiles of buoyancy flux (the main source of BL TKE) from the EPIC data. The diurnal cycle of buoyancy flux suggests that drizzle, while only a small term in the boundary-layer moisture budget, significantly reduces sub-cloud buoyancy flux and may induce weak decoupling of surface and cloud-layer turbulence during the early morning

hours, a structure which is maintained throughout the day by shortwave warming.

In the end, modeling uncertainty will only be reduced by testing parameterizations against data. To that end, we also include in Chapter 2 a comparison between entrainment parameterizations and the observed results from EPIC. All of the parameterizations tested were remarkably successful at predicting entrainment across the entire diurnal cycle. This suggests that the results of models such as that described in Chapter 4 are more robust than previously expected, at least with regard to entrainment. In order to facilitate future comparisons with the EPIC data, we have compiled the EPIC-Sc data into a freely-available online archive.

Chapter 3 focuses on a more in-depth comparison between an LES model and the EPIC observations. The LES was able to reproduce many of the observed features from EPIC such as the BL-averaged moisture and energy balances, the level of BL stratification, and the diurnal cycle of LWP. The diurnal cycle of inversion height (and therefore entrainment) and its relation to buoyancy forcing fit the observed data at all times except 1100 LT, when boundary-layer decoupling may be degrading the observational retrievals of buoyancy forcing and inversion height. The LES-predicted drizzle seems more sensitive to LWP than the EPIC observations, and the LES underpredicts subcloud drizzle evaporation. For these reasons, the timing and impact of drizzle in the model differs from that of the observations, preventing us from testing the hypothesis that drizzle induces early-morning decoupling introduced in Chapter 2.

Because LES represents BL processes in a physically consistent way (at least in theory) it can provide insight into questions which are not tractable based on the available observations. For instance, there are no observations of the vertical structure of turbulence in the EPIC BL, but the LES suggests that vertical velocity variance generally has an obvious mid-BL minimum associated with weak or negative buoyancy flux below cloudbase. This suggests that the EPIC BL is always struggling to remain well mixed. Sensitivity studies with LES can also be used to better understand BL processes. One such study we performed focused on the impact of diurnal variations in subsidence on the EPIC BL. We found that removing the diurnal cycle of subsidence had little impact

on BL LWP, despite damping the diurnal cycle of inversion height. We also tried turning off drizzle while leaving cloud droplet sedimentation unaltered, which caused LWP and cloud radiative forcing to increase substantially, but left entrainment and z_i relatively unaffected. In contrast, runs where N_d was decreased fourfold to 25 cm^{-3} were found to have substantially lower entrainment rates, regardless of whether drizzle was included. This suggests that associating entrainment response to N_d changes with drizzle is probably not accurate.

While this thesis yielded significant discoveries, more observations and more observation-guided modeling studies are needed to assess the validity of existent Sc parameterizations and to make improvements where needed. In particular, better understanding of the relationship between turbulence and entrainment is needed. It would be useful to have more simultaneous measurements of entrainment and the processes that may potentially be governing it. Additionally, further studies comparing modeled drizzle to observations would be useful to assess the validity of existing drizzle parameterizations. There are also a great deal of improvements which could be made to the large-scale component of the simple model presented in Chapter 4. In particular, it would be very useful to know surface winds, free-tropospheric subsidence, and ocean heat transport into the Sc region will be affected by global warming. Finally, I believe that better understanding of radiative transfer near the top of Sc is an important and relatively-overlooked problem.

BIBLIOGRAPHY

Ackerman, A. S., M. Kirkpatrick, D. Stevens, and O. Toown, 2004: The impact of humidity above stratiform clouds on indirect aerosol climate forcing. *Nature*, 1014–1017, doi:10.1038/nature03174.

Ackerman, A. S. and O. B. Toon, 1996: Unrealistic desiccation of marine stratocumulus clouds by enhanced solar absorption. *Nature*, **380**, 512–515.

Ackerman, A. S., O. B. Toon, D. E. Stevens, A. J. Heymsfield, V. Ramanathan, and E. Welton, 2000: Reduction of tropical cloudiness by soot. *Science*, 1042–1047.

Agee, E. M., T. S. Chen, and K. E. Dowell, 1973: A review of mesoscale cellular convection. *Bull. Amer. Meteor. Soc.*, **54**, 1004–1012.

Albrecht, B. A., 1989: Aerosols, cloud microphysics, and fractional cloudiness. *Science*, **245**, 1227–1230.

Albrecht, B. A., C. S. Bretherton, D. Johnson, W. H. Scubert, and A. S. Frisch, 1995a: The Atlantic Stratocumulus Transition Experiment - ASTEX. *Bull. Amer. Meteor. Soc.*, **76**, 889–904.

Albrecht, B. A., M. P. Jenson, and W. J. Syrett, 1995b: Marine boundary layer structure and fractional cloudiness. *J. Geophys. Res.*, **100**, 14209–14222.

Albrecht, B. A., D. A. Randall, and S. Nicholls, 1988: Observations of marine stratocumulus during FIRE. *Bull. Amer. Meteor. Soc.*, **69**, 618–626.

Alley, R. et al., 2007: Climate change 2007: The physical science basis. summary for policymakers. Technical report, Intergovernmental Panel on Climate Change, 18pp, http://ipcc-wg1.ucar.edu/wg1/Report/AR4WG1_SPM.pdf.

Betts, A. K., 1973: Non-precipitating cumulus convection and its parameterization. *Quart. J. Roy. Meteor. Soc.*, **99**, 178–196.

—, 1986: A new convective adjustment scheme. Part I: Observational and theoretical basis. *Quart. J. Roy. Meteor. Soc.*, **112**, 677–691.

Betts, A. K. and M. J. Miller, 1986: A new convective adjustment scheme. Part II: Single column tests using GATE wave, BOMEX, ATEX, and arctic-airmass data sets. *Quart. J. Roy. Meteor. Soc.*, **112**, 693–709.

Boers, R., K. B. Krummel, S. T. Siems, and G. D. Hess, 1997: Thermodynamic structure and entrainment of stratocumulus over the southern ocean. *J. Geophys. Res.*, **103**, 16637–16650.

Boers, R. and R. Mitchell, 1994: Absorption feedback in stratocumulus clouds. Influence on cloud-top albedo. *Tellus*, **46A**, 229–241.

Bony, S. and J.-L. Dufresne, 2005: Marine boundary layer clouds at the heart of cloud feedback uncertainties in climate models. *J. Geophys. Res.*, **32**, L20806, doi: 10.1029/2005GL023851.

Bretherton, C., 1997: Convection in stratocumulus-capped atmospheric boundary layers. *The Physics and Parameterization of Moist Atmospheric Convection*, R. Smith, ed., Kluwer Publishers, 127–142.

Bretherton, C., P. Blossey, and J. Uchida, 2007: Cloud droplet sedimentation, entrainment efficiency, and subtropical stratocumulus albedo. *Geophys. Res. Lett.*, **34**, L03813, doi: 10.1029/2006GL027648.

Bretherton, C. S., P. Austin, and S. T. Siems, 1995: Cloudiness and marine boundary layer dynamics in the ASTEX lagrangian experiments. Part II: Cloudiness, drizzle, surface fluxes, and entrainment. *J. Atmos. Sci.*, **52**, 2724–2735.

Bretherton, C. S., M. MacVean, P. Bechtold, A. Chlond, W. Cotton, J. Cuxart, H. Cuijpers, M. Khairoutdinov, D. Lewellen, C. Moeng, P. Siebesma, B. Stevens, D. Stevens, I. Sykes, and M. Wyant, 1999: An intercomparison of radiatively driven entrainment and turbulence in a smoke cloud, as simulated by different numerical models. *Quart. J. Roy. Meteor. Soc.*, **125**, 391–423.

Bretherton, C. S., T. Uttal, C. W. Fairall, S. E. Yuter, R. A. Weller, D. Baumgardner, K. Comstock, and R. Wood, 2004: The EPIC 2001 stratocumulus study. *Bull. Amer. Meteor. Soc.*, **85**, 967–977.

Bretherton, C. S. and M. C. Wyant, 1997: Moisture transport, lower-tropospheric stability, and decoupling of cloud-topped boundary layers. *J. Atmos. Sci.*, **54**, 148–167.

Caldwell, P. M., C. S. Bretherton, and R. Wood, 2005: Mixed-layer budget analysis of the diurnal cycle of entrainment in southeast Pacific stratocumulus. *J. Atmos. Sci.*, **62**, 3775–3791.

Campbell, G., 2004: *View angle dependence of cloudiness and the trend in ISCCP cloudiness*, paper presented at 13th Conference on Satellite Meteorology and Oceanography, Am. Meteor. Soc., Norfolk, Va., 20-23 Sept.

Caughey, S., B. Crease, and W. Roach, 1982: A field study of nocturnal stratocumulus II: Turbulence structure and entrainment. *Quart. J. R. Met. Soc.*, **108**, 125–144.

Cess, R. D. et al., 1989: Interpretation of cloud-climate feedback as produced by 14 atmospheric general circulation models. *Science*, **245**, 513–516.

—, 1997: Comparison of the seasonal change in cloud-radiative forcing from atmospheric general circulation models and satellite observations. *J. Geophys. Res.*, **102**, 16593–16603, doi:10.1029/97JD00927.

Charlson, R. J., S. E. Schwartz, J. M. Hales, R. D. Cess, J. A. Coakley, Jr., J. E. Hansen, and D. J. Hofmann, 1992: Climate Forcing by Anthropogenic Aerosols. *Science*, **255**, 423–430.

Charney, J. G., 1963: A note on large-scale motions in the tropics. *J. Atmos. Sci.*, **20**, 607–609.

Ciesielski, P. E., W. H. Schubert, and R. H. Johnson, 2001: Diurnal Variability of the Marine Boundary Layer during ASTEX. *J. Atmos. Sci.*, **58**, 2355–2376.

Clement, A. and R. Seager, 1999: Climate and the tropical oceans. *J. Climate*, **12**, 3383–3401.

Coakley, J. A. et al., 2000: The appearance and disappearance of ship tracks on large spatial scales. *J. Atmos. Sci.*, **57**, 2765–2778.

Coakley, J. A., Jr. and C. D. Walsh, 2002: Limits to the Aerosol Indirect Radiative Effect Derived from Observations of Ship Tracks. *Journal of Atmospheric Sciences*, **59**, 668–680.

Collins, W. et al., 2006: The Community Climate System Model: CCSW3. *J. Climate*, **19**, 2122–2143.

Comstock, K., R. Wood, S. E. Yuter, and C. S. Bretherton, 2004: Reflectivity and rain rate in and below drizzling stratocumulus. *Quart. J. Roy. Meteor. Soc.*, **130**, 2891–2918.

Comstock, K. K., C. S. Bretherton, and S. E. Yuter, 2005: Mesoscale variability and drizzle in southeast pacific stratocumulus. *J. Atmos. Sci.*, **62**, 3792–3807.

de Roode, S. R. and P. G. Duynkerke, 1997: Observed lagrangian transition of stratocumulus into cumulus during ASTEX: mean state and turbulence structure. *J. Atmos. Sci.*, **54**, 2157–2173.

de Szoeke, S. P. and C. S. Bretherton, 2004: Quasi-Lagrangian Large Eddy Simulations of Cross-Equatorial Flow in the East Pacific Atmospheric Boundary Layer. *J. Atmos. Sci.*, **61**, 1837–1858.

Deardorff, J., 1980: Stratocumulus-capped mixed layers derived from a three-dimensional model. *Bound.-Layer Meteor.*, **18**, 495–527.

—, 1983: A multi-limit mixed-layer entrainment formulation. *J. Phys. Oceanogr.*, **13**, 988–1002.

Dong, X. and G. G. Mace, 2003: Arctic stratus cloud properties and radiative forcing derived from ground-based data collected at Barrow, Alaska. *J. Climate*, **16**, 445–460.

Driedonks, A., 1982: Models and observations of the growth of the atmospheric boundary layer. *Boundary-Layer Meteorol.*, **23**, 283–306.

Duynkerke, G. P., R. S. de Roode, C. van Zanten Margreet, J. Calvo, J. Cuxart, S. Cheinet, A. Chlond, H. Grenier, P. J. Jonker, M. Köhler, G. Lenderink, D. Lewellen, C.-L. Lappen, P. A. Lock, C.-H. Moeng, F. Müller, D. Olmeda, J.-M. Piriou, E. Sánchez, and I. Sednev, 2004: Observations and numerical simulations of the diurnal cycle of the EUROCS stratocumulus case. *Quart. J. Roy. Meteor. Soc.*, **130**, 3269–3296.

Evan, A. T., A. K. Heidinger, and D. J. Vimont, 2007: Arguments against a physical long-term trend in global ISCCP cloud amounts. *Geophys. Res. Let.*, **34**, L4701.

Fairall, C. W., E. F. Bradley, D. P., Rogers, J. B. Edson, and G. S. Young, 1996: Bulk parameterization of air-sea fluxes for tropical ocean global atmosphere coupled ocean atmospere response experiment. *J. of Geophys. Res. - Oceans*, **101**, 3747–3764.

Faloona, I., D. Lenschow, T. Campos, B. Stevens, M. van Zanten, B. Blomquist, D. Thornton, A. Bandy, and H. Gerber, 2005: Observations of entrainment in Eastern Pacific marine stratocumulus using three conserved scalars. *J. Atmos. Sci.*, **62**, 3268–3285.

Garreaud, R. D. and R. Muñoz, 2004: The diurnal cycle in circulation and cloudiness over the tropical southeast Pacific: A modeling study. *J. Climate*, 1699–1710.

Garreaud, R. D., J. Rutlant, J. Quintana, J. Carrasco, and P. Minnis, 2001: CIMAR-5: A snapshot of the lower troposphere over the subtropical southeast Pacific. *Bull. Amer. Meteor. Soc.*, **82**, 2913–2207.

Germano, M., U. Piomelli, P. Moin, and W. Cabot, 1991: A dynamic subgrid-scale eddy viscosity model. *Phys. Fluids A*, **3**, 1760–1765.

Hansen, J., A. Lacis, D. Rind, G. Russell, P. Stone, I. Fung, R. Ruedy, and J. Lerner, 1984: Climate sensitivity: Analysis of feedback mechanisms. *Climate Processes and Climate sensitivity, Geophys. Monogr. No 29*, J. Jansen and T. Takahashi, eds., Amer. Geophys. Union, 130–163.

Hanson, H. P., 1991: Marine stratocumulus climatologies. *Int. J. Climatol.*, **11**, 147–164.

Held, I. M. and B. Soden, 2006: Robust responses of the hydrological cycle to global warming. *J. Climate*, **19**, 5686–5699.

Hignett, P., 1991: Observations of diurnal-variation in a cloud-capped marine boundary-layer. *J. Atmos. Sci.*, **12**, 1474–1482.

Hogg, D. C., F. O. Guiraud, J. B. Snider, M. T. Deckerand, and E. R. Westwater, 1983: A steerable dual-channel microwave radiometer for the measurement of water vapor and liquid in the troposphere. *J. Clim./Appl. Meteorol.*, **5**, 789–806.

Houghton, J., Y. Ding, D. Griggs, M. Noguer, P. van der Linden, X. Dai, and K. Maskell, eds., 2001: *Climate Change 2001: The Scientific Basis*. Cambridge University Press, 892pp.

Houze, R. A., 1993: *Cloud Dynamics*. Acedemic Press, 573pp.

Jiang, H., G. Feingold, and W. R. Cotton, 2002: A modeling study of entrainment of cloud condensation nuclei into the marine boundary layer during ASTEX. *JGR*, **107**, 4813, doi:10.1029/2001JD001502.

Kawa, S. R. and R. Pearson, Jr., 1989: Ozone budgets from the Dynamics and Chemistry of Marine Stratocumulus experiment. *J. Geophys. Res.*, **94**, 9809–9817.

Khairoutdinov, M. F. and Y. L. Kogan, 2000: A new cloud physics parameterization in a large-eddy simulation model of marine stratocumulus. *Mon. Wea. Rev.*, **128**, 229–243.

Khairoutdinov, M. F. and D. A. Randall, 2003: Cloud resolving modeling of the ARM summer 1997 IOP: model formulation, results, uncertainties, and sensitivities. *J. Atmos. Sci.*, **60**, 607–625.

Kiehl, J. T., C. A. Shields, J. J. Hack, and W. D. Collins, 2006: The climate sensitivity of the Community Climate System Model Version 3 (CCSM3). *J. Climate*, **19**, 2584–2596.

Klein, S. A. and D. L. Hartmann, 1993: The seasonal cycle of low stratiform clouds. *J. Climate*, **6**, 1587–1606.

Klein, S. A., D. L. Hartmann, and J. R. Norris, 1995: On the relationships among low-cloud structure, sea surface temperature, and atmospheric circulation in the summertime northeast pacific. *J. Climate*, **8**, 1140–1655.

Knutson, T. and S. Manabe, 1995: Time-mean response over the tropical Pacific to increased $CO2$ in a coupled ocean-atmosphere model. *J. Climate*, **8**, 2181–2199.

Kollias, P., C. Fairall, P. Zuidema, J. Tomlinson, and G. Wick, 2004: Observations of marine stratocumulus in SE Pacific during the PACS 2003 cruise. *Geophys. Res. Lett.*, **31**, L22110.

Larson, K., D. Hartmann, and S. Klein, 1999: the role of clouds, water vapor, circulation, and boundary layer structure in the sensitivity of the tropical climate. *J. Climate*, **12**, 2359–2374.

Lenschow, D. H., M. Y. Zhou, L. S. Chen, and X. D. Xu, 2000: Measurements of finescale structure at the top of marine stratocumulus. *Boundary Layer Meteorology*, **97**, 331–357.

Lewellen, D. and W. Lewellen, 1998: Large-eddy boundary layer entrainment. *J. Atmos. Sci.*, **55**, 2645–2665.

Lilly, D., 1968: Models of cloud-topped mixed layers under a strong inversion. *Quart. J. Roy. Meteor. Soc.*, 292–309.

—, 2002a: Entrainment into mixed layers. Part I: Sharp-edged and smoothed tops. *J. Atmos. Sci.*, **59**, 3340–3352.

—, 2002b: Entrainment into mixed layers. Part II: A new closure. *J. Atmos. Sci.*, 3353–3361.

Liou, K., 2002: *An Introduction to Atmospheric Radiation*. Academic Press, 583pp.

Ma, C.-C., C. R. Mechoso, A. W. Robertson, and A. Arakawa, 1996: Peruvian Stratus Clouds and the Tropical Pacific Circulation: A Coupled Ocean-Atmosphere GCM Study. *Journal of Climate*, **9**, 1635–1645.

Martin, G. M., W. Johnson, and A. Spice, 1994: The measurement and parameterization of effective radius of droplets in warm stratocumulus clouds. *J. Atmos. Sci.*, **51**, 1823–1842.

McCaa, J. and C. Bretherton, 2004: A new parameterization for shallow cumulus convection and its application to marine subtropical cloud-topped boundary layers. Part II: Regional simulations of marine boundary layer clouds. *Mon. Wea. Rev.*, **132**, 883–896.

McClatchey, R., R. Fenn, J. Selby, F. Volz, and J. Garing, 1971: Optical properties of the atmosphere. Technical Report Rep. AFCRL-71-0497, Air Force Cambridge Res. Lab., Hanscom AFB, Bedford MA.

McEwan, A. D. and G. W. Paltridge, 1976: Radiatively driven thermal convection bounded by an inversion-A laboratory simulation of stratus clouds. *J. Geophys. Res.*, **81**, 1095–1102.

McNoldy, B., P. E. Ciesielski, W. H. Schubert, and R. H. Johnson, 2004: Surface winds, divergence, and vorticity in stratocumulus regions using quikscat and reanalysis. *Geophys. Res. Lett.*, **31**, L08105, doi:10.1029/2004GL019768.

Medeiros, B., B. Stevens, I. M. Held, M. Zhao, D. L. Williamson, J. G. Olson, and C. S. Bretherton, 2007: Aquaplanets, climate sensitivity, and low clouds, submitted, J. Clim.

Miller, R., 1997: Tropical thermostats and low cloud cover. *J. Climate*, **10**, 409–440.

Moeng, C.-H., 1984: A Large-Eddy-Simulation Model for the Study of Planetary Boundary-Layer Turbulence. *Journal of Atmospheric Sciences*, **41**, 2052–2062.

Nicholls, S., 1984: The dynamics of stratocumulus: aircraft observations and comparisons with a mixed layer model. *Quart. J. Roy. Meteor. Soc.*, **110**, 783–820.

Nicholls, S. and J. Turton, 1986: An observational study of the structure of stratiform cloud sheets: Part II. entrainment. *Quart. J. Roy. Meteorol. Soc.*, **112**, 461–480.

Norris, J. R., 1999: On Trends and Possible Artifacts in Global Ocean Cloud Cover between 1952 and 1995. *Journal of Climate*, **12**, 1864–1870.

—, 2005: Multidecadal changes in near-global cloud cover and estimated cloud cover radiative forcing. *J. of Geophys. Res. (Atmospheres)*, **110**, 8206–+.

Oreopoulos, L. and R. Davies, 1993: Statistical Dependence of Albedo and Cloud Cover on Sea Surface Temperature for Two Tropical Marine Stratocumulus Regions. *Journal of Climate*, **6**, 2434–2447.

Paluch, I. R. and D. H. Lenschow, 1991: Stratiform cloud formation in the marine boundary layer. *J. Atmos. Sci.*, **48**, 2141–2158.

Pawlowska H. and J.-L. Brenguier, 2003: An observational study of drizzle formation in stratocumulus clouds for general circulation model (GCM) parameterizations. *J. of Geophys. Res. (Atmospheres)*, **108**, 8630–+.

Payne, R., 1986: Albedo of the sea surface. *J. Atmos. Sci.*, **29**, 959–970.

Pierrehumbert, R. T., 1995: Thermostats, radiator fins, and the runaway greenhouse. *J. Atmos. Sci.*, **52**, 1784–1806.

Pincus, R. and M. B. Baker, 1994: Effect of precipitation on the albedo susceptibility of clouds in the marine boundary layer. *Nature*, **372**, 1994.

Pope, S., 2000: *Turbulent Flows*. Cambridge University Press, 770pp.

Radke, L. F., J. A. Coakley, and M. D. King, 1989: Direct and Remote Sensing Observations of the Effects of Ships on Clouds. *Science*, **246**, 1146–1149.

Randall, D., 1980: Conditional instability of the first kind upside-down. *J. Atmos. Sci.*, **37**, 125–130.

—, 1984: Stratocumulus cloud deepening through entrainment. *Tellus*, **36A**, 447–456.

Randall, D., J. Coakley Jr, D. Lenschow, C. Fairall, and R. Kropfli, 1984: Outlook for research on subtropical marine stratification clouds. *Bull. Amer. Meteor. Soc.*, **65**, 1290–1301.

Randall, D., S. Krueger, C. Bretherton, et al., 2003: Confronting models with data - the GEWEX cloud systems study. *Bull. Amer. Meteor. Soc.*, **4**, 455–469.

Randall, D. and M. Suarez, 1984: On the dynamics of stratocumulus formation and dissipation. *J. Atmos. Sci.*, **41**, 3052–3057.

Roach, W. T., R. Brown, S. J. Caughey, B. A. Crease, and A. Slingo, 1982: A field study of nocturnal stratocumulus: I. mean structure and budgets. *Quart. J. Roy. Meteor. Soc.*, 103–123.

Rozendaal, M., C. B. Leovy, and S. A. Klein, 1995: An observational study of diurnal variations of marine stratiform cloud. *J. Climate*, 1795–1809.

Savic-Jovcic, V. and B. Stevens, 2007: The structure and mesoscale organization of precipitating stratocumulus, submitted, J. Atmos. Sci.

Sayler, B. J. and R. E. Breidenthal, 1997: Laboratory simulations of radiatively induced entrainment in stratiform clouds. *J. Geophys. Res.*, **103**, 8827–8838.

Slingo, A., 1990: Sensitivity of the earth's radiation budget to changes is low clouds. *Nature*, **343**, 49–51.

Slingo, A., R. C. Wilderspin, and R. N. B. Smith, 1989: Effect of improved physical parameterizations on simulations of cloudiness and the Earth's radiation budget. *J. Geophys. Res.*, **94**, 2281–2301.

Smagorinsky, J., 1963: General circulation experiments with the primitive equations: I. the basic equations. *Mon. Weather Rev.*, **91**, 99–164.

Sobel, A. H., J. Nilsson, and L. M. Polvani, 2001: The weak temperature gradient approximation and balanced tropical moisture waves. *J. Atmos. Sci.*, **58**, 3650–3665.

Soden, B. J., R. T. Wetherald, G. L. Stenchikov, and A. Robock, 2002: Global cooling after the eruption of Mount Pinatubo: A test of climate feedback by water vapour. *Science*, **296**, 727–730.

Somerville, R. C. J. and L. A. Remer, 1984: Cloud optical thickness feedbacks in the CO2 climate problem. *J. Geophys. Res.*, **89**, 9668–9672.

Stephens, G., P. Partain, and P. Gabriel, 2001: Parameterization of atmospheric radiative transfer. Part I: Validity of simple models. *J. Atmos. Sci.*, **48**, 3391–3409.

Sterl, A. and W. Hazeleger, 2005: The relative roles of tropical and extra-tropical forcing on atmospheric variability. *Geophys. Res. Lett.*, **32**, L18716, doi:10.1029/2005GL023757.

Stevens, B., 2000: Cloud transitions and decoupling in shear-free stratocumulus-topped boundary layers. *Geophys. Res. Lett.*, **27**, 2557–2560.

—, 2002: Entrainment in stratocumulus-topped mixed layers. *Quart. J. Roy. Meteorol. Soc.*, **128**, 2663–2689.

Stevens, B., A. Beljaars, S. Bordoni, C. Holloway, M. Köhler, S. Krueger, V. Savic-Jovcic, and Y. Zhang, 2007: On the structure of the lower troposphere in the summertime stratocumulus regime of the northeast pacific. *Mon. Weath. Rev*, **135**, 985–1005.

Stevens, B., W. R. Cotton, G. Feingold, and C.-H. Moeng, 1998: Large-eddy simulations of strongly precipitating, shallow stratocumulus-topped boundary layers. *J. Atmos. Sci.*, **55**, 3616–3638.

Stevens, B., C.-H. Moeng, and P. P. Sullivan, 1999: Large-Eddy Simulations of Radiatively Driven Convection: Sensitivities to the Representation of Small Scales. *J. Atmos. Sci*, **56**, 3963–3984.

Stevens, B., G. Vali, K. Comstock, R. Wood, M. vanZanten, P. Austin, C. Bretherton, and D. Lenschow, 2005a: Pockets of open cells and drizzle in marine stratocumulus. *Bull. Amer. Meteor. Soc.*, 51–57.

Stevens, B. et al., 2003: On entrainment rates in nocturnal marine stratocumulus. *Quart. J. Roy. Meteor. Soc.*, **84**, 3469–3493.

—, 2005b: Evaluation of large-eddy simulations via observations of nocturnal marine stratocumulus. *Mon. Wea. Rev.*, **133**, 1443–1462.

Stevens, D. E. and C. S. Bretherton, 1999: Effects of resolution on the simulation of stratocumulus entrainment. *Quart. J. Roy. Meteorol. Soc.*, **125**, 425–439.

Turner, J., 1973: *Buoyancy Effects in Fluids*. Cambridge Press, 360pp.

Turton, J. and S. Nicholls, 1987: A study of the diurnal variation of stratocumulus using a multiple mixed layer model. *Q.J.R. Meteorol. Soc*, **113**, 969–1009.

Twomey, S., 1977: The influence of pollution on the shortwave albedo of clouds. *J. Atmos. Sci.*, **34**, 1149–1152.

Uppala, S. et al., 2005: The ERA-40 re-analysis. *Quart. J. Roy. Meteor. Soc.*, **131**, 2961–3012.

vanZanten, M. C. and P. G. Duynkerke, 2001: Radiative and evaporative cooling in the entrainment zone of stratocumulus - the role of longwave radiative cooling above cloud top. *Bound.-Layer Meteor.*, **102**, 253–280.

Vanzanten, M. C., B. Stevens, G. Vali, and D. H. Lenschow, 2005: Observations of Drizzle in Nocturnal Marine Stratocumulus. *Journal of Atmospheric Sciences*, **62**, 88–106.

Vecchi, G., B. Soden, A. Wittenberg, I. Held, A. Leetmaa, and M. Harrison, 2006: Weakening of tropical Pacific atmospheric circulation due to anthropogenic forcing. *Nature*, **44**, 73–76.

Williams, K. D., M. A. Ringer, C. A. Senior, M. J. Webb, B. J. McAvaney, N. Andronova, S. Bony, J.-L. Dufresne, S. Emori, R. Gudgel, T. Knutson, B. Li, K. Lo, I. Musat, J. Wegner, A. Slingo, and J. F. B. Mitchell, 2006: Evaluation of a component of the cloud response to climate change in an intercomparison of climate models. *Climate Dynamics*, **26**, 145–165.

Wood, R., 2005: Drizzle in stratocumulus clouds. Part I: Aircraft observations. *J. Atmos. Sci.*, **62**, 3011–3033.

—, 2007a: Cancellation of aerosol indirect effects in marine stratocumulus through cloud thinning. *J. Atmos. Sci.*, **64**, 2657–2669.

—, 2007b: Cancellation of aerosol indirect effects in marine stratocumulus through cloud thinning, in press.

Wood, R. and C. S. Bretherton, 2004: Boundary layer depth, entrainment, and decoupling in the cloud-capped subtropical and tropical marine boundary layer. *J. Climate*, **17**, 3576–3588.

—, 2006: On the relationship between stratiform low cloud cover and lower tropospheric stability. *J. Climate*, **19**, 6425–6432.

Wood, R., C. S. Bretherton, and D. L. Hartmann, 2002: Diurnal cycle of liquid water path over the subtropical and tropical oceans. *Geophys. Res. Lett.*, **29**.

Wyant, M., C. S. Bretherton, J. T. Bacmeister, J. T. Kiehl, I. M. Held, M. Zhao, S. A. Klein, , and B. A. Soden, 2006: A comparison of tropical cloud properties and responses in GCMs using mid-tropospheric vertical velocity. *Climate Dyn.*, **27**, 261–279.

Wyant, M. et al., 2007: A single column model intercomparison of a heavily drizzling stratocumulus topped boundary layer, submitted 2/07.

Xue, H., G. Feingold, and B. Stevens, 2007: Aerosol effects on clouds, precipitation, and the organization of shallow cumulus convection, accepted.

Yu, J.-Y. and C. R. Mechoso, 1999: Links between Annual Variations of Peruvian Stratocumulus Clouds and of SST in the Eastern Equatorial Pacific. *Journal of Climate*, **12**, 3305–3318.

Zhang, M. and H. Soon, 2006: Deceleration of the atmospheric Walker circulation in the last fifty years. *Geophys. Res. Lett.*, **33**, L12701, doi:10.1029/2006GL025942.

Zhu, P. . et al., 2005: Intercomparison and interpretation of single column model simulations of a nocturnal stratocumulus topped marine boundary layer. *Mon. Wea. Rev.*, **133**, 2741–2758.

Zhu, P., J. Hack, J. Kiehl, and C. Bretherton, 2007: Climate sensitivity of tropical and subtropical marine low cloud amount to ENSO and global warming due to doubled CO2, accepted.

Zuidema, P., E. R. Westwater, C. Fairall, and D. Hazen, 2005: Ship-based liquid water path estimates in marine stratocumulus. *J. Geophys. Res. (Atmos.)*, **110**, D20206, doi:10.1029/2005JD005833.

Appendix A

DERIVATION OF BUDGET EQUATIONS

For some quantity A, the time tendency of A can be written in terms of the convergence of its flux F_A,

$$\frac{\partial A}{\partial t} + \mathbf{v} \cdot \nabla_h A + w \frac{\partial A}{\partial z} = -\frac{1}{\rho} \nabla \cdot F_A \tag{A.1}$$

where ∇_h is the horizontal divergence operator (the vertical divergence is considered explicitly) and ρ is the air density. The large-scale pressure field is in hydrostatic balance and by classical Boussinesq scaling assumptions, horizontal pressure perturbations are negligibly small compared to those in the vertical, so at any $\hat{p}$ (defined in section 2.2.1 of the text), $\partial \hat{p} = \rho g \partial z$ and by extension the vertical pressure-velocity $\hat{\omega}$ satisfies $\hat{\omega} = \rho g w$. Applying this relation to (A.1),

$$\frac{\partial A}{\partial t} + \mathbf{v} \cdot \nabla_h A + \hat{\omega} \frac{\partial A}{\partial \hat{p}} = -\frac{1}{\rho} \nabla_h \cdot F_A - g \frac{\partial F_A}{\partial \hat{p}}. \tag{A.2}$$

Reynolds averaging this last equation and noting that conservation of mass implies $\partial u / \partial x + \partial v / \partial y + \partial \hat{\omega} / \partial \hat{p} = 0$,

$$\frac{\partial \overline{A}}{\partial t} + \overline{\mathbf{v}} \cdot \nabla_h \overline{A} + \hat{\omega}_s \frac{\partial \overline{A}}{\partial \hat{p}} + \frac{\partial \overline{\hat{\omega}' A'}}{\partial \hat{p}} = -g \frac{\partial \overline{F_A}}{\partial \hat{p}} \tag{A.3}$$

where overbars denote horizontally-averaged quantities, primes imply perturbations from this average, and it is recognized that $\overline{\hat{\omega}}$ is the subsidence rate, $\hat{\omega}_s$. In this equation, $\nabla_h \cdot \overline{\hat{\omega}' A'}$ and $\nabla_h \cdot \overline{F_A}$ have been neglected in recognition of their relative insignificance when compared to the vertical gradients. Integrating over the BL depth $\hat{p}_i$, (A.3) becomes

$$\int_0^{\hat{p}_i} \frac{\partial \overline{A}}{\partial t} d\hat{p} + \hat{p}_i \left\langle \overline{\mathbf{v}} \cdot \nabla_h \overline{A} \right\rangle + \int_0^{\hat{p}_i} \hat{\omega}_s \frac{\partial \overline{A}}{\partial \hat{p}} d\hat{p} + \overline{\hat{\omega}' A'} \big|_0^{\hat{p}_i} = -g F_A \big|_0^{\hat{p}_i} \tag{A.4}$$

where angle brackets refer to BL-averaged quantities. The first term in (A.4) can be simplified by noting that

$$\int_0^{\hat{p}_i} \frac{\partial \overline{A}}{\partial t} d\hat{p} = \frac{\partial}{\partial t} \int_0^{\hat{p}_i} \overline{A} d\hat{p} - \frac{\partial \hat{p}_i}{\partial t} \overline{A}|_{\hat{p}_{i-}} \tag{A.5}$$

$$= \frac{\partial \left(\hat{p}_i \left\langle \overline{A} \right\rangle \right)}{\partial t} - \frac{\partial \hat{p}_i}{\partial t} \overline{A}|_{\hat{p}_{i-}} \tag{A.6}$$

$$= \left[\left\langle \overline{A} \right\rangle - \overline{A}|_{\hat{p}_{i-}} \right] \frac{\partial \hat{p}_i}{\partial t} + \hat{p}_i \frac{\partial \left\langle \overline{A} \right\rangle}{\partial t}. \tag{A.7}$$

where $\overline{A}|_{\hat{p}_{i-}}$ is $\overline{A}$ evaluated just below the inversion. The third term in (A.4) may be rewritten as

$$\int_0^{\hat{p}_i} \hat{\omega}_s \frac{\partial \overline{A}}{\partial \hat{p}} d\hat{p} = \int_0^{\hat{p}_i} \frac{\partial \left(\hat{\omega}_s \cdot \overline{A} \right)}{\partial \hat{p}} d\hat{p} - \int_0^{\hat{p}_i} \overline{A} \frac{\partial \hat{\omega}_s}{\partial \hat{p}} d\hat{p} \tag{A.8}$$

$$= \hat{\omega}_s \cdot \overline{A}|_{\hat{p}_{i-}} - \frac{\partial \hat{\omega}_s}{\partial \hat{p}} \cdot \hat{p}_i \left\langle \overline{A} \right\rangle \tag{A.9}$$

$$= \hat{\omega}_s \left[\overline{A}|_{\hat{p}_{i-}} - \left\langle \overline{A} \right\rangle \right]. \tag{A.10}$$

In the above equation, the second equality follows from assuming that horizontal divergence, $-\partial \hat{\omega}_s / \partial \hat{p}$, is constant in height (true for a well-mixed BL since in this case horizontal winds are height independent) and noting that $\hat{\omega}_s = 0$ at the surface. The final line results from noting that if $\partial \hat{\omega}_s / \partial \hat{p}$ is height independent, $\hat{p}_i \partial \hat{\omega}_s / \partial \hat{p} = \hat{\omega}_s|_{\hat{p}_i}$.

Applying (A.7) and (A.10) to (A.4) and noting that turbulent flux across the cloud top is predominantly due to entrainment of above-BL air, a relationship expressed by $\overline{\hat{\omega}' A'}|_{\hat{p}_i} = -\hat{\omega}_e \left(\overline{A}|_{\hat{p}_{i+}} - \overline{A}|_{\hat{p}_{i-}} \right)$ (where $\hat{\omega}_e$ is the pressure-entrainment rate),

$$\hat{p}_i \left[\frac{\partial \left\langle \overline{A} \right\rangle}{\partial t} + \left\langle \overline{\mathbf{v} \cdot \nabla_h \overline{A}} \right\rangle \right] + \left(\hat{\omega}_s - \frac{\partial \hat{p}_i}{\partial t} + \hat{\omega}_e \right) \left[\overline{A}|_{\hat{p}_{i-}} - \left\langle \overline{A} \right\rangle \right]$$
$$- \hat{\omega}_e \left[\overline{A}|_{\hat{p}_{i+}} - \left\langle A \right\rangle \right] - \overline{\hat{\omega}' A'}|_0 + g F_A|_0^{\hat{p}_i} = 0. \tag{A.11}$$

Defining $\Delta A = \left[\overline{A}|_{\hat{p}_{i+}} - \left\langle A \right\rangle \right]$ (where $\overline{A}|_{\hat{p}_{i+}}$ is $\overline{A}$ evaluated just above the inversion) and

noting that $\hat{\omega}_s - \frac{\partial \hat{p}_i}{\partial t} + \hat{\omega}_e = \overline{\mathbf{v}} \cdot \nabla_h \hat{p}_i$ (from (2.3) in the main text),

$$\hat{p}_i \left[\frac{\partial \langle \overline{A} \rangle}{\partial t} + \langle \overline{\mathbf{v}} \cdot \nabla_h \overline{A} \rangle \right] - \overline{\hat{\omega}' A'}|_0 + g F_A|_0^{\hat{p}_i} - \hat{\omega}_e \Delta A = \left[\langle A \rangle - \overline{A}|_{\hat{p}_{i-}} \right] \overline{\mathbf{v}} \cdot \nabla_h \hat{p}_i \quad (A.12)$$

which yields the budget equations presented in this study ((2.1) and (2.2) in the text) when $\overline{A}$ is replaced by q_t (which makes the turbulent surface flux $g \cdot \frac{\text{LHF}}{L}$ and the flux function $F_{q_t} = F_P$) or by s_l (in which case $\overline{\hat{\omega}' A'}|_0 = g \cdot \text{SHF}$ and $F_{s_l} = F_R - L F_P$).

Appendix B

SURFACE GEOSTROPHIC WINDS

Assuming $Du/Dt = 0$ and neglecting viscous effects, the Boussinesq momentum equations can be written

$$f(v - v_g) = \frac{\partial \overline{u'w'}}{\partial z}, \tag{B.1}$$

$$-f(u - u_g) = \frac{\partial \overline{v'w'}}{\partial z} \tag{B.2}$$

where v_g and u_g are the zonal and meridional geostrophic winds, respectively. If the BL is well-mixed, u, v, u_g, and v_g should be constant in height above the surface layer. Assuming momentum flux across z_i to be zero (reasonable since $w' \approx 0$ above z_i), (B.1) and (B.2) can be integrated between 0 and z_i to yield

$$v_g = v + \frac{\overline{u'w'}(0)}{f z_i} \tag{B.3}$$

$$v_g = u - \frac{\overline{v'w'}(0)}{f z_i}. \tag{B.4}$$

To compute representative values for EPIC from the above equations, u and v are taken to be BL-average values from radiosonde data. Surface momentum fluxes are computed using ship-based 14 m winds and the empirical relation

$$\overline{u'w'}(0) = -C_D |u| u \tag{B.5}$$

with $C_D = 1.5 \times 10^{-3}$.

VITA

Peter Caldwell was born in Frederick, MD on St. Patrick's Day of 1977, but spent most of his formative years in Western Washington. He received Bachelor and Master of Science degrees in mathematics from Western Washington University in 1999 and 2001 (respectively), and this Ph.D. from the University of Washington in 2007.